RICE UNIVERSITY

Measurement of the Forward-Backward Asymmetry in the Production of $B^{\pm}$ Mesons in $p\bar{p}$ Collisions

by

Julie Managan Hogan

A THESIS SUBMITTED
IN PARTIAL FULFILLMENT OF THE
REQUIREMENTS FOR THE DEGREE

Doctor of Philosophy

APPROVED, THESIS COMMITTEE:

Marjorie D. Corcoran, Chair
Professor of Physics and Astronomy

Frank Geurts
Assistant Professor of Physics and Astronomy

Stephen Semmes
Professor of Mathematics

Houston, Texas

February, 2015

Measurement of the Forward-Backward Asymmetry in the Production of $B^{\pm}$ Mesons in $p\bar{p}$ Collisions

Julie Managan Hogan

Abstract

We present a measurement of the forward-backward asymmetry in the production of $B^{\pm}$ mesons, $A_{\rm FB}(B^{\pm})$, using $B^{\pm} \to J/\psi K^{\pm}$ decays in 10.4 fb^{-1} of $p\bar{p}$ collisions at $\sqrt{s} = 1.96$ TeV collected by the DØ experiment during Run II of the Tevatron collider. A nonzero asymmetry would indicate a preference for a particular flavor, i.e., b quark or $\bar{b}$ antiquark, to be produced in the direction of the proton beam. We extract $A_{\rm FB}(B^{\pm})$ from a maximum likelihood fit to the difference between the numbers of forward- and backward-produced $B^{\pm}$ mesons, using a boosted decision tree to reduce background. Corrections are made for reconstruction asymmetries of the decay products. We measure an asymmetry consistent with zero: $A_{\rm FB}(B^{\pm}) = [-0.24 \pm 0.41\,({\rm stat}) \pm 0.19\,({\rm syst})]\%$. The standard model estimate from next-to-leading-order Monte Carlo is $A_{\rm FB}^{\rm SM}(B^{\pm}) = [2.31 \pm 0.34\,({\rm stat.}) \pm 0.51\,({\rm syst.})]\%$. There is a difference of ≈ 3 standard deviations between this prediction and our result, which suggests that more rigorous determination of the standard model prediction is needed to interpret these results.

Acknowledgments

Ten years ago when I was making decisions about where to study physics in college, I couldn't imagine getting to this point. I want to thank Paul Sheldon and Will Johns at Vanderbilt for taking in an undergraduate researcher who could barely open a UNIX terminal, much less write any useful program. I didn't produce much physics for their group, but learned to use the programs that would make or break my graduate work.

Construction of DØ began before I was born, and I owe a massive debt of gratitude to everyone who designed, built, and ran the detector over the last thirty years. I also want to thank George Ginther and Stefan Gruenendahl for teaching me so much about DØ and giving me the opportunity to lead tours.

To Marj Corcoran and everyone in the heavy flavor group, I would have been lost without you. Thank you all for pointing me to a fruitful topic and teaching me the techniques I needed to make the measurement. So many periods of frustration were ended at our meetings, and so many mistakes were corrected because of your careful reviews. And to Michelle Mathis and Jesus Orduña, thank you for always seeing me as more capable than I could see myself – your encouragement and friendship kept me moving forward.

To my fellow singers, thank you for making music with me. Greg Wheatley, ever since my audition when I said I studied physics at the Tevatron and you responded "is it an

accelerated program?", I knew the Glen Ellyn-Wheaton Chorale was the right group for me. And Rollie Lindstrom, here's the long promised pay-off for your generous "Hogan's Heroes" Red Solo Cup Award. Cheers!

To my parents, thank you for never letting me accept less than my best, and for always assuming I would succeed. I once described our family's various science careers and was told "you must have such empowering family gatherings". Thank you for seeing a basic science career as completely normal, and for constantly empowering me (even when we aren't talking about science).

And to Thomas – I love coming home every day and being with you. I love that you've never doubted I could do this, and you've never grown tired of supporting me through my own doubts. I love that you give pizza delivery the same enthusiasm you give home cooked dinners. Thank you for throwing your oar in with mine and not looking back.

"But one thing I do: forgetting what lies behind and straining forward to what lies ahead, I press on toward the goal for the prize of the upward call of God in Christ Jesus."

Phil. 3:13-14

Contents

Illustrations

Tables

Chapter 1

Creating Asymmetries: the Standard Model and Beyond

My family are fans of a television show called "How It's Made", which documents the manufacturing process of any item you could ever be curious about. All of science seeks to answer that basic question – how and why do things work? Particle physicists have a great luxury: the thing we seek to understand is not merely a new computing system or advanced material, but the universe itself. For thousands of years knowledge of the fundamental particles of the universe has been unfolding like a set of Russian dolls, as scientists discovered smaller and smaller particles inside what was previously believed to be indivisible. The pace of discovery exploded in the 20th century, and now all the results of study and experiment are summarized in a theory called the "standard model".

1.1 Standard Model of Particle Physics

The standard model (SM) describes the properties of the twelve elementary particles, four force carrying gauge bosons, and the electroweak symmetry breaking Higgs boson (Fig. 1.1) [1].

The box structure of Fig. 1.1 is not just an aesthetic choice: the twelve particles shown on the left side of the figure are joined by type, quark or lepton, as well as "family" or "generation". Quarks and leptons are distinguished by the forces with which they interact.

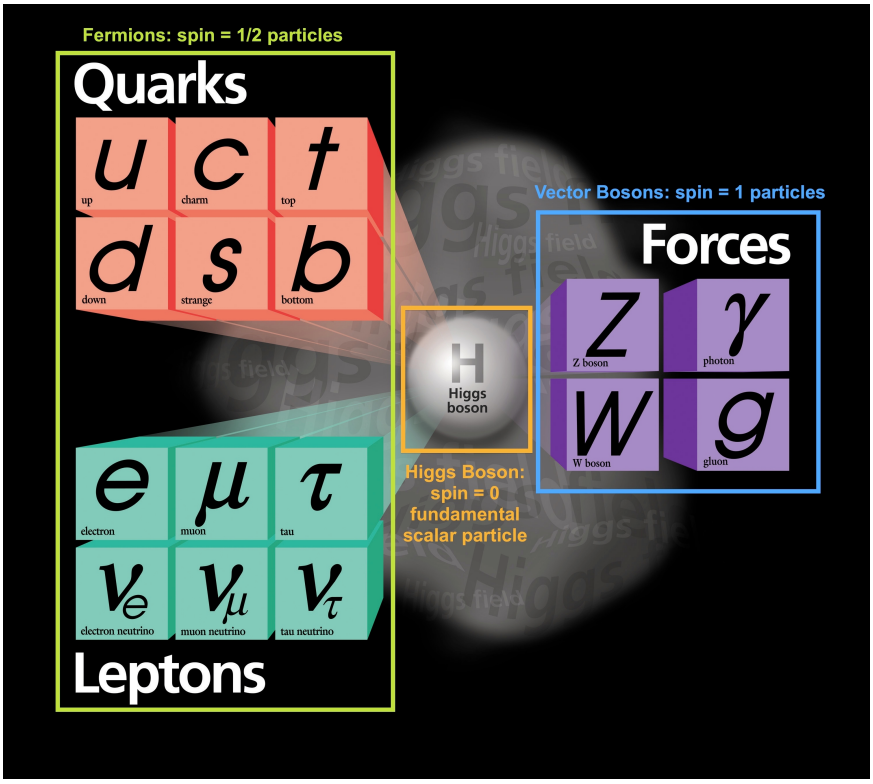

Figure 1.1 : Particles of the Standard Model. Figure from [2].

Through studying electrons and their structure within atoms the property of "spin", a particle's intrinsic angular momentum, was discovered. Particles with half-integer spin values are called "fermions": they are observed to obey Fermi-Dirac statistics where no two particles can occupy the same quantum mechanical state. All quarks and leptons have spin equal to 1/2, the smallest conventional unit.

The first generation of fermions contains the lightest quarks and leptons: up (u) and down (d) quarks which build the familiar protons (uud) and neutrons (udd), and the electron which completes the atom. Since the electron and proton also set the conventional unit of charge, the quarks are left with non-unit charges: up-type quarks in the top row have charge 2/3, and down-type quarks in the second row have charge -1/3.

The electron neutrino (ν_e) is a neutral particle with nearly zero mass which was discovered because of its role in radioactive decays. Neutrinos behave in very unique ways since their mass is nearly zero and they only interact with other particles through the weak force, described below. While neutrinos are frequently produced in radioactive beta decays or high energy particle collisions, once produced their probability of interacting again is very small.

Particles in the second and third generations have larger masses than their partners in the first generation, but have identical charges and properties, listed in Table 1.1. All the fermions have corresponding antiparticles with the opposite charges (and colors, in the case of antiquarks). Antiparticles are labeled with a bar over a particle's symbol, such as $\bar{p}$ for antiprotons.

The four particles in the right-hand box of Fig. 1.1 are called bosons, and have spin

Table 1.1 : Standard model fermion properties. Masses are averaged by the Particle Data Group [3].

Gen.	Quarks			Leptons		
	Symbol	Charge (e)	Mass (MeV)	Symbol	Charge (e)	Mass (MeV)
1^{st}	u	$+2/3$	≈ 2	e^-	-1	0.511
	d	$-1/3$	≈ 5	ν_e	0	< 2 eV
2^{nd}	c	$+2/3$	95	μ^-	-1	106
	s	$-1/3$	1275	ν_μ	0	< 0.2
3^{rd}	t	$+2/3$	173,210	τ^-	-1	1,777
	b	$-1/3$	4,180	ν_τ	0	< 18.2

equal to 1. All bosons have integer spin values and obey Bose-Einstein statistics, where any number of particles can share the same quantum state. The interactions of these particles with matter produces what we call the fundamental forces. An electromagnetic force between charged particles can be described as an exchange of photons (γ). Photons can carry energy proportional to their wavelength, for instance the colors of light detected by our eyes, or they can be "virtual" and transfer energy not allowed by classical conservation laws. A virtual particle can transfer energy ΔE as long as it only exists for a time $\Delta t \leq \hbar/\Delta E$, where where $\hbar$ is the reduced version of Planck's constant. This quantum mechanical uncertainty means that the energy imbalance exists for such a short time it cannot be measured.

The weak nuclear force is mediated by the Z^0, W^+, and W^- bosons. These bosons interact with both quarks and leptons, and have been produced in high energy collisions.

They are some of the most massive particles in the SM: $M(Z) = 91.2$ GeV and $M(W) = 80.4$ GeV [3]. The weak force is unique because it is the only force that allows quarks to change their type, or "flavor". Up-type quarks can decay to down-type quarks (or vice versa) by exchanging virtual $W^{\pm}$ particles, although the large $W^{\pm}$ mass limits the range of these energy transfers to a small fraction of a femtometer [1]. The weak decay of bottom quarks to produce charm quarks, $b \to W^{-}c$ (Fig. 1.2), is the foundation of the decays studied in this analysis.

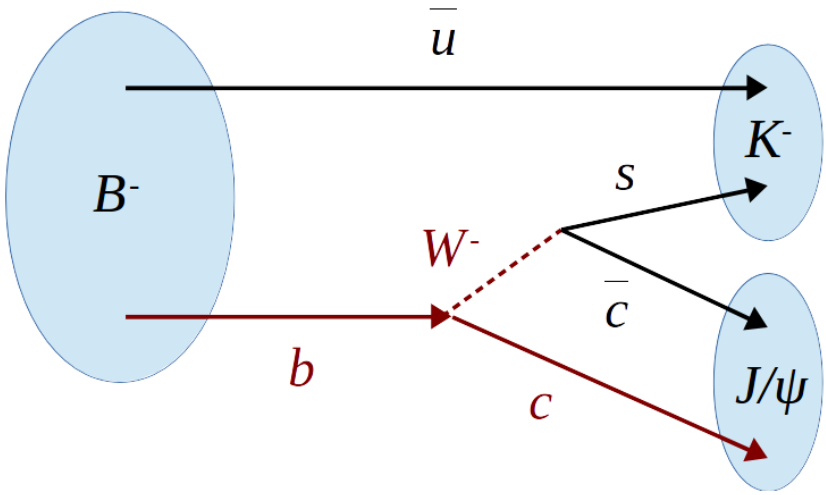

Figure 1.2 : Illustration of the $B^{\pm} \to J/\psi K^{\pm}$ decay, in which a b quark changes flavor through a weak decay.

Gluons, which mediate the strong nuclear force, are massless like photons. They transfer quanta of the strong force called "color charge" between quarks or other gluons. This system was introduced when the Δ^{++} baryon was discovered, containing three up quarks whose spins couple to give the Δ^{++} a spin of $+3/2$. This spin coupling is an example of a "symmetric"

state, meaning the three quark wave function is identical if any two of the quarks are swapped. Since these three quarks (fermions) could not occupy identical quantum mechanical states, another quantum classification had to exist which would make their wave function *anti*-symmetric, so that it changes sign when two quarks are swapped. The color labels are an analogy of light: a quark can be red (R), green (G), or blue (B). All stable quark combinations, called hadrons, are observed to be "colorless" (or white).

In quantum mechanics, color is treated as an SU(3) symmetry group, where colorless means that hadrons have color wave functions in the singlet state of the symmetry group. Quark-antiquark combinations, called mesons, have equal mixtures of color and anticolor: $(q\bar{q})_{\text{color singlet}} = (R\bar{R} + G\bar{G} + B\bar{B})/\sqrt{3}$. Hadrons with three quarks (or antiquarks) are called baryons and have equal mixtures of all colors (or anticolors) in a fully antisymmetric color singlet: $(qqq)_{\text{color singlet}} = [R(GB - BG) + G(BR - RB) + B(RG - GR)]/\sqrt{6}$.

One of the great successes of the Standard Model as a theory is its ability to unify the electromagnetic and weak forces into a joint symmetry group. In practice, this means that photons and weak bosons interact with the same particles because they are mixtures of more fundamental "electroweak" bosons. The standard model predicts a relationship between the weak boson masses and a mixing angle which has been confirmed by experiments [4]. Another important element of the Standard Model is electroweak symmetry breaking. To create a theory with massive weak bosons and a massless photon, symmetry of the electroweak field must be broken by choosing one of many possible ground states, or "gauges". The result of this process, called the Higgs mechanism, is an additional massive particle – the Higgs

boson. The Higgs boson (H^0) interacts with all particles, including itself, and the strength of these interactions determines what we observe as particle masses.

After many years of slowly eliminating possible H^0 masses, this elusive particle was discovered in 2012 by the experiments at CERN's Large Hadron Collider [5]. Its mass of 126 GeV, spin consistent with 0, and frequency of interactions with various particles indicate that H^0 follows the properties outlined by the standard model. Several theories that extend the standard model include multiple Higgs bosons, and for those particles the search continues.

There are still many physical concepts which the Standard Model cannot describe. An issue related to this analysis is CP violation. We observe that the universe is made up primarily of matter, which indicates that matter and antimatter must be produced or interact differently in some ways. These differences violate the fundamental symmetries of charge conjugation (C) and parity (P). The charge conjugation operation changes all particles to antiparticles, and vice versa. A parity operation flips the coordinate system: $(x,y,z) \rightarrow (-x,-y,-z)$. If CP symmetry is conserved, physics processes are identical after these two operations. The SM predicts some violation of CP symmetry, particularly in electroweak interactions, but not enough to understand the matter/antimatter imbalance we see today.

The SM will also require modification to include neutrino masses, which must be non-zero since we have observed neutrinos oscillating between flavors. Gravity is well understood on a macroscopic scale, but cannot be reconciled with the other known forces into a unified theoretical framework. Other cosmological phenomena such as dark matter and dark energy remain even more mysterious. The Standard Model has proved itself an excellent theory,

but the door to new discoveries is certainly not closed.

1.2 Bottom Quark Production at the Tevatron

Bottom quarks can be produced at the Tevatron in several ways. Quark-antiquark collisions can produce $b\bar{b}$ pairs by annihilation into photons, Z bosons, or gluons. Gluon collisions can also produce $b\bar{b}$ pairs. These processes account for ≈ 25 – 35% of b quarks produced at the Tevatron [6]. A similar fraction is created by gluon interactions after the primary $p\bar{p}$ interaction. The remaining fraction of b quarks are produced from scattering of quarks and gluons.

The theory of interactions between quarks and gluons, called quantum chromodynamics (QCD), is often treated as a perturbation theory where predictions are made by expanding the theory as a power series of the coupling strength between particles. The coupling strength is labeled α in quantum electrodynamics and α_s in QCD. The primary leading-order contribution ($\propto \alpha_s^2$) is refined and augmented by calculating higher order contributions ($\propto \alpha_s^3$, α_S^4, etc). Higher orders represent alternate paths from the same initial state to the same final state. A leading-order diagram for production of $b\bar{b}$ pairs at the Tevatron is shown in Fig. 1.3(a), and an example higher order diagram is shown in Fig. 1.3(b). Perturbation theory is an effective tool if the energy scale of the interaction is above the characteristic QCD mass scale $\Lambda \approx 210$ Mev [3]. The QCD coupling strength varies according to energy (Eq. 1.4) but is generally much larger than the electromagnetic coupling, $\alpha \approx 1/137$, which means that QCD perturbation series converge more slowly and often benefit from the

complex higher order calculations.

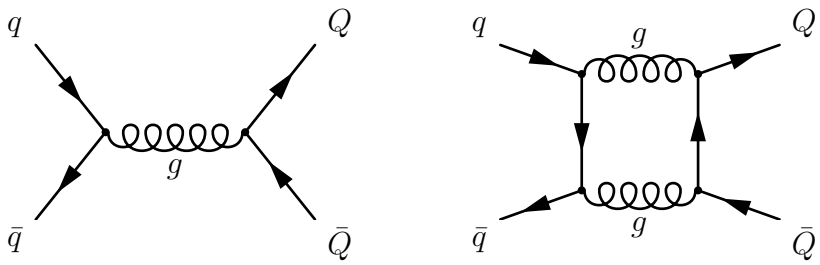

(a) (b)

Figure 1.3 : Example diagrams of the $q\bar{q} \rightarrow b\bar{b}$ process through (a) a "tree-level" interaction, and (b) a one-loop higher order interaction.

Like the fabled cat in the box that may (or may not) be dead, we cannot determine the exact process of an interaction. The final states from the diagrams in Fig. 1.3 are indistinguishable and there are an infinite number of other possible higher order contributions to the same process. Just as the cat is simultaneously alive and dead, we interpret the $p\bar{p} \rightarrow b\bar{b}$ process as simultaneously proceeding through all the possible paths. These paths are said to "interfere" with each other, and the overall cross section, or interaction probability, for producing the final state particles will have contributions from all the possible interactions. This analysis is particularly focused on how cross section contributions from various types of interactions affect the scattering angle distributions of the final state particles.

1.3 Forward-Backward Asymmetries

If a proton-antiproton collision reaches equilibrium the decay products will have no "memory" of the original p and $\bar{p}$ direction. By measuring a forward-backward asymmetry we are investigating whether or not heavy quarks have a preference to follow one of particle beams. If the SM accurately describes the interactions of quarks and gluons, then we expect a small positive asymmetry from the sources described below.

Over the past years there has been much interest in the forward-backward asymmetry in QCD $t\bar{t}$ production ($A_{\rm FB}^{t\bar{t}}$) [7], especially since initial experimental results were larger than standard model (SM) predictions [8, 9]. These observations prompted development of models beyond the SM that could explain the excess [10]. The corresponding asymmetry in $b\bar{b}$ production, $A_{\rm FB}^{b\bar{b}}$, has the same sources as $A_{\rm FB}^{t\bar{t}}$ but is expected to have a smaller magnitude in the SM, making it an important probe of these new physics models [11, 12]. However, the most recent D0 measurements of $A_{\rm FB}^{t\bar{t}}$ [13] agree with the SM [14].

In $p\bar{p}$ collisions, a forward-backward asymmetry in quark production is defined as: $A_{\rm FB}^{q\bar{q}} = (N_F - N_B)/(N_F + N_B)$. The forward category indicates a quark with the longitudinal component of its momentum in the direction of the proton beam, or an anti-quark with the longitudinal component of its momentum in the direction of the anti-proton beam. At the Tevatron, $A_{\rm FB}^{t\bar{t}}$ is measured by reconstructing the top quark and top antiquark and measuring their rapidities:

$$y = \frac{1}{2} \ln \left(\frac{E + p_z}{E - p_z} \right), \tag{1.1}$$

where E is a particle's energy and p_z is the component of its momentum in the direction of

the proton beam. The difference in rapidity between the top quark and top antiquark (Δy_t) is positive for forward events and negative for backward events. The asymmetry is:

$$A_{\mathrm{FB}}^{t\bar{t}} = \frac{N(\Delta y_t > 0) - N(\Delta y_t < 0)}{N(\Delta y_t > 0) + N(\Delta y_t) < 0}. \tag{1.2}$$

A closely related quantity called the $t\bar{t}$ charge asymmetry has been studied at the LHC [15, 16]. The LHC collides protons with protons, so there is no instinctive direction to label "forward". All $q\bar{q}$ interactions at the LHC are between a quark from one incoming proton and an antiquark that is produced by gluon interactions within the other proton. The quark is expected to have much higher momentum, so when $t\bar{t}$ pairs are produced the top quark is expected to have a broad rapidity distribution and the top antiquark is expected to have a narrower rapidity distribution. The LHC experiments measure the difference in the absolute values of the top and anti-top rapidities, $\Delta|y_t| = |y(t)| - |y(\bar{t})|$. The $t\bar{t}$ charge asymmetry, often referred to as a "forward-central" asymmetry, is defined as:

$$A_C = \frac{N(\Delta|y_t| > 0) - N(\Delta|y_t| < 0)}{N(\Delta|y_t| > 0) + N(\Delta|y_t| < 0)}. \tag{1.3}$$

The LHCb collaboration has recently measured the analogous charge asymmetry for b quarks, $A_C^{b\bar{b}}$ [17].

A forward-backward production asymmetry is caused by interference between various higher order processes. The gluon fusion process, $gg \to Q\bar{Q}$, is symmetric at all orders when quarks and antiquarks are switched, since protons and antiprotons have the same gluon content. In $Q \leftrightarrow \bar{Q}$ symmetric interferences all color charge elements change sign when Q and $\bar{Q}$ are switched, making the overall cross section contributions the same. The

$q\bar{q} \rightarrow Q\bar{Q}$ interaction has several possible non-symmetric interferences, where the cross section calculation contains color factors that do not change sign under the switch, making the cross section contributions different [18]. These non-symmetric interferences generate a forward-backward asymmetry that can be observed in the final state particles.

The dominant source of the forward-backward asymmetry is interference between tree-level and loop diagrams for $q\bar{q} \rightarrow Q\bar{Q}$ interactions, with additional contributions from interference between initial and final state gluon radiation [18]. These interfering diagrams are shown in Fig. 1.4.

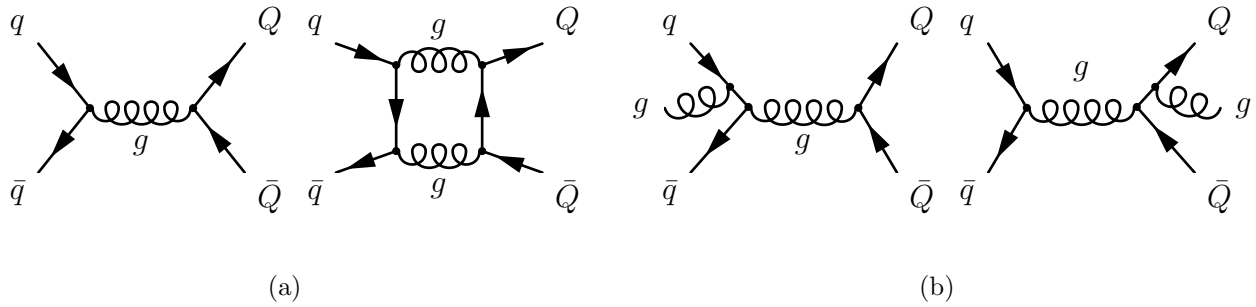

Figure 1.4 : Next-to-leading order diagrams which interfere to produce a forward-backward asymmetry in heavy quark production.

1.4 From b Quarks to B Mesons

While bottom quarks are produced very often in collisions at the Tevatron, it can be difficult to identify their properties directly. Bottom quarks go through a process called hadronization before they decay. Unlike the electromagnetic force, the strong force between two quarks does not become weaker as the particles move farther apart, it grows stronger. The strong

force couples particles with strength α_s:

$$\alpha_s(Q^2) = \frac{12\pi}{(33 - 2n_f)\log(Q^2/\Lambda^2)}, \tag{1.4}$$

where n_f is the number of quark flavors, Q^2 is the momentum transfer between particles, and Λ is the QCD mass scale [1]. Because of this relationship, quarks only move freely at very high energies across very small distance scales. At larger distances (where "large" means only tens of femtometers) the gluon coupling the two quarks has enough energy to split into a new quark-antiquark pair, effectively confining the quarks within bound states. The bound states, mesons and baryons, are colorless so they do not experience further strong interactions with other quarks or gluons. They remain bound together until they decay through other processes, such as the weak force.

The fragmentation of bottom quarks into a quagmire (or "jet") of mesons or baryons has been studied extensively at e^+e^- colliders and models were developed to describe the momentum and angular distributions of the hadrons created from an initial quark. At the Tevatron about 34% of b quarks hadronize to $B^\pm$ or B^0 mesons by combining with up or down quarks [3]. The $B^\pm$ meson has a rest mass of 5.279 GeV and a mean lifetime of 1.638 picoseconds, which means it travels far enough before decaying that its decay vertex can be distinguished from the $p\bar{p}$ vertex with current detector technology.

1.5 Measuring A_{FB} in $B^\pm \to J/\psi K^\pm$

We measure the forward-backward asymmetry using fully reconstructed $B^\pm \to J/\psi(\to \mu^+\mu^-)K^\pm$ decays where the $B^\pm$ directly identifies the quark flavor (i.e., b or $\bar{b}$). This decay,

shown in Fig. 1.2, occurs when a b quark decays to a W^- boson and a c quark. If the W^- decays to a $\bar{c}s$ pair, a J/ψ meson ($c\bar{c}$) and K^- meson ($s\bar{u}$) can be formed from the decay products and the $\bar{u}$ quark that was part of the original B^- meson. The B^+ meson decays in the same way, with all particles swapped for their antiparticles.

The strong force interactions that cause hadronization proceed more quickly than b quark decays through the weak force, so most b quarks will form B hadrons before they decay. This makes the quantity $A_{\rm FB}(B^{\pm})$ sensitive to the same production asymmetries as $A_{\rm FB}^{b\bar{b}}$ since, to a large extent, the b quark's momentum and direction are preserved in the $B^{\pm}$ meson.

Compared to b jet reconstruction, reconstructing $B^{\pm}$ decays has the advantages that the charge of the b quark is unambiguously determined, and there is no need to account for oscillations which occur in the neutral B meson system through box diagrams similar to Fig. 1.3(b). Flavor identification in b jets often involves finding a charged lepton, such as a muon, and inferring whether it came from a b or $\bar{b}$ decay. In the $b \to W^-c$ example, the W^- decay can produce a negative muon: $W^- \to \mu^-\bar{\nu}_{\mu}$. This charge correlation can be obscured by $B^0/\bar{B}^0$ oscillations where the b oscillates to a $\bar{b}$ before decaying, which could create a positive or "wrong" charge muon. Sequential weak decays such as $b \to W^-c$ followed by $c \to W^+s$ can also cause misidentification. If the W^+ decay creates the muon tagged in the jet, it will have the wrong sign to correctly identify b or $\bar{b}$. Correcting for these misidentification probabilities generally introduces substantial systematic uncertainties to a measurement. Reconstructing charged $B^{\pm}$ mesons avoids this difficulty, but with the drawback of limiting the energy range of the initial $b\bar{b}$ pair. At lower energies there is

a greater probability that $b\bar{b}$ pairs are produced from gluon interactions rather than $q\bar{q}$ interactions.

We reconstruct $B^{\pm}$ mesons and categorize them as forward or backward with a variable $q_{FB} = -q_B \,\mathrm{sgn}(\eta_B)$, where q_B is the electric charge of the $B^{\pm}$ mesons, $\mathrm{sgn}(x)$ is the sign function, and η_B is the pseudorapidity of the $B^{\pm}$. DØ defines a coordinate system with the z axis along the proton beam direction, the x axis pointing away from the Tevatron center, and the y axis pointing upwards. Pseudorapidity is defined as $\eta = -\ln[\tan(\theta/2)]$, where θ is the laboratory frame polar angle. Angle ϕ is the azimuthal angle in the x-y plane.

Figure 1.5 gives examples of the forward and backward categories. The forward-backward asymmetry of the $B^{\pm}$ mesons is:

$$A_{FB}(B^{\pm}) = \frac{N(-q_B\eta_B > 0) - N(-q_B\eta_B < 0)}{N(-q_B\eta_B > 0) + N(-q_B\eta_B < 0)}. \tag{1.5}$$

1.6 Theoretical Predictions

Until recently, theoretical predictions of $A_{\mathrm{FB}}^{b\bar{b}}$ in QCD production were limited [18]. But interest in $t\bar{t}$ asymmetry measurements has lead to new predictions of $A_{\mathrm{FB}}^{b\bar{b}}$ in the standard model and several new physics models. Inclusive predictions of $A_{\mathrm{FB}}^{b\bar{b}}$ give positive asymmetries of $\approx 0.5\%$ [11, 19], but the mass scales of the $b\bar{b}$ pairs considered ($M(b\bar{b}) > 35$ GeV, or $p(b) > \approx 15$ GeV) are more relevant for a jet-based analysis.

In the $b\bar{b}$ mass range which overlaps the most with data used in this analysis, $35 \leq M(b\bar{b}) < 75$ GeV, [11] predicts $A_{\mathrm{FB}}^{b\bar{b}} = (0.34 \pm 0.10 \pm 0.01)\%$. The asymmetry increases to $\approx 2\%$ – 4% at masses near and above $M(b\bar{b}) = M(Z^0)$. Several new physics models which

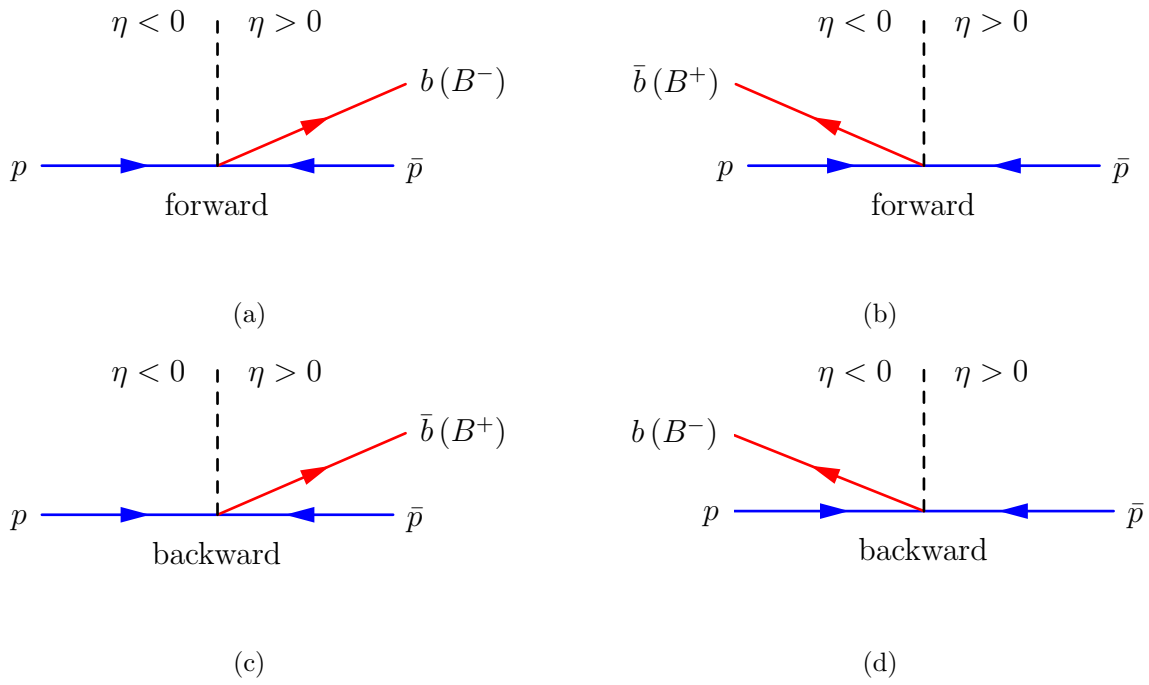

Figure 1.5 : Diagrams illustrating the definitions of (a, b) forward particles with $q_{\mathrm{FB}} = +1$ and (c, d) backward particles with $q_{\mathrm{FB}} = -1$.

give non-SM values of $A_{\rm FB}^{b\bar{b}}$ while agreeing with experimental results for $A_{\rm FB}^{t\bar{t}}$ are shown in Fig. 1.6 [11]. These models predict a new physics particle which could replace the gluons in Fig. 1.4 and create interference patterns which raise or lower the value of $A_{\rm FB}^{b\bar{b}}$ compared to the SM value. In the 35 – 75 GeV mass range (the first bin) asymmetries from the new physics models range from $\approx 0\% - 0.8\%$.

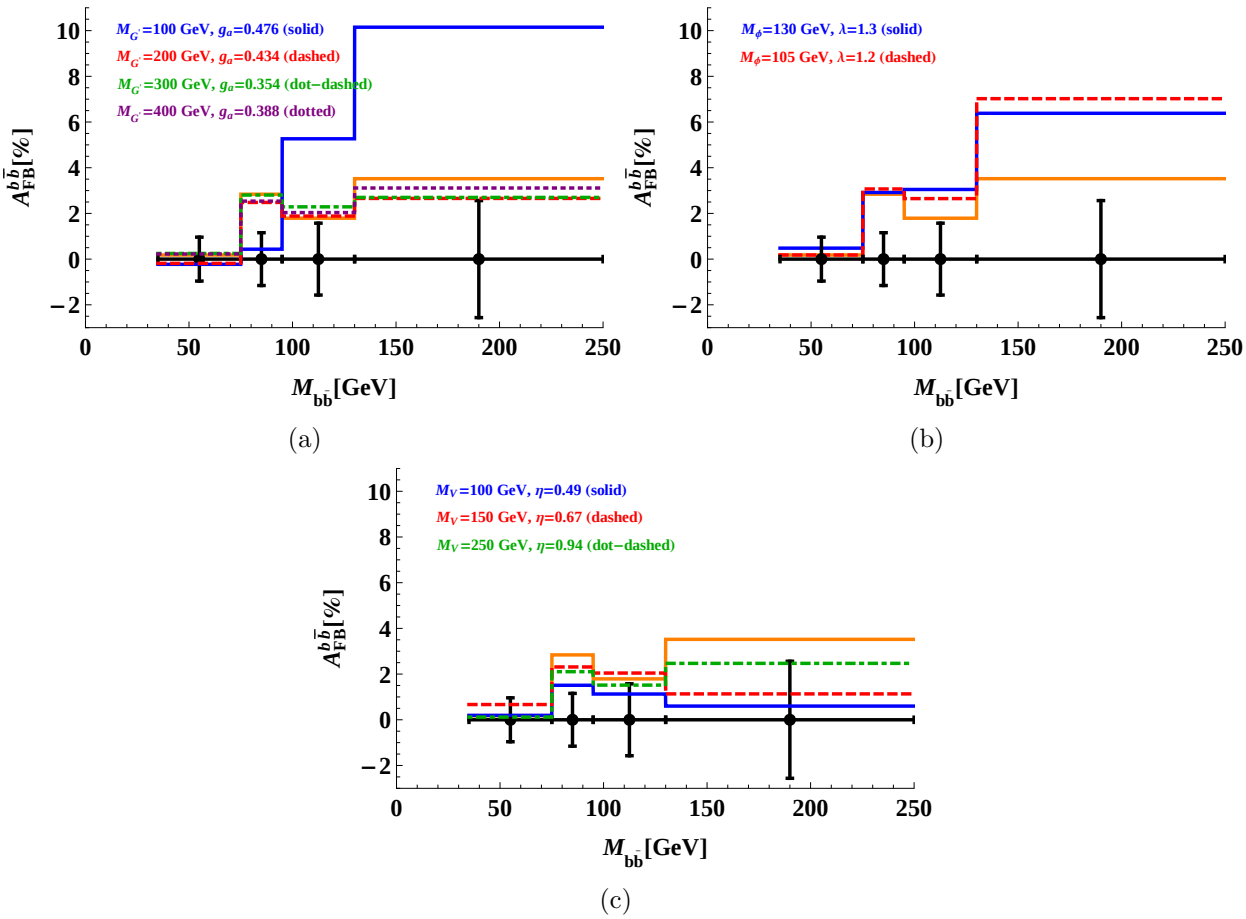

Figure 1.6 : Predictions of $A_{\rm FB}^{b\bar{b}}$ in the SM (orange) compared to new physics models: (a) an axigluon G' (b) a scalar weak doublet ϕ, and (c) a flavor octet vector V. Black points represent expected experimental sensitivity in a jet-based analysis. Figures from [11].

Since no SM predictions exist for $A_{\rm FB}(B^{\pm})$, we make predictions tailored to our kine-

matics and selections by producing next-to-leading-order Monte Carlo (MC) samples for QCD production of $B^{\pm}$ in the process $p\bar{p} \to b\bar{b}X$. This simulation also allows us to compare the $B^{\pm}$ system to the $b\,(\bar{b})$ system. MC events are generated using MC@NLO [20] with parton distribution function set CTEQ6M1 [21] and HERWIG [22] for parton showering and hadronization. Detector simulation is performed using GEANT3 [23]. The analysis of this simulation is presented in Chapter 6.

Chapter 2

Colliding Beams and Detecting Particles

The Fermi National Accelerator Laboratory (Fermilab) is a United States Department of Energy laboratory in Batavia, Illinois, where a wide range of particle physics experiments are conducted. Until the LHC began running in 2009, Fermilab boasted the largest and most energetic particle accelerator system in the world. The physics program, which was always diverse, is now focused strongly on experiments designed to detect neutrinos. These experiments will (hopefully) uncover missing elements of the standard model such as neutrino mass ordering and CP violation [24]. Two precision muon experiments in development will probe the existence of new physics at mass scales far beyond the reach of collider detectors [25].

But as these new experiments progress, the Tevatron collaborations have continued producing physics results in the three years post shutdown. Legacy measurements from the Tevatron will influence the particle physics community for a long time to come. The DØ detector may be inactive, but is has not closed its doors: more than 2500 students, scientists, teachers, and members of the public have walked through the detector and the adjacent Tevatron tunnel to learn about particle physics and detector technologies.

2.1 Accelerators at Fermilab

A long chain of accelerators lies behind the physics knowledge that has emerged from 20+ years of running detectors like DØ. The Tevatron was supported by a series of accelerators, shown in Fig. 2.1, which worked together to produce and accelerate protons and antiprotons [26].

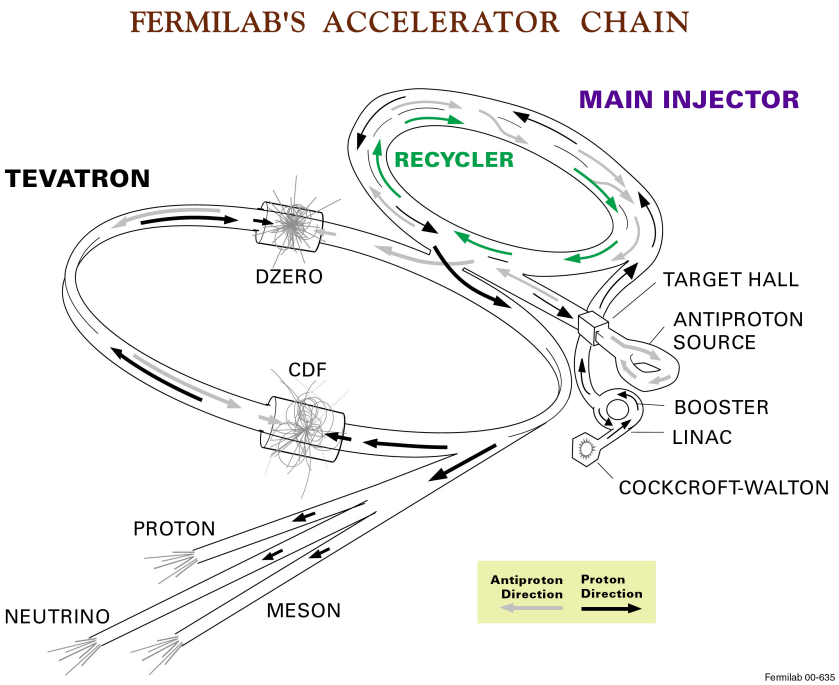

Figure 2.1 : Overview of the accelerator system at Fermilab.

The chain began with a collection of Cockcroft-Walton accelerators, which feature columns supporting large domes charged to -750 kV where hydrogen atoms pick up electrons to become H^- ions. The ions drift through the electric field and accelerate to an energy of 750 keV as they move down the columns to electrical ground. The ions are then transfered to

the Linac, or linear accelerator, which uses a series of 12 radio frequency (RF) cavities to increase the ions' energy to 400 MeV. An RF cavity is a metal annulus around the beam pipe which creates a gap where an electric field can be applied to the beam, increasing the kinetic energy. The applied electric field and induced magnetic field of the cavity are in resonance with each other at a frequency designed to be in the radio range of the electromagnetic spectrum. The Linac uses increasingly longer drift tubes between cavities so that as the particles accelerate they never cross a cavity when the electric field opposes their direction of motion. The Linac then sends 400 MeV H^- ions to the Booster, and also sends 66 MeV ions to Fermilab's Neutron Therapy Facility where neutrons are produced for medical radiation treatments.

In the Booster the H^- ions are stripped of their electrons and the resulting protons are accelerated to an energy of 8 GeV. The Booster is the first circular "synchrotron" accelerator in the chain and has 19 RF cavities. Accelerators like the Booster are called synchrotrons because the RF cavity frequencies must increase in sync with the growing beam energy to protect the particles from opposing electric fields, like the lengthening drift tubes in the Linac. Dipole magnets bend the beam particles into a circular pattern, and the field strength is also ramped up in sync with the particles' acceleration so that the radius of curvature remains the same. Particles in the beam continually gain energy until the RF cavities' frequency is set so that the beam crosses the cavities when the electric field is zero. This allows a single ring to both accelerate particles and store them at the desired energy. The Booster transfers 8 GeV protons to the Main Injector or to fixed targets for production of neutrino beams.

The Main Injector is a much larger circular synchrotron which has 18 RF cavities, accelerating protons to 150 GeV for the Tevatron and 120 GeV for producing antiprotons and secondary beams such as kaons, pions, muons, or neutrinos. Antiprotons are produced when the 120 GeV proton beam strikes a nickel target and magnets are used to isolate 8 GeV antiprotons from the spray of collision products. The antiprotons go through several stages of "cooling" which make the beam more uniform in both space and momentum. Lower intensity antiproton beams undergo stochastic cooling in the Antiproton Source, and are then transfered to the Recycler, a storage ring which shares the Main Injector Tunnel. The higher intensity antiproton beams in the Recycler are cooled using electron cooling, where an electron beam is laid over the antiproton beam so that collisions filter out the unfocused beam particles. Finally, the antiprotons are returned to the Main Injector for acceleration to 150 GeV and injection into the Tevatron.

The Tevatron is the most well known of Fermilab's accelerators. It has a one kilometer radius and the protective berm is a well known landmark. Superconducting niobium-titanium magnets, cryogenically cooled to near four degrees Kelvin with liquid helium, bend and focus the particle beams, which are accelerated through 8 RF cavities to 980 GeV. The ring consists of dipole and quadrapole magnets arranged in a repeating lattice, with four dipole magnets between each quadrapole. The dipole magnets direct the beam into a circluar path, and the quadrapole magnets are responsible for focusing the beam in either the x or y planes. The focusing direction is alternated at each quadrapole magnet around the ring so the combination produces a universally focused beam.

The proton and antiproton beams are directed so that they collide in two detectors: the Collider Detector at Fermilab (CDF), and DØ (named for its position on the Tevatron ring). The accelerator complex was developed over many years and represents an enormous engineering achievement. The Tevatron run ended in September 2011 after the detectors recorded more than 10 fb^{-1} of integrated luminosity, or about five trillion collisions [27].

2.2 The DØ Detector

The DØ detector is located on the southeast portion of Fermilab's Tevatron accelerator. The first data-taking run lasted from 1992 – 1996, during which time DØ recorded 120 pb^{-1} of data at a center of mass energy of 1.8 TeV. The top quark was discovered by the Tevatron experiments during this time [28], and the record of high precision measurements of the W boson mass began [29]. From 1996 – 2001 the detector was upgraded for Run II, which lasted from 2002 – 2011 and is the data of interest for this analysis. DØ is a standard example of modern hadron collider detectors: the beampipe sits inside a tube of tracking detectors surrounded by electromagnetic and hadronic calorimeters and a muon tracking system (Fig. 2.2) [30].

2.2.1 Central tracking system

The first detector element which particles from a collision encounter is the silicon microstrip tracker (SMT) [31]. The SMT is a system of barrels and disks mounted with silicon sensors, shown in Fig. 2.3(a). This detector was added to DØ for Run II, and identifies particle

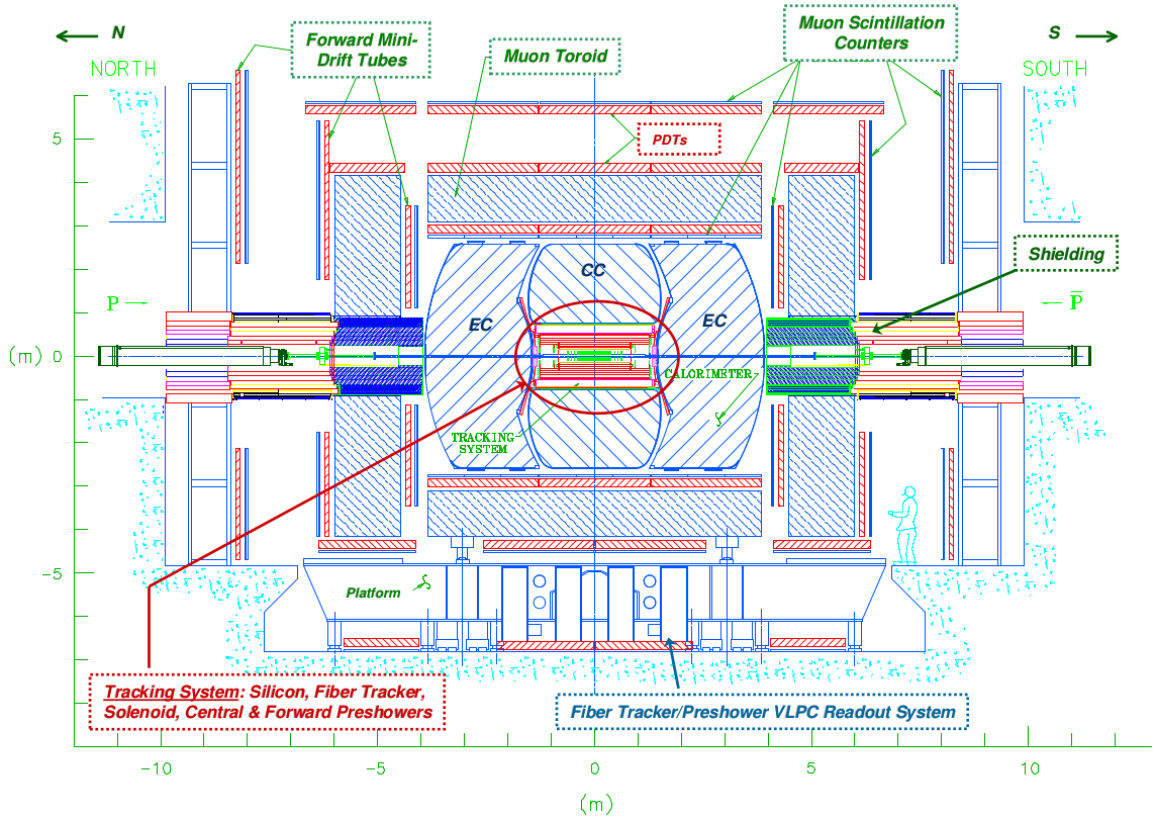

Figure 2.2 : View of the full DØ detector in the $y-z$ plane showing the beampipe, central tracking, calorimetry, and muon system.

interaction vertices to a precision of 15 μm at the center of the detector. The primary $p\bar{p}$ interaction vertex can be located with a precision of $\approx$ 35 μm along the beam axis. This resolution is sufficient to separate b quark decay vertices from the primary $p\bar{p}$ vertex. The SMT covers a wide range of pseudorapidity, out to $|\eta| < 3$, so that SMT tracks can be matched to calorimeter energy clusters and tracks in the muon system. An upgrade during Run II called "Layer 0" added two more layers of silicon sensors at a radius of $\approx$ 17 mm from the beam axis. These extra layers were especially useful for improving the impact parameter resolution of low momentum tracks [32] and increasing the efficiency of b quark identification.

The second layer of the central tracking system is the central fiber tracker (CFT), illustrated in Fig. 2.3(b). The CFT consists of polystyrene scintillating fibers that are 830 microns in diameter, mounted on four concentric carbon fiber cylinders. The cylinders are placed outside the SMT and range in radius from 20 – 52 cm. Fiber direction is alternated so that two layers of fibers lie along the beam direction and the the next two layers are offset by small positive or negative stereo angles to provide a measurement of the z coordinate of the track. The CFT measures track position with a resolution of about 100 μm.

Charged particles moving through the tracking detectors leave small amounts of ionizing radiation behind, which are detected by sensitive amplifiers in the SMT readout chips and by light produced in the CFT scintillators. Photons produced in the CFT fibers are carried to Visible Light Photon Counters (VLPCs) which convert photons to electrical signals. The VLPCs are operated at 9K and are capable of converting single photons to electrons with an

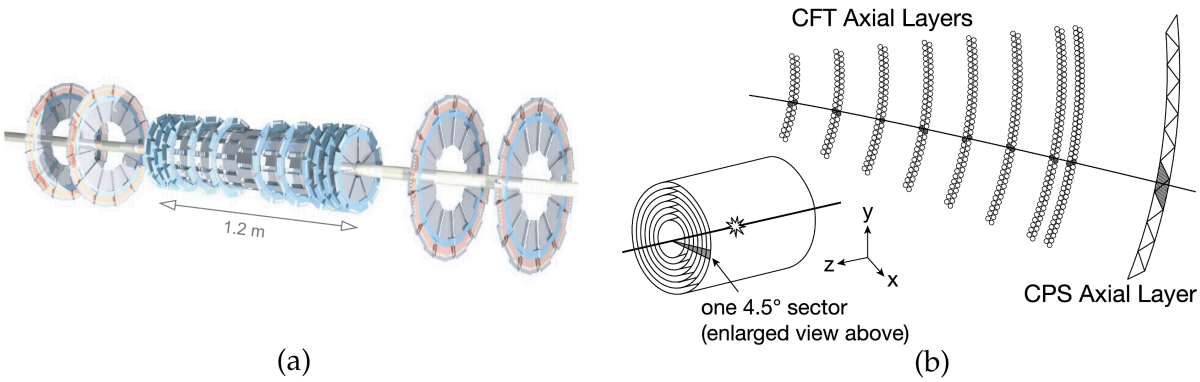

Figure 2.3 : Illustrations of (a) the SMT detector and (b) a path through the CFT layers.

efficiency of greater than 75%. Signals, or "hits", from the tracking detectors are connected along a path to form a particle track. The amount of matter which particles pass through in the tracking detector is small, with all the CFT layers making up only 20% of one radiation length. The CFT is optimized for tracking out to pseudorapidity $|\eta| < 2.5$.

Both layers of tracking detectors are encased in a ≈ 1.9 T solenoid magnet which can be operated with positive or negative polarity. Tracking a particle's motion through the magnetic field gives information about electric charge and momentum, which drastically improved DØ's performance in Run II over Run I, when the detector had no magnetic field in its tracker.

2.2.2 Preshower detectors

Outside the central tracking system and solenoid magnet are the central preshower (CPS) and forward preshower (FPS) detectors. These detectors act as a combination of trackers and calorimeters, and help match tracks to the calorimeter showers. They are designed to

contain approximately two radiation lengths of material which will spark electromagnetic showers from electrons and photons. The CPS is made of triangular scintillator strips which are interlaced so that tracks hit multiple strips and there is no dead space. The FPS has three layers: a minimum ionizing particle (MIP) layer where most particles deposit a relatively small amount of energy for each unit of distance they travel, a steel absorber layer, and a shower layer where electrons and photons will leave showers while hadronic particles and muons continue traveling through as MIPs. These different types of behavior in the preshower detectors provide valuable information for particle identification.

2.2.3 Calorimeters

DØ's real "workhorse" detector is a series of liquid argon sampling calorimeters, shown in Fig. 2.4. Short distance electric fields are created across a few millimeters of liquid argon by grounding heavy metal absorber plates and connecting electronic readout boards to a high voltage. Shower particles created in the absorber plates ionize liquid argon atoms. Ionization electrons drift through the electric field across the liquid argon gap to the readout boards so their energy can be measured. The innermost calorimeter is the electromagnetic calorimeter with 3-4 mm uranium absorber plates. As electrons and photons move through the electric fields around atomic nuclei they create showers of other electromagnetic particles through a combination of bremsstrahlung and e^-e^+ pair production, spreading the initial particle's energy across many shower particles. The number of particles in the shower is proportional to the energy of the original particle, allowing a measurement of its energy.

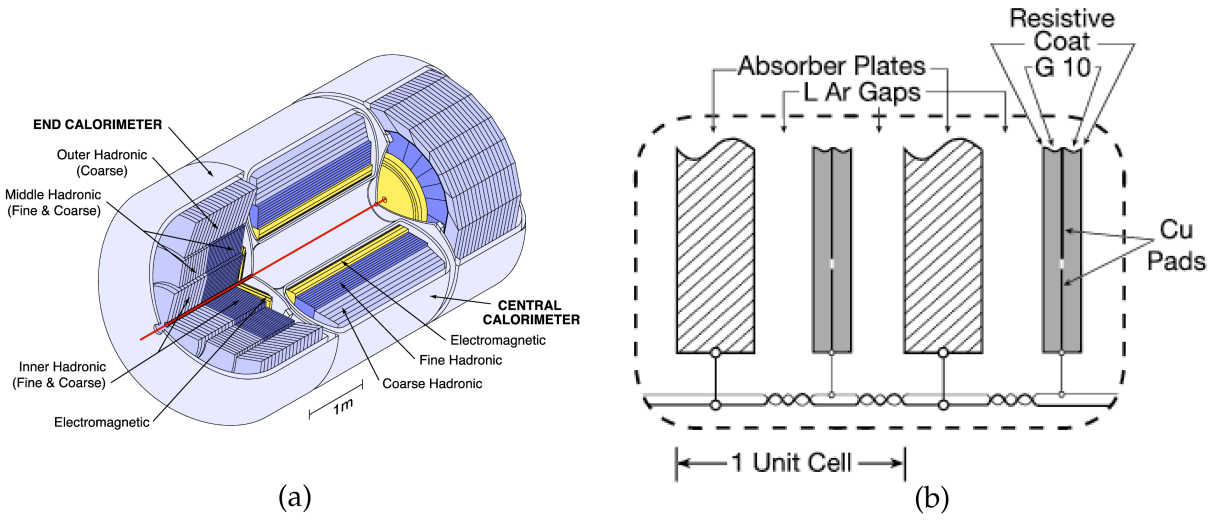

Figure 2.4 : Illustrations of (a) the calorimeter sections and (b) a calorimeter unit cell.

Hadrons also form showers as they move through detector material, mainly through hadronic interactions with atomic nuclei. These showers are more broadly distributed than electromagnetic showers and the measurement of the original particle's energy is not as precise. The outer calorimeter layer has two segments for detecting hadronic showers: the fine and coarse hadronic calorimeters (FH, CH). The FH calorimeter has thicker absorber plates, 6 mm uranium-niobium alloy, in which hadronic particles begin showers. The CH calorimeter's plates are much thicker, 46 mm, and made of copper or stainless steel. While traveling through the calorimeter all hadronic particles will shower into cone-shaped clusters of energy. Collections of closely spaced showers form jets which are used to trace hadronic particles back to the original quarks from a collision and estimate their energies.

The calorimeter is split into three sections: a central barrel covering $|\eta| < 1$ and two symmetric endcaps to extend coverage to $|\eta| < 4$. To maintain the 90K liquid argon temper-

ature three separate cryostats are needed. Just inside each cryostat, outside the first layer of uranium, are subdetectors called the massless gaps, which are essentially one calorimeter readout cell. In between the cryostats are the intercryostat detectors which are made of scintillating tiles in light-tight aluminum boxes. The light from particles impacting the scintillator is directed through wavelength shifting fibers to photomultiplier tubes. These smaller subdetectors help improve the hermicity of DØ.

2.2.4 Luminosity monitors

The luminosity monitors, illustrated in Fig. 2.5, are two arrays of twenty-four scintillating plastic pieces and photomultiplier tubes which are mounted around the beampipe next to the endcap calorimeters ($2.7 < |\eta| < 4.4$). They measure $p\bar{p}$ inelastic scattering to calculate the number of collisions in the detector as well as to monitor unfocused beam "halo" backgrounds. Luminosity is defined as:

$$L = \frac{1}{\sigma_{LM}} \frac{dN}{dt}, \tag{2.1}$$

where dN/dt describes the rate of coincident particles in both luminosity monitors, and σ_{LM} is a constant describing the effective inelastic cross section of the luminosity monitor [27]. The integral of L over some period of time is a measure of the total number of collisions, in the bizarre unit of "inverse barns", which provides a normalization value for the DØ data sample. All the inner elements of DØ are shown in Fig. 2.6.

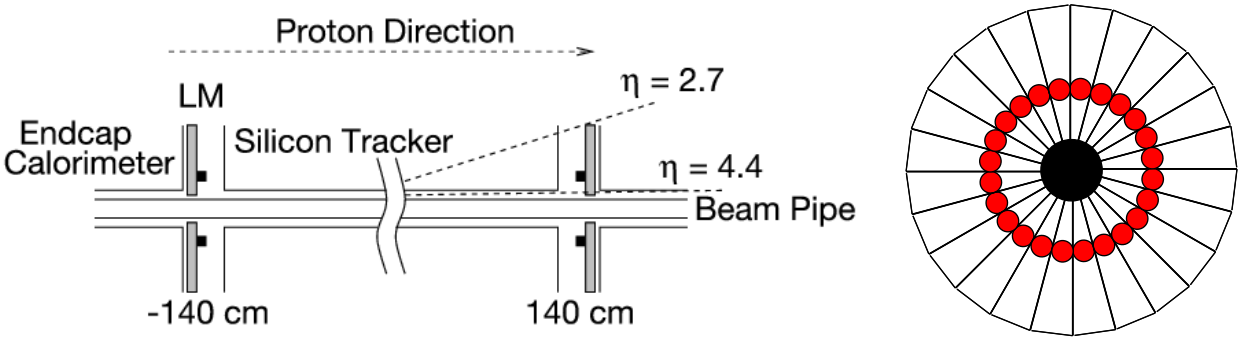

(a) (b)

Figure 2.5 : Illustrations of (a) the placement and (b) the layout of the luminosity monitors, with plastic scintillator (white trapezoids) and photomultiplier tubes (red dots).

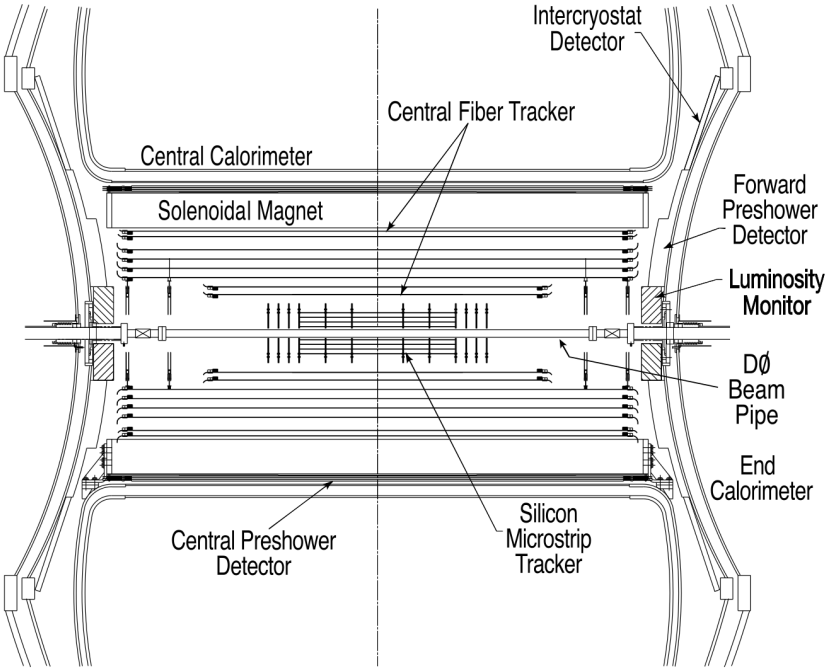

Figure 2.6 : Close up view of the central region of the DØ detector showing the SMT, CFT, solenoid, preshower detectors, luminosity monitors, and intercryostat detectors.

2.2.5 Muon tracking systems

The muon tracking system [33] is the exterior layer of the DØ detector and tracks the momentum of muons, the only charged particles which travel through all the tracking and calorimeter layers without stopping. Muons are more massive than electrons, so they interact with matter quite differently. In particular, energy lost to photon radiation through the bremsstrahlung process is many orders of magnitude smaller for muons than electrons.

The muon system has one layer within a 1.8 T iron toroid magnet and two more layers outside the toroid (Fig. 2.7). An important measure of a reconstructed muon's quality is how many (and which) layers of the muon system it encounters. Drift tubes and scintillation counters are used to make an independent momentum measurement which helps match muon tracks to central detector tracks, and improves the muon momentum resolution. The muon tracking system for DØ was specially designed with a wide pseudorapidity coverage, out to $|\eta| \approx 2$, creating a large data sample for b quark decays which frequently include muons.

The polarities of both the central tracking solenoid and the muon system toroids were reversed approximately every two weeks so that all four solenoid/toroid polarity combinations received nearly equal beam exposure. A track which is reconstructed with a certain sign of curvature will represent a positive particle in one polarity and a negative particle in the opposite polarity. Reversing the polarities means that any detector inefficiencies will affect both charges equally, removing first-order charge asymmetries from the tracking detectors.

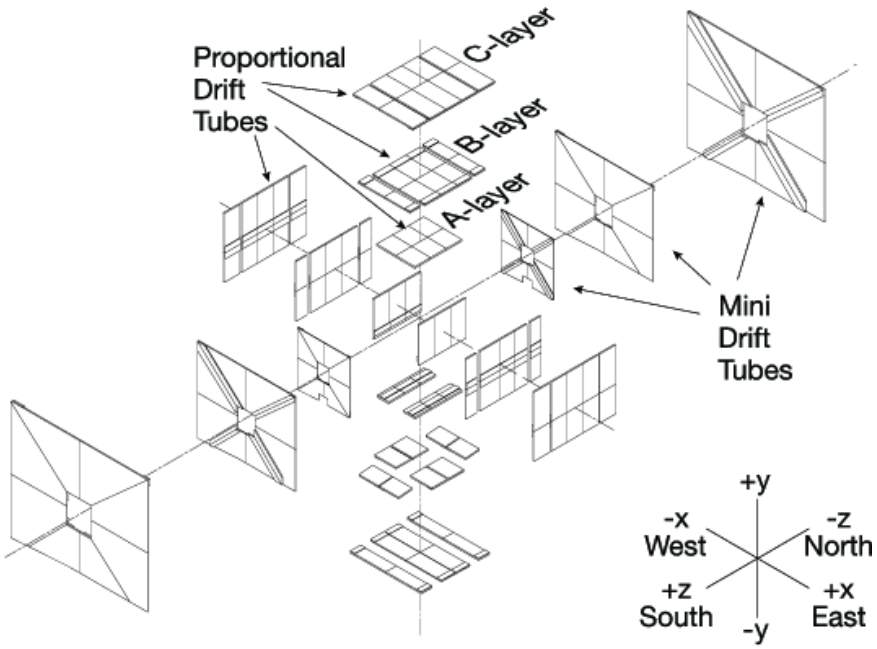

Figure 2.7 : The muon tracking system drift tubes.

2.2.6 Triggers and data reconstruction

Collisions are processed through three levels of triggers (Fig. 2.8) to collect events with interesting physics processes and reduce the massive stream of data to a manageable rate. The first level is a series of hardware triggers which make decisions to keep or reject events based on calorimeter energy deposits or track momentum above certain thresholds. These triggers accept an average of 2000 events per second, or a rate of 2 kHz. The second trigger level combines hardware triggers with computer processors which can form physics objects such as leptons or quark jets, match tracks to calorimeter clusters, and calculate quantities such as missing transverse energy or a track's impact parameter with the beam. This information is used to look for known signatures across the subdetectors and reduce

the accepted event rate by half. The Level 3 trigger is a farm of microprocessors which make more detailed calculations and study relationships between objects in the event to reduce the acceptance rate to 50 – 100 Hz. This final output rate is acceptable for the tape record system and promotes high quality physics data samples.

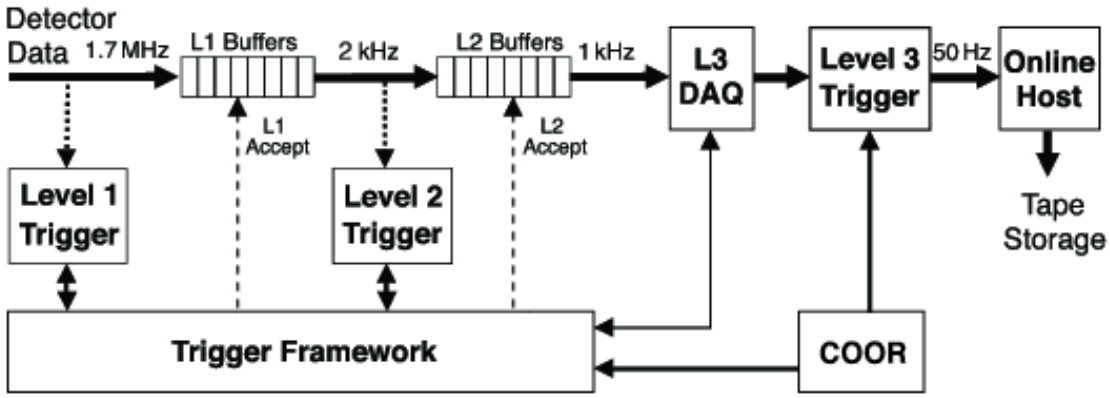

Figure 2.8 : Graphical outline of the trigger framework.

Events passing all three trigger levels are processed through DØ's reconstruction algorithms which create physics objects (tracks, jets, leptons, etc) from tracker hits or calorimeter energy deposits. The data can be broken up based on information from the trigger framework into smaller samples containing events with similar objects or conditions. The data used for this analysis require single muon or dimuon triggers since muons are a final state particle in a vast array of heavy flavor decays.

DØ collected data with very high efficiency while the Tevatron was running. Several shutdown periods for upgrades or maintenance are used to mark divisions in the data. Run IIa refers to the first 1.1 fb^{-1} of luminosity collected before the upgrade of the tracking

detector in 2006. All the data collected from 2006 – 2011 is called Run IIb, which is further split into four subsets: Run IIb1, Run IIb2, etc (Fig. 2.9). Of the 11.9 fb^{-1} of integrated luminosity delivered by the Tevatron, DØ recorded 10.7 fb^{-1}. All the data is monitored for quality control in the various detector components. In this analysis we use data passing quality control cuts for the central tracking and muon systems; a total to 10.4 fb^{-1}.

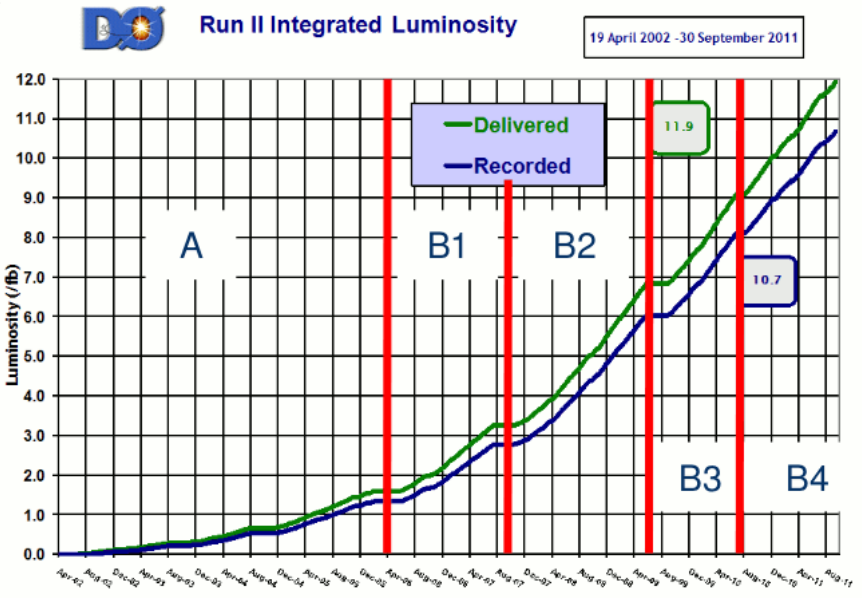

Figure 2.9 : Delivered and recorded luminosity of Run II.

Chapter 3

Finding $B^{\pm} \to J/\psi K^{\pm}$

3.1 Data Samples and Event Selection

We select events containing $B^{\pm} \to J/\psi K^{\pm}$ candidates from the full DØ Run II dataset, using data samples in which each event contains at least one muon. The DØ flavor physics software framework reads data events and constructs a "box" of particles which can be passed through selection criteria to find decays of interest based on their kinematics.

Candidate $B^{\pm} \to J/\psi K^{\pm}$ decays are reconstructed by identifying a pair of oppositely charged muons (decay products of the J/ψ meson) which meet a charged track (the $K^{\pm}$ candidate) at a common vertex which is significantly displaced from the $p\bar{p}$ interaction vertex. In each event the $p\bar{p}$ interaction vertex is identified by calculating the position which minimizes the distance between all tracks which pass the beam intersection point within 0.2cm.

The first pass through the box of particles determines which pairs of muons form J/ψ candidates. Muon track segments are reconstructed in the three layers of the muon tracking system, and the segments are joined into a track. The trajectory can be extrapolated back toward the center of the detector and matched with a track reconstructed from hits in the central tracking system. The resulting muon object has information from both tracking

systems. The muons must be oppositely charged and lie within the coverage regions of the central and muon tracking systems, $|\eta| < 2.1$. They must have transverse momentum $p_T > 1.5$ GeV/c and at least two hits in each of the SMT and CFT detectors. At least one of the muons must have reconstructed segments in both the inner and outer layers of the muon tracking system. Finally, the differences in $z(\mu)$, $\phi(\mu)$, and $\eta(\mu)$ between the central and muon trackers must match the following criteria: $\Delta z(\mu) < 100$ cm, $\Delta\phi(\mu) < 0.4$ rad, and $\Delta\eta(\mu) < 0.6$.

If a muon pair meets these criteria, a J/ψ candidate is formed at the $\mu^+\mu^-$ vertex. The vertex algorithm finds the distance of closest approach between the two muons tracks, extrapolating back toward the $p\bar{p}$ vertex if necessary, and averages the track position vectors to assign a vertex point. Vertices which are actually just track crossings are rejected by requiring less than two total hits (on both muon tracks combined) located between the $p\bar{p}$ vertex and the J/ψ vertex. The algorithm also sets a limit on how much extrapolation of the track trajectories is allowed: the muon tracks must begin within four central tracking detector layers of the J/ψ vertex.

J/ψ candidates with invariant mass from 2.7 to 3.45 GeV/c^2 are accepted. The invariant mass is calculated from the known mass (m_μ) and measured momentum vectors ($\vec{\mathbf{p}}_{\mu_1}$, $\vec{\mathbf{p}}_{\mu_2}$) of the muons:

$$M(J/\psi) = \sqrt{(E_{\mu_1} + E_{\mu_2})^2 - (\vec{\mathbf{p}}_{\mu_1} + \vec{\mathbf{p}}_{\mu_2})^2}, \tag{3.1}$$

$$E_\mu = \sqrt{m_\mu^2 + |\vec{\mathbf{p}}_\mu|^2}. \tag{3.2}$$

The distance from the $p\bar{p}$ vertex to the $J/\psi \to \mu^+\mu^-$ vertex in the x-y plane is called the

transverse decay length, L_{xy}. The decay length $L_{xy}(J/\psi)$ must have uncertainty less than 0.1 cm. Particles reconstructed with momentum vectors which point back toward the $p\bar{p}$ vertex are removed by a cut on the pointing angle, which is the angle between a particle's momentum vector and the vector from the $p\bar{p}$ vertex to the particle's decay vertex. This angle can be calculated from either two- or three-dimensional vectors. The cosine of the J/ψ meson's two-dimensional pointing angle must be greater than zero.

With each of the J/ψ candidates we take another pass through the box of particles to choose kaon candidates. The $K^{\pm}$ track must have $|\eta| < 2.1$ and $p_T > 0.7$ GeV/c. If the $K^{\pm}$ candidate meets the μ^+ and μ^- tracks at a common vertex, a $B^{\pm}$ candidate is formed. Since DØ cannot distinguish between charged hadrons we assign the kaon mass of 0.494 GeV to the $K^{\pm}$ candidate track in order to calculate the $B^{\pm}$ candidate mass. We constrain the $\mu^+\mu^-$ invariant mass to the world average of $M(J/\psi) = 3.097$ GeV [3] by correcting the muon momenta. The $B^{\pm}$ candidate invariant mass is then calculated by combining the masses and momenta of these three particles, as in equation 3.1. Candidates with mass from 4.0 to 7.0 GeV/c^2 are accepted.

The $B^{\pm}$ vertex is a combination of three tracks, formed in the same way as the J/ψ vertex. Each track will be slightly displaced from the vertex position so a χ^2 statistic is constructed by adding in quadrature the displacement for each track divided by its uncertainty. The combination of μ^+, μ^-, and $K^{\pm}$ tracks to form the $B^{\pm}$ meson vertex must have $\chi^2 < 16$ for three degrees of freedom. The cosine of the $B^{\pm}$ meson pointing angle is required to be above 0.8. Finally, the $B^{\pm}$ transverse decay length significance, defined as $\mathcal{S}_{xy} = L_{xy}/\sigma(L_{xy})$, must

be greater than 3. This displacement of the $B^{\pm}$ decay from the $p\bar{p}$ vertex is an essential identifier of $B^{\pm}$ candidates.

Because the definitions of forward and backward are tied directly to $\mathrm{sgn}(\eta_B)$, the ambiguous region near $\eta = 0$ must be considered. Simulated MC events provide two levels of particle information: generated particles with kinematic properties based only on the physics processes which created them, and reconstructed particles which have been processed through the detector simulation. To determine the effect of the detector material on the η_B measurement we compare the quantity at generation level and reconstruction level. The sample of MC@NLO events is passed through the $B^{\pm} \to J/\psi K^{\pm}$ selection described above and the reconstructed muon and kaon tracks are matched kinematically to $B^{\pm} \to J/\psi K^{\pm}$ decays from the MC generator. This matching removes all background events from the MC sample. Based on the range of $\eta_B(\text{generated}) - \eta_B(\text{reconstructed})$, shown in Fig. 3.1(a), we reject $B^{\pm}$ candidates with $|\eta_B| < 0.1$. This cut removes all $B^{\pm}$ mesons reconstructed with incorrect q_{FB} while rejecting only 2% of the data sample.

We can also compare the difference between the direction of the reconstructed $B^{\pm}$ meson and its parent $b(\bar{b})$ quark. To simulate the reconstruction of b jets, we choose the MC b particle produced closest to the $p\bar{p}$ interaction which has a maximum distance from the $B^{\pm}$ meson of $\Delta\mathcal{R} = 0.5$, where $\Delta\mathcal{R} = \sqrt{\Delta\phi^2 + \Delta\eta^2}$ is the angular separation between tracks. This requirement mimics the jet algorithm which clusters calorimeter energy deposits into cones of size $\Delta\mathcal{R} \leq 0.5$. Figure 3.1(b) shows the difference $\eta_b(\text{generated}) - \eta_B(\text{reconstructed})$, which has an RMS width of 0.11. After the cut which removes candidates with $|\eta_B| < 0.1$,

more than 99.9% of reconstructed $B^{\pm}$ mesons have a $q_{\rm FB}$ value which matches the parent quark. This indicates that the $B^{\pm}$ mesons have very similar kinematics to the quarks, making $A_{\rm FB}(B^{\pm})$ a good estimate of $A_{\rm FB}^{b\bar{b}}$.

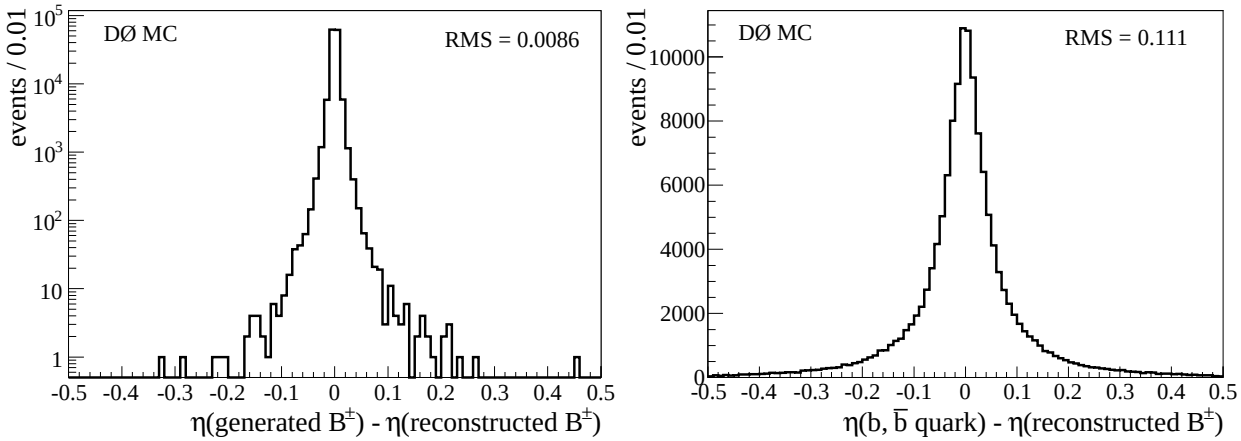

(a) (b)

Figure 3.1 : Distributions of (a) η(generated $B^{\pm}$) $-$ η(reconstructed $B^{\pm}$) and (b) $\eta(b, \bar{b}$ quark) $-$ η(reconstructed $B^{\pm}$) in MC@NLO. Events with $|\eta_{B^{\pm}}| < 0.1$ are rejected.

3.2 Maximum Likelihood Fit

A maximum likelihood fit incorporating a signal probability density distribution and three background distributions is used to extract $A_{\rm FB}(B^{\pm})$. The distributions are functions of the reconstructed $B^{\pm}$ mass $M_{J/\psi K}$ and the kaon energy E_K.

3.2.1 Signal and background distributions

The signal distribution $S(M_{J/\psi K}, E_K)$ is modeled by a double Gaussian function where both Gaussians have the same mean value (m_B) but different widths (σ_1, σ_2):

$$S(M_{J/\psi K}, E_K) = \frac{1-f}{\sigma_1\sqrt{2\pi}} \exp\left(\frac{-(M_{J/\psi K} - m_B)^2}{2\sigma_1^2}\right) + \frac{f}{\sigma_2\sqrt{2\pi}} \exp\left(\frac{-(M_{J/\psi K} - m_B)^2}{2\sigma_2^2}\right). \tag{3.3}$$

The widths of the double Gaussian depend on E_K:

$$\sigma_1 = c_0(1 + c_1 e^{-c_2 E_K}), \tag{3.4}$$

$$\sigma_2 = c_3\sigma_1. \tag{3.5}$$

The formula in equation 3.4 was determined empirically by performing fits in several bins of E_K, with all dependences on E_K removed from the distributions (e.g., setting c_1 to zero). Figure 3.2(a) shows fitted values of c_0 in each bin of E_K with the best fit exponential curve. The final result from the unbinned maximum likelihood fit is drawn for comparison.

We have observed differences between $\eta < 0$ (the "north" side of the detector) and $\eta > 0$ (the "south" side) in the invariant mass distributions of several particles, as shown in Fig. 3.3. The shifts are statistically significant but very small compared to the overall width of the distribution. The magnetic field of the DØ solenoid is not symmetric along the beam direction, but the reconstruction code uses a simplified symmetric field map to improve computation speed. This results in small differences in reconstructed invariant masses on the north and south sides. To allow for these differences a unique set of parameters (m_B, f, $c_0 - c_3$) is used on each side, labeled with a superscript, such as m_B^N or m_B^S. The likelihood

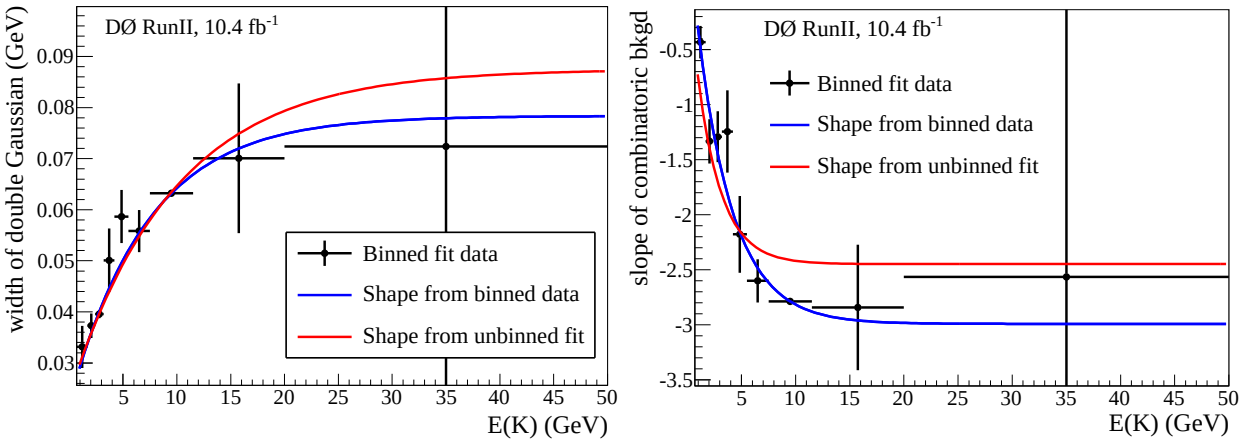

(a) (b)

Figure 3.2 : Formulas for (a) the width σ_1 of the signal distribution and (b) the slope S of the combinatorial background were derived by fitting the data in bins of E_K. The shapes from the unbinned fit (parameters in Table 5.1) have been overlaid for comparison.

function for any given $B^{\pm}$ candidate includes only one set of signal parameters, depending on the pseudorapidity of the $B^{\pm}$ meson. These mass shifts are not taken into account when correcting the J/ψ invariant mass to the world average in the $B^{\pm}$ mass calculation, but adjusting the reconstruction code to include this results in only negligible change to $A_{\rm FB}(B^{\pm})$.

The background distribution $P(M_{J/\psi K}, E_K)$ describes $B^{\pm} \to J/\psi\pi^{\pm}$ events in which the pion is misidentified as a kaon, resulting in an artificially high reconstructed $B^{\pm}$ mass. The distribution P is a reflection of S with the mean value shifted to account for the K/π mass difference and the widths scaled by a ratio of the mean values. The mean value of P is

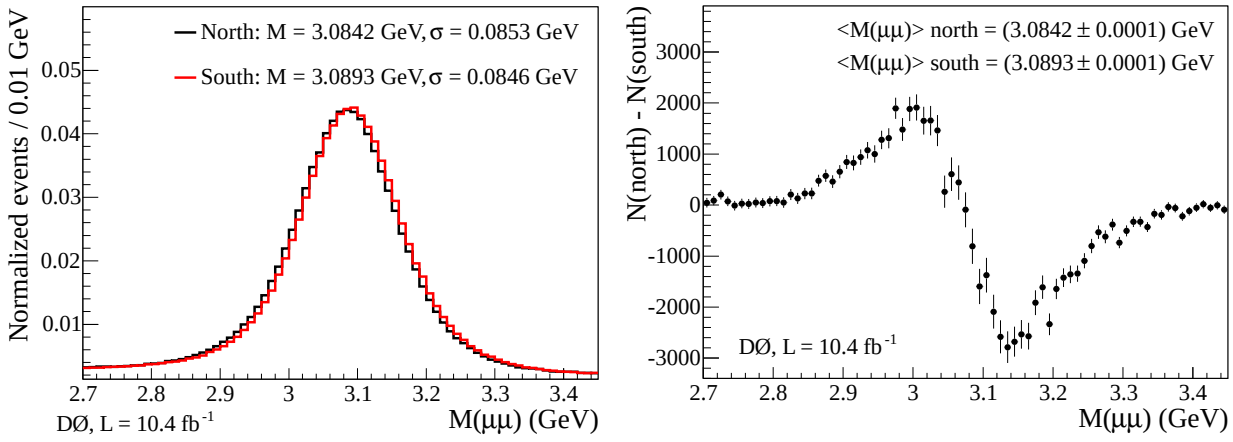

(a) (b)

Figure 3.3 : Demonstration in M(J/ψ) of particle mass differences between the north and south sides: (a) north and south overlaid, and (b) north − south.

denoted $m_{B\pi}$ and is calculated for each candidate according to [34]:

$$m_{B\pi}^2 - m_B^2 = 2E_{J/\psi}(E_K - E_\pi) + m_K^2 - m_\pi^2, \tag{3.6}$$

$$E_{K,\pi} = \sqrt{m_{K,\pi}^2 + |\vec{\mathbf{p}}_K|^2}, \tag{3.7}$$

where m_B is the fitted mean value of the signal distribution, $E_{J/\psi}$ is calculated using the reconstructed mass and momentum of the dimuon pair, $|\vec{\mathbf{p}}_K|$ is the reconstructed momentum of the kaon, $m_K = 0.494$ GeV/c^2, and $m_\pi = 0.140$ GeV/c^2. The widths of P are:

$$\sigma_{1\pi} = \frac{m_{B\pi}}{m_B}\sigma_1, \tag{3.8}$$

$$\sigma_{2\pi} = \frac{m_{B\pi}}{m_B}\sigma_2. \tag{3.9}$$

With this construction, P does not introduce any floating parameters into the fit. The full

functional form is:

$$P(M_{J/\psi K}, E_K) = \frac{1-f}{\sigma_{1\pi}\sqrt{2\pi}} \exp\left(\frac{-(M_{J/\psi K} - m_{B\pi})^2}{2\sigma_{1\pi}^2}\right) + \frac{f}{\sigma_{2\pi}\sqrt{2\pi}} \exp\left(\frac{-(M_{J/\psi K} - m_{B\pi})^2}{2\sigma_{2\pi}^2}\right). \tag{3.10}$$

The background distribution $T(M_{J/\psi K})$ describes all partially reconstructed B mesons. If a B meson decays to a final state with four or more particles, the reconstructed candidate will be missing a portion of its mass. These decays are modeled using a hyperbolic tangent threshold function with the slope parameter fixed from MC simulations [35] and a floating inflection point t:

$$T(M_{J/\psi K}) = \frac{1 - \tanh[25(M_{J/\psi K} - t)]}{T_{\text{norm}}}, \tag{3.11}$$

where T_{norm} is the integral of the numerator over the mass range 5.05 – 5.65 GeV/c^2:

$$T_{\text{norm}} = 0.6 + \frac{1}{25} \ln\left(\frac{\cosh[25(t-5.05)]}{\cosh[25(t-5.65)]}\right). \tag{3.12}$$

Finally, the background distribution $E(M_{J/\psi K}, E_K)$ describes the combinatoric background. It is modeled using an exponential function, with a slope which depends on E_K (Fig. 3.2(b)):

$$E(M_{J/\psi K}, E_K) = \frac{e^{S(M_{J/\psi K} - 5.05)}}{E_{\text{norm}}}, \tag{3.13}$$

$$S = s_0(1 + s_1 e^{-s_2 E_K}), \tag{3.14}$$

where E_{norm} is the integral of the numerator over the mass range 5.05 – 5.65 GeV/c^2:

$$E_{\text{norm}} = \frac{e^{0.6S} - 1}{S}. \tag{3.15}$$

The value of S in E and E_{norm} is calculated for each $B^{\pm}$ candidate using the specific value of E_K.

3.2.2 Likelihood function

Fits are performed using the ROOT `TMinuit` package [36], which varies parameters according to the MIGRAD algorithm to find the minimum value of a test statistic. In practice, our maximum likelihood fit is a minimum negative-log-likelihood fit, where the test statistic is called LLH. This quantity is the negative log of a likelihood function $\mathcal{L}_n$ summed over N selected $B^{\pm}$ candidates, each with weight w_n (sec. 4):

$$\mathrm{LLH} = -2\sum_{n=1}^{N} w_n \ln(\mathcal{L}_n). \tag{3.16}$$

The function $\mathcal{L}_n$ depends on the four probability density functions S, P, T, and E. They are each assigned a sample fraction f_i and a forward-backward asymmetry A_i. Until the analysis method was finalized and systematic effects were studied, the parameters A_i were blinded by adding to them unknown random offsets. $\mathcal{L}_n$ has 26 parameters and is normalized to 1:

$$\begin{aligned}\mathcal{L}_n = \alpha\Big[&f_S(1+q_{\mathrm{FB}}A_S)S(M_{J/\psi K},E_K) + f_P(1+q_{\mathrm{FB}}A_P)P(M_{J/\psi K},E_K)\\ &+ f_T(1+q_{\mathrm{FB}}A_T)T(M_{J/\psi K})\Big] + [1-\alpha(f_S+f_P+f_T)](1+q_{\mathrm{FB}}A_E)E(M_{J/\psi K},E_K),\end{aligned} \tag{3.17}$$

where α describes the dependence of the sample fractions on E_K. The form of α follows that used in previous analyses [37, 34]:

$$\alpha = \begin{cases} 1 + p_0(E_K-3)/3 + p_1(E_K-3)^2/9 & E_K < 3\,\mathrm{GeV} \\ 1 + p_2(E_K-3)/7 & 3\,\mathrm{GeV} \geq E_K < 10\,\mathrm{GeV} \\ 1 + p_2 & E_K \geq 10\,\mathrm{GeV}. \end{cases} \tag{3.18}$$

3.3 Boosted Decision Tree

To improve separation of signal from background we use a Boosted Decision Tree (BDT) multivariate technique [38]. A BDT is trained by comparing distributions of given input variables in signal and background samples. It makes a chain (or "tree") of decisions using all the input variables to determine to what extent a given candidate is signal-like or background-like. After training, candidates in the analysis data sample are processed by the BDT, which returns a discriminant ranging from negative (background-like) to positive (signal-like) values.

We train two BDTs, one for Run IIa and another for Run IIb. The signal sample is a leading-order signal MC simulation in the analysis mass range of 5.05 – 5.65 GeV/c^2. The background sample is data from sidebands above and below the analysis mass range, 4.0 – 5.05 GeV/c^2 and 5.65 – 7.0 GeV/c^2.

3.3.1 Monte Carlo Selection and Reweighting

Leading order $B^{\pm} \to J/\psi K^{\pm}$ MC is generated using PYTHIA [39] with setting msel = 1, which includes both direct $b\bar{b}$ production and gluon splitting into $b\bar{b}$ pairs. The MC is processed using the same reconstruction code as for data, adding MC particle identification information (an integer value number assigned to each type of particle [3]) so that reconstructed μ and $K^{\pm}$ tracks can be matched to tracks from true $B^{\pm} \to J/\psi K^{\pm}$ decays. The MC sample initially contains 219705 Run IIa events and 239395 Run IIb3 events, which is the DØ standard for simulating all of Run IIb data. After the selection cuts we retain 37561 Run IIa events (17%

efficiency) and 35726 Run IIb events (15% efficiency).

MC events which are used to train a BDT should reflect the signal in data as accurately as possible. To create a data sample of estimated signal events within the analysis range of 5.05 – 5.65 GeV we must remove the background contribution beneath the $B^{\pm} \to J/\psi K^{\pm}$ peak. We choose two sideband sub-ranges above and below the peak which contain approximately the same number of $B^{\pm}$ candidates as there are background candidates under the peak. Distributions of BDT input variables (e.g., muon p_T) created from sideband events are then subtracted from distributions created from peak events, leaving distributions which model the estimated signal contribution in the data. Figure 3.4 shows the ranges chosen for peak and sidebands, as well as the signal and background fits (these initial fits had no asymmetry parameters). In the peak range, the background curves have an integral of 12683 $B^{\pm}$ candidates, and there are 12653 candidates in the two sideband ranges.

The MC events are weighted to correct for trigger turn-on effects in the transverse momentum of both muons. We label the muon with larger momentum μ_1 and the muon with smaller momentum μ_2. A weight is also applied to the transverse decay length significance $\mathcal{S}_{xy}(B^{\pm})$. These weights were developed by Masato Aoki [35] in an earlier analysis using this decay channel. The functions are shown below, with coefficients given in Table 3.1:

$$w_{\mu_1} = \frac{m_0}{1.43}\left[\mathrm{erf}(m_1[p_T(\mu_1) - m_2]) + m_3\right], \tag{3.19}$$

$$w_{\mu_2} = \frac{m_4}{2}\left[\mathrm{erf}(m_5[p_T(\mu_2) - m_6]) + m_7\right], \tag{3.20}$$

$$w_{\mathcal{S}_{xy}} = m_8 \exp[-m_9 \mathcal{S}_{xy}(B^{\pm})]. \tag{3.21}$$

To improve the effects of these weights on our specific samples, we test agreement be-

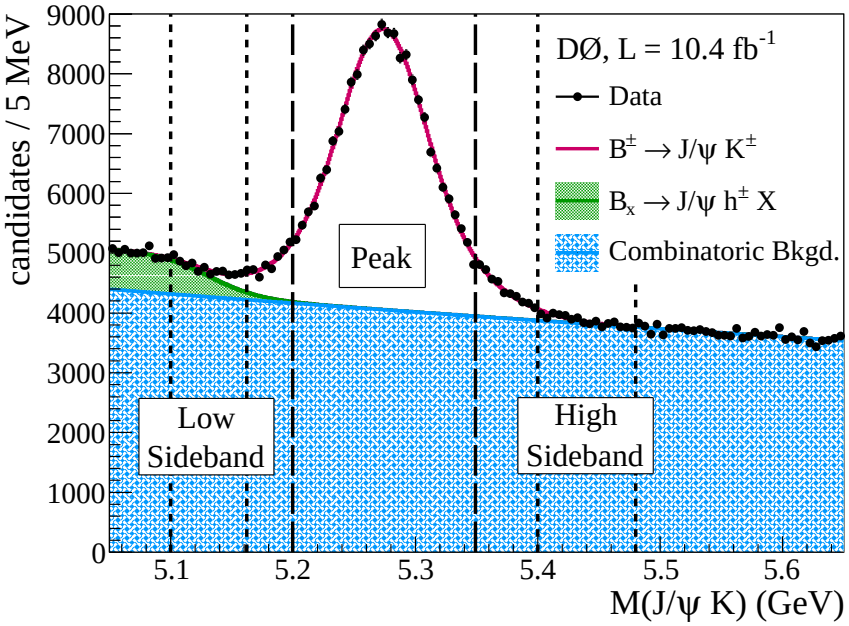

Figure 3.4 : Analysis range data showing the choice of peak sub-range and 2 sideband sub-ranges. The fitted curves are used to calculate the expected number of background candidates under the signal peak.

Table 3.1 : MC muon trigger weight coefficients

	w_{μ_1} (Eq. 3.19)				w_{μ_2} (Eq. 3.20)				$w_{\mathcal{S}_{xy}}$ (Eq. 3.21)	
Run Period	m_0	m_1	m_2	m_3	m_4	m_5	m_6	m_7	m_8	m_9
Run IIa	0.674	0.723	3.638	1.056	0.474	1.6	2.5	3.09	1.189	0.00896
Run IIb	0.693	1.38	3.591	1.054	0.373	1.29	2.78	4.18	1.306	0.01081

tween distributions of sideband subtracted data and signal MC in all the BDT variables. Additional weights are derived for several key variables to match the distributions in MC to the distributions in data: $p_T(\mu_1)$, $p_T(B^{\pm})$, $p_T(K^{\pm})$, and χ^2 of the $B^{\pm}$ vertex fit. We also apply a weight to the highest bin of two "isolation" variables, where isolation is defined as a particle's momentum divided by the sum of the particle's momentum plus the momentum of all other tracks in a cone of size $\Delta\mathcal{R} < 1$. Isolation is calculated for the $B^{\pm}$ candidate as well as the two muons:

$$\mathcal{I}(B^{\pm}, \mu) = \frac{p(B^{\pm}, \mu)}{p(B^{\pm}, \mu) + \sum\limits_{\Delta\mathcal{R}=1} p(track)}. \tag{3.22}$$

If there are no other tracks within the given cone, $\mathcal{I} = 1$. The MC does not model the fraction of completely isolated particles well, so events in those bins are reweighted using a discrete value.

The weighting functions are created in sequence after the previous weight has been applied, resulting in a combination of weights which produce good data/MC agreement in all BDT variables. The $p_T(B^{\pm})$ distribution (Fig. 3.6) has an unusual shape at low p_T caused by the sideband subtraction procedure. This distribution is only reweighted above 5 GeV/c and is replaced with $p(B^{\pm})$ in the BDT. Figures 3.5 – 3.10 compare sideband subtracted data to signal MC before and after the application of weights.

3.3.2 BDT training and cut selection

To choose BDT input variables, reweighted signal MC is contrasted with data in the background sidebands to determine if a variable has meaningful separation between signal and

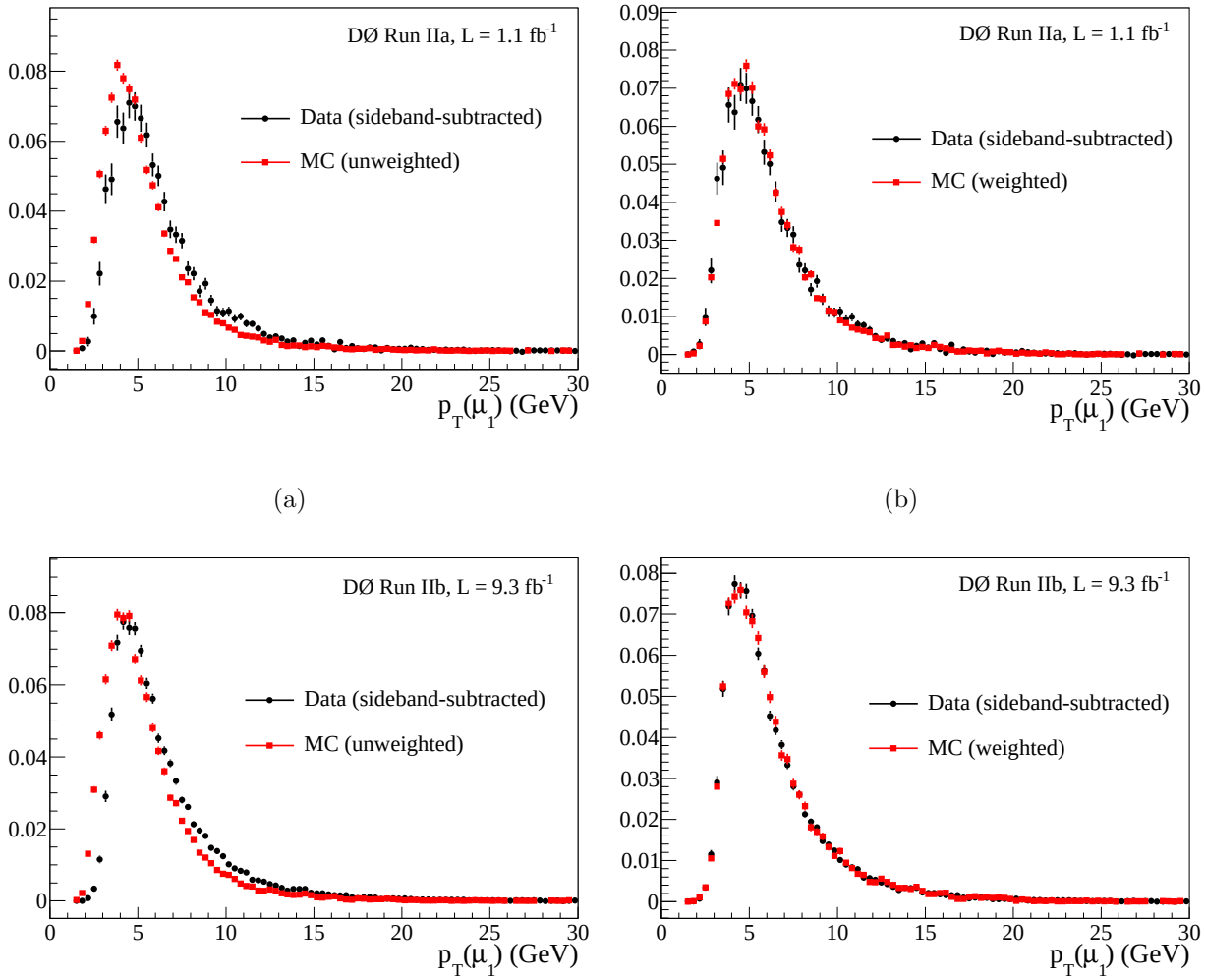

Figure 3.5 : Distributions of $p_T(\mu_1)$ in data (black) and MC (red) for Run IIa (a) before and (b) after reweighting, and Run IIb (c) before and (d) after reweighting.

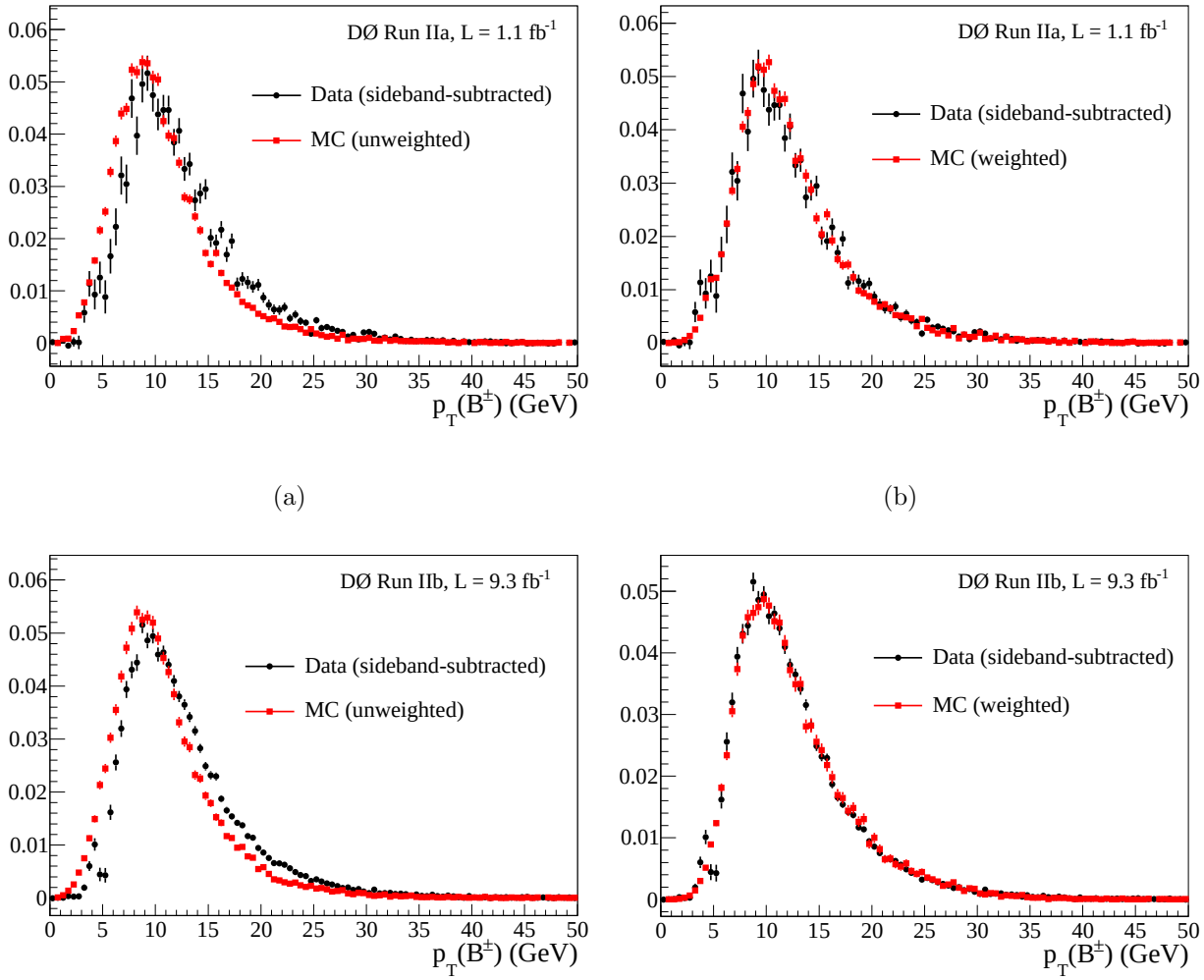

Figure 3.6 : Distributions of $p_T(B^{\pm})$ in data (black) and MC (red) for Run IIa (a) before and (b) after reweighting, and Run IIb (c) before and (d) after reweighting.

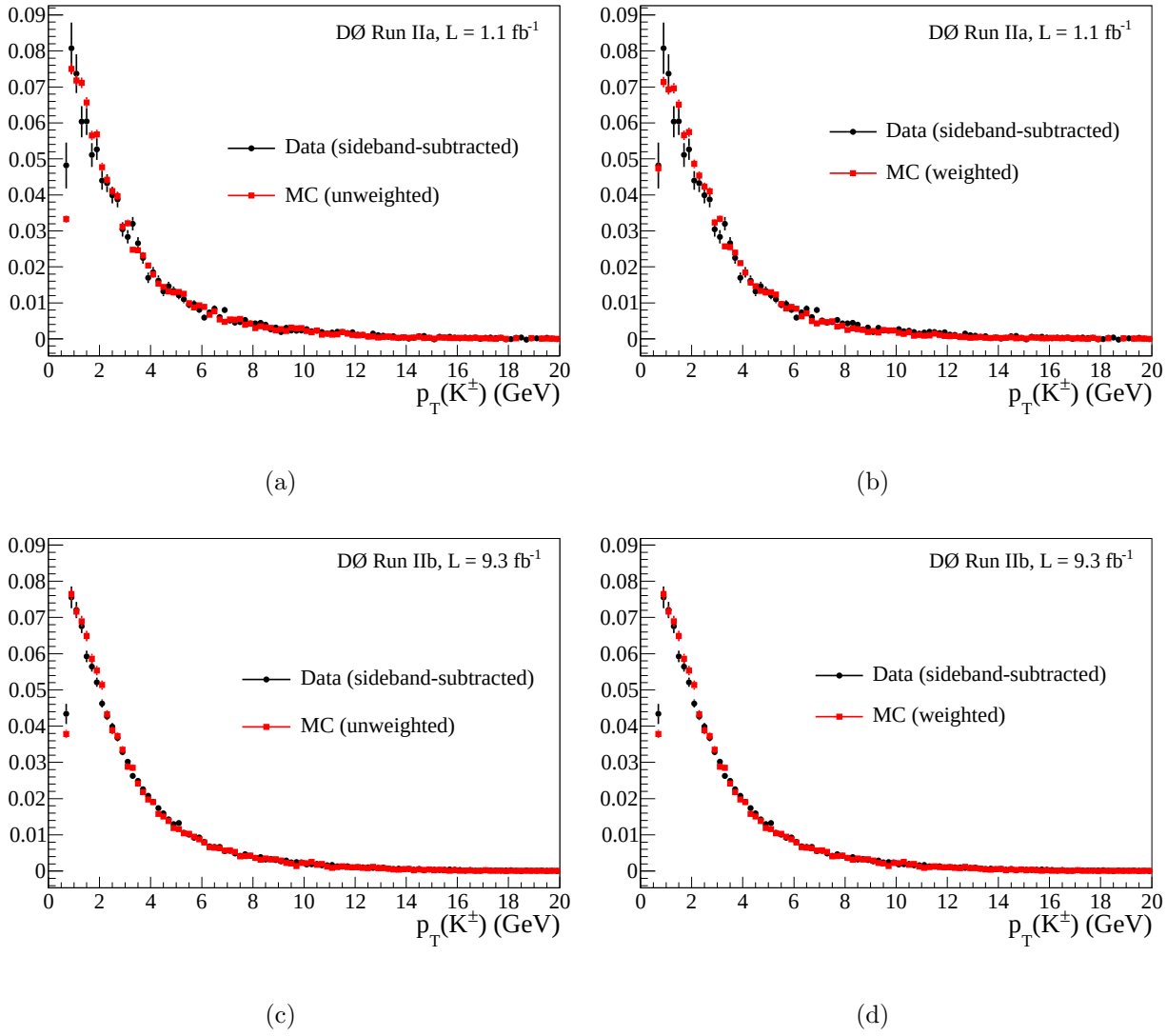

Figure 3.7 : Distributions of $p_T(K^{\pm})$ in data (black) and MC (red) for Run IIa (a) before and (b) after reweighting, and Run IIb (c) before and (d) after reweighting.

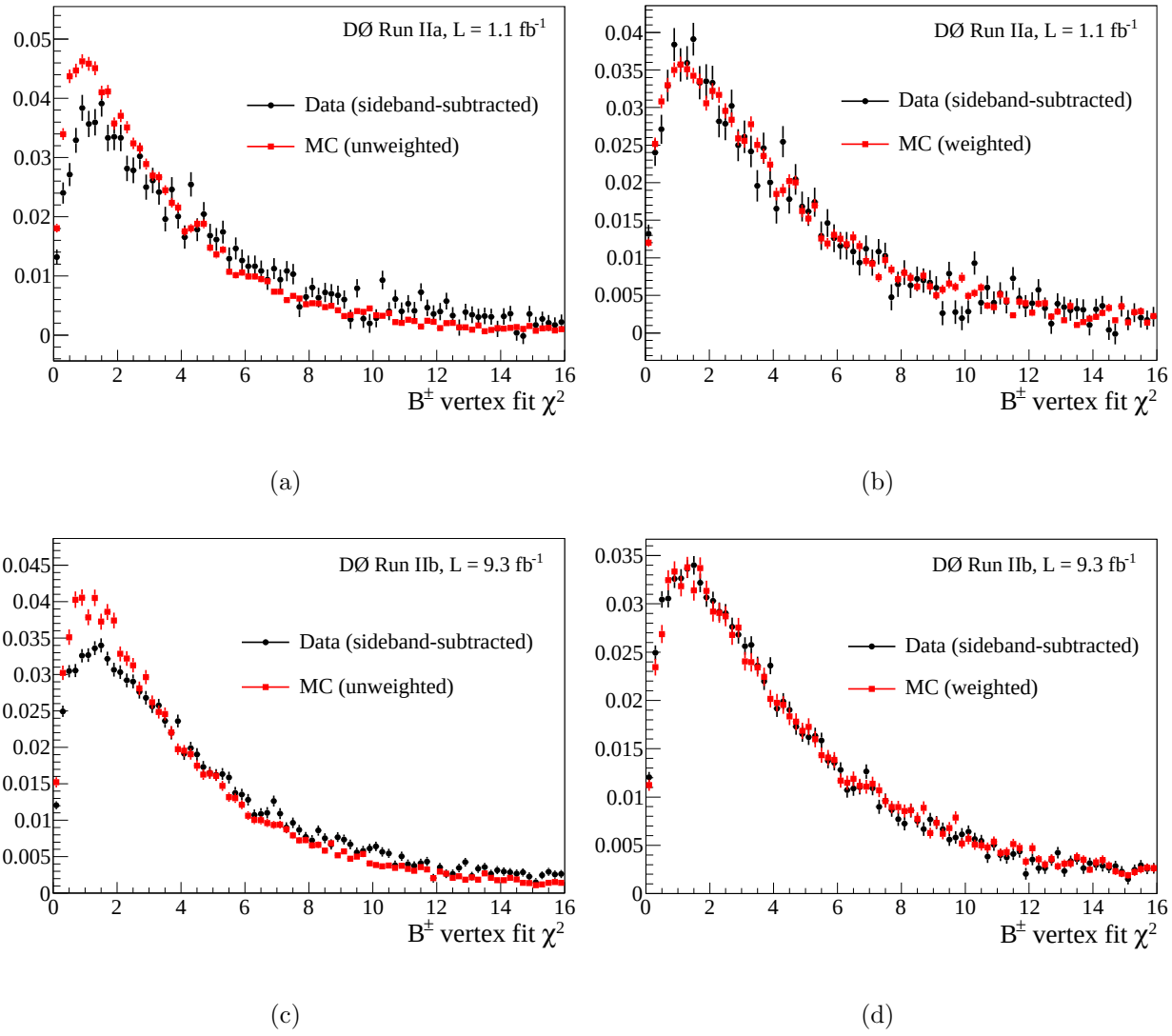

Figure 3.8 : Distributions of $B^{\pm}$ vertex χ^2 in data (black) and MC (red) for Run IIa (a) before and (b) after reweighting, and Run IIb (c) before and (d) after reweighting.

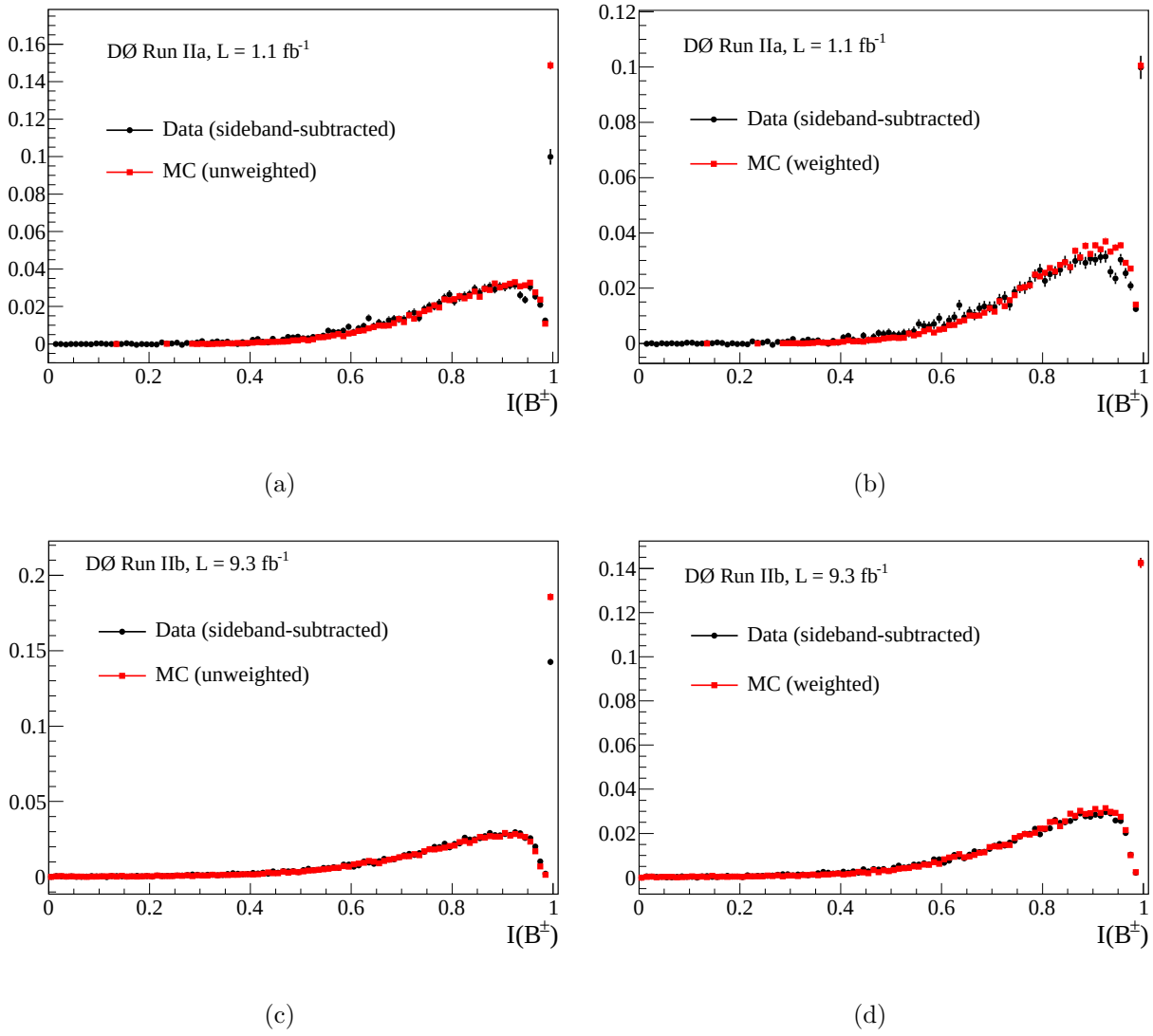

Figure 3.9 : Distributions of $\mathcal{I}(B^{\pm})$ in data (black) and MC (red) for Run IIa (a) before and (b) after reweighting, and Run IIb (c) before and (d) after reweighting.

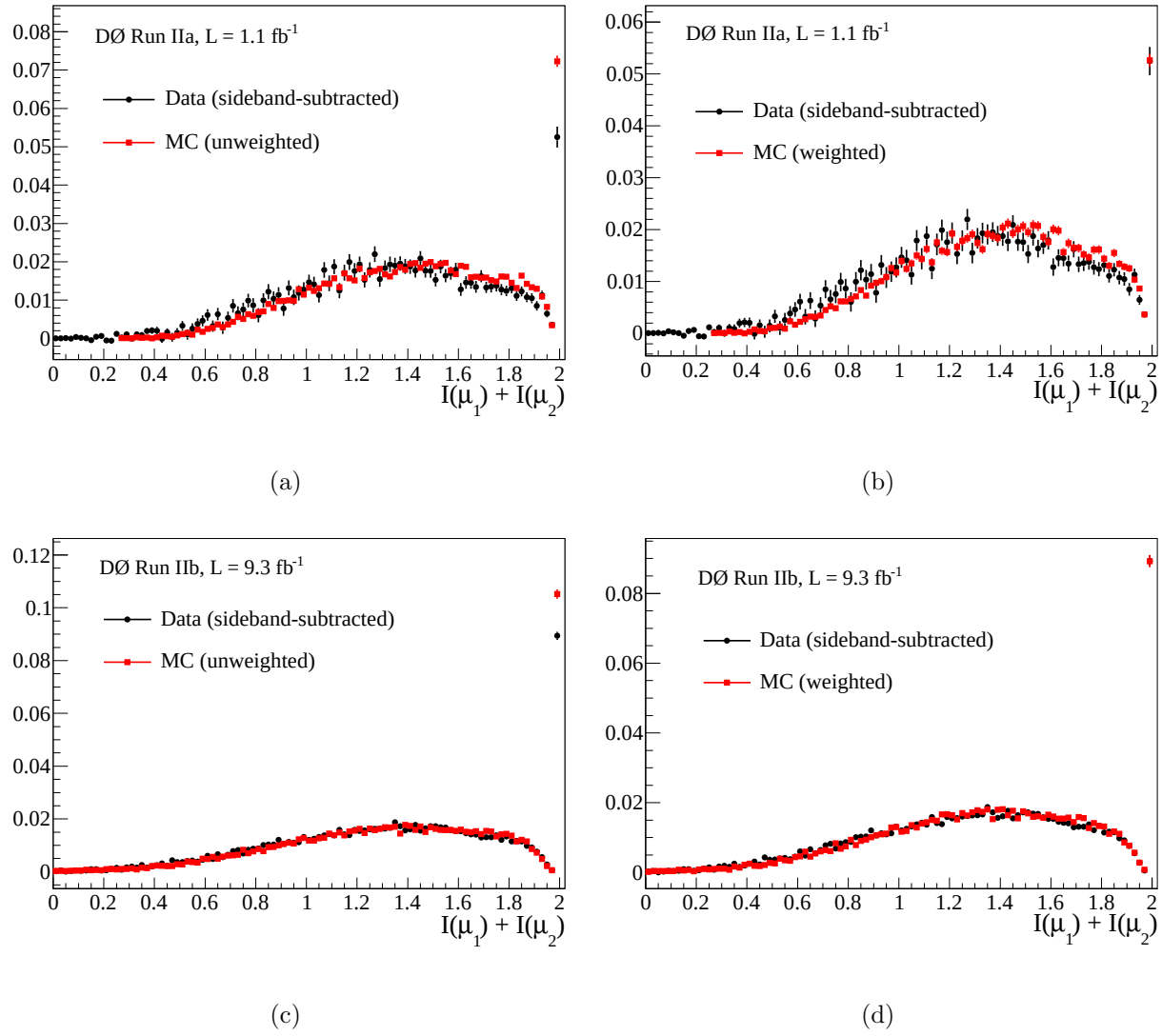

Figure 3.10 : Distributions of $\mathcal{I}(\mu_1) + \mathcal{I}(\mu_2)$ in data (black) and MC (red) for Run IIa (a) before and (b) after reweighting, and Run IIb (c) before and (d) after reweighting.

background. Comparisons of sideband-subtracted data, MC signal, and background data for all input variables are shown in Appendix A. For Run IIb the BDT uses 35726 signal MC events and 2764049 background events. For Run IIa the BDT uses 37561 signal events and 534764 background events. In both run periods, 850 boosted decision trees are trained using 12000 of the signal MC events and 12000 of the background events. The performance of the BDT is then tested on the remaining events. Figure 3.11 compares BDT values in the training and testing samples for both run periods. Variables were added or removed from the Run IIb BDT until the best performance was achieved. Figure 3.12 demonstrates the performance of the BDT, comparing the percentage of background events rejected to the percentage of signal events retained. After optimization the BDT for Run IIa is trained using the same set of variables. The final BDT contains 40 input variables, the first 10 of which are listed in Table 3.2 in order of their importance.

To choose a cut on the BDT discriminant, a sequence of 50 fits is performed using different cuts. Each fit used a unique random number to blind q_{FB} in the data, and the set of 50 fits was duplicated five times. Figure 3.13(a) shows the statistical uncertainty on the signal asymmetry, A_S, at different BDT cuts. To minimize the statistical uncertainty we accept events with BDT > -0.01 into the final data sample. This cut gives an expected uncertainty on A_S of approximately 0.41% and also a high fraction of signal events in the final sample (Fig. 3.13(b)).

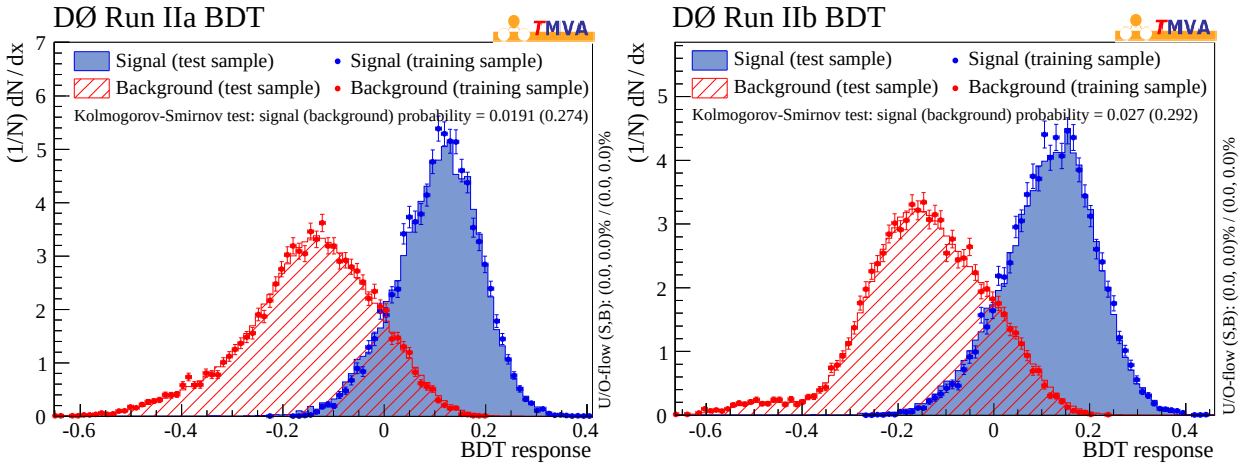

(a) (b)

Figure 3.11 : Distributions of BDT values in the signal and background samples for (a) Run IIa and (b) Run IIb. The training samples (points) match the testing samples (histograms) well.

3.3.3 Fit validation

To validate the statistical uncertainty returned by the fit we use an ensemble test of 1000 trials, where the values of $q_{\rm FB}$ are randomized, with a unique random number generator seed for each trial. Figure 3.14 show the values of $A_{\rm FB}(B^{\pm})$ measured in each trial. The Gaussian distributions is centered at $A_{\rm FB}(B^{\pm}) = 0$, as expected for randomized data, and the width of (0.40 ± 0.01) is consistent with the statistical uncertainty of 0.41% from the fit.

The fit method was tested for bias by injecting a series of 100 test asymmetries into the blinded data. At each test point the values of $q_{\rm FB}$ were assigned randomly, and then $q_{\rm FB}$ was flipped in a percentage of randomly chosen events to generate an asymmetry. The test was repeated five times and the results combined. Figure 3.15 shows that the fit succeeds

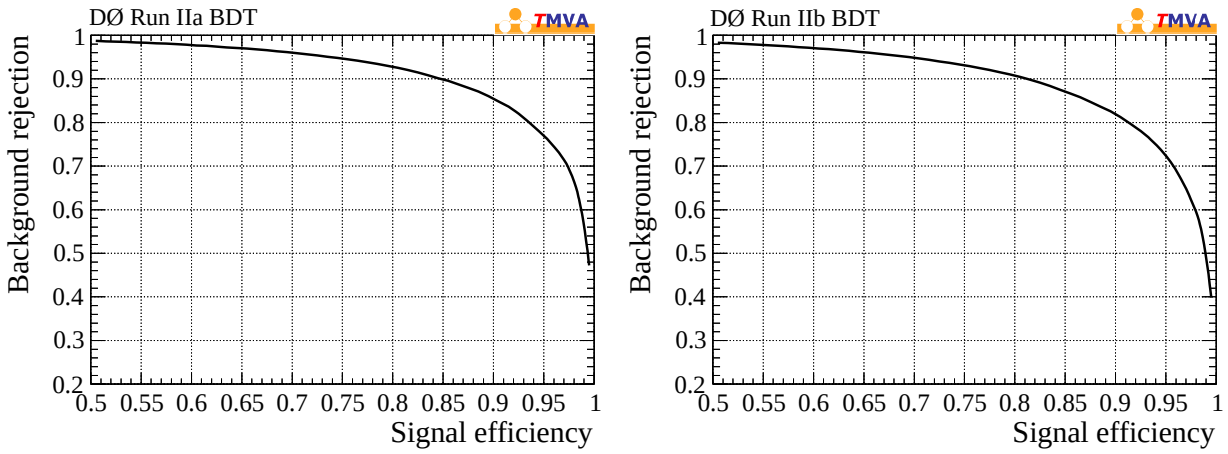

(a) (b)

Figure 3.12 : Comparisons of background rejection versus signal efficiency in BDTs for (a) Run IIa and (b) Run IIb. The optimal BDT has the highest percentage of background rejection for a given value of signal efficiency.

in returning the input asymmetry values. The adjustments to A_{FB} given by this calibration line are added as a systematic uncertainty since they are consistent with zero.

Table 3.2 : Run IIb boosted decision tree variables. Impact parameter denotes a particle's distance of closest approach to the $p\bar{p}$ vertex, in the x-y plane (transverse) or along z (longitudinal). Impact parameter significance is the value divided by its uncertainty.

Rank	Variable	Fraction of Decisions
1	$B^{\pm}$ transverse impact parameter (IP)	0.2404
2	$B^{\pm}$ transverse IP significance	0.2347
3	J/ψ transverse IP significance	0.0956
4	$p_T(K^{\pm})$	0.0364
5	$\phi_{K^{\pm}} - \phi_{J/\psi}$	0.0352
6	$\phi_{B^{\pm}} - \phi_{K^{\pm}}$	0.0307
7	$\eta_{\mu_1} - \eta_{\mu_2}$	0.0305
8	$L_{xy}(B^{\pm})$	0.0291
9	$\mathcal{S}_{xy}(B^{\pm})$	0.0286
10	$K^{\pm}$ longitudinal IP	0.0252

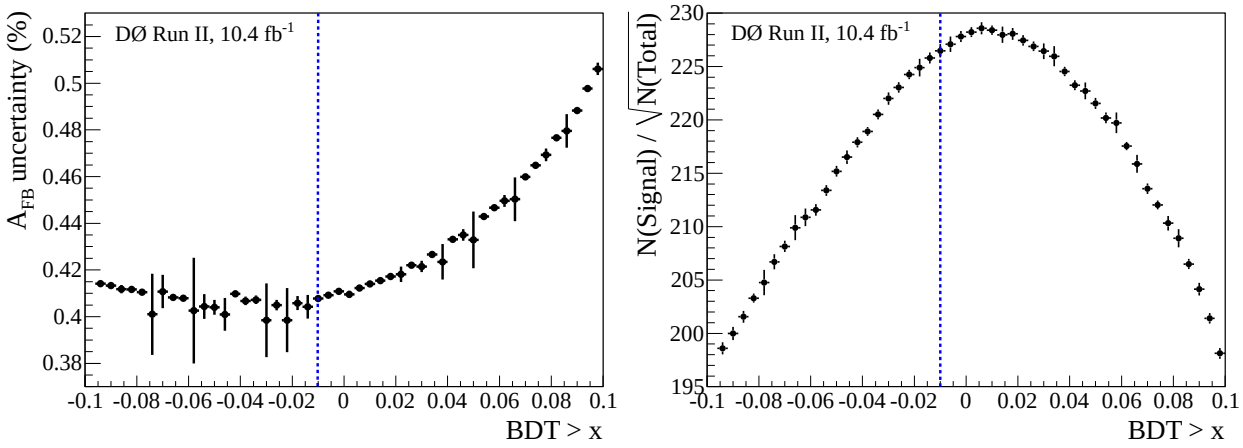

(a) (b)

Figure 3.13 : The BDT minimum value of -0.01 was chosen to balance (a) a small uncertainty on the signal asymmetry with (b) a large fraction of signal events in the sample.

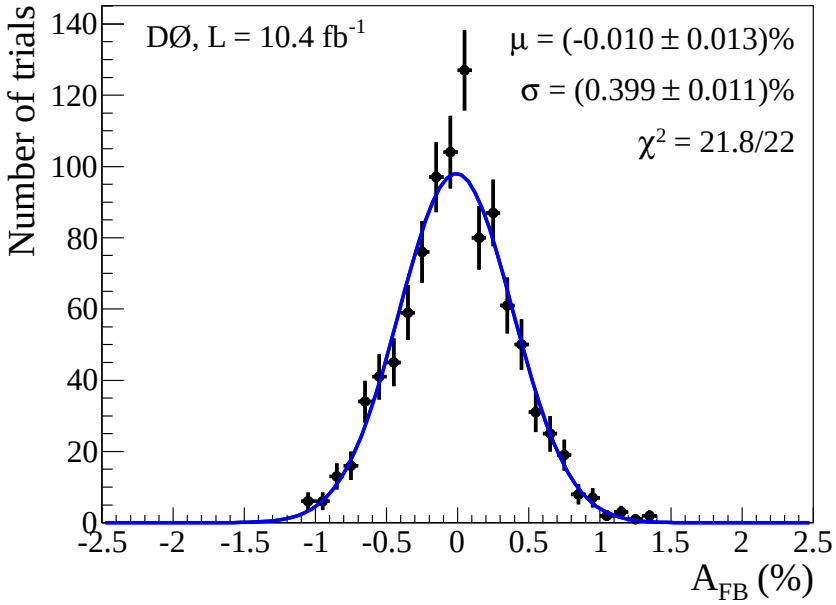

Figure 3.14 : Values of $A_{\rm FB}(B^{\pm})$ from an ensemble test of 1000 fits to data with $q_{\rm FB}$ randomized. The mean value is zero, as expected, and the width of (0.40±0.01)% is consistent with the statistical uncertainty of 0.41% returned by the fit.

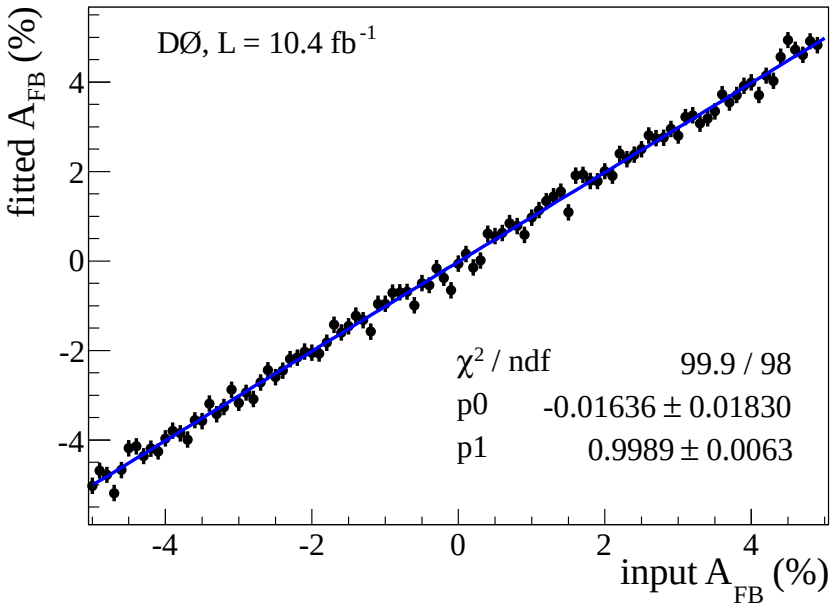

Figure 3.15 : Fitted values of A_{FB} versus the injected values, in data with q_{FB} randomized. The data points combine five sets of fits with unique random seeds for each input asymmetry. The best fit line has an offset consistent with zero and a slope consistent with one, which shows the fit measures the expected asymmetries.

Chapter 4

Removing Detector Asymmetries

There are no production asymmetries that we expect as backgrounds to $A_{\rm FB}(B^{\pm})$, but asymmetries in detector material and J/ψ or $K^{\pm}$ reconstruction can result in an apparent $A_{\rm FB}$. A forward-backward asymmetry is, in essence, a combination of an asymmetry between the numbers of positive and negative particles and an asymmetry between the numbers of particles on the north side ($\eta < 0$) and the south side ($\eta > 0$) of the detector. The reconstruction of $B^{\pm} \to J/\psi K^{\pm}$ decays must not introduce either form of asymmetry, which would bias the measurement of the production asymmetry.

4.1 Magnet polarity weights

To remove charge asymmetries, $A = (N^+ - N^-)/(N^+ + N^-)$, from the tracking detectors we use a weight to equalize the number of $B^{\pm}$ candidates in each of four magnet polarity settings. In one polarity a B^+ is reconstructed with the same sign of curvature as a B^- in the opposite polarity, so with this weighting any detector inefficiencies will affect both charges equally. We also equalize the number of B^+ and B^- candidates in the final data sample, which eliminates the need to correct for different K^+ and K^- interaction cross sections in the detector [40]. Negative kaons contain a strange quark which can interact with detector matter to form hyperons, and positive kaons have no corresponding interaction. This creates

higher tracking efficiency for positive kaons and therefore a charge asymmetry, which is $\approx 1\%$ integrated over $|\eta|$ and p_T.

After removing events with BDT < -0.01, 163765 events remain in the final data sample. We combine the four magnet polarity settings and two $B^{\pm}$ charges into a group of eight (solenoid polarity) $\times$ (toroid polarity) $\times$ ($B^{\pm}$ charge) settings. The weight for setting i is $w_i = N_i/N_{\rm min}$, where $N_{\rm min}$ is the number of candidates in the smallest setting. Because DØ took data with regular magnet polarity reversal, all the weights are larger than 0.96. The polarity-charge weights are shown in Table 4.1.

4.2 J/ψ north-south asymmetry

To account for differences in efficiency between the north and south sides of the detector we measure north-south asymmetries for both decay products in data samples which are not expected to have a production asymmetry. A north-south asymmetry is defined as:

$$A_{\rm NS} = \frac{N_N - N_S}{N_N + N_S}. \tag{4.1}$$

To measure $A_{\rm NS}(J/\psi)$, a sample of prompt $J/\psi \to \mu^+\mu^-$ decays is collected using the selection criteria described in previously (sec. 3.1), adding the requirement that the $\mathcal{S}_{xy}(J/\psi)$ must be less than 1.5. This requirement guards against J/ψ mesons from various types of B decays, which may have a production asymmetry, such as $A_{\rm FB}(B^{\pm})$. We estimate the remaining fraction of non-prompt particles by comparing distributions of J/ψ mesons with positive versus negative decay lengths. Negative decay length is an artifact of Gaussian detector resolution, and indicates particles whose true decay length is very near zero. By

Table 4.1 : Magnet polarity and charge weights

Solenoid Polarity	Toroid Polarity	$B^{\pm}$ Charge	N Events	Weight
-1	-1	-1	20318	0.986564
-1	-1	+1	20795	0.963934
-1	+1	-1	20813	0.963100
-1	+1	+1	20852	0.961299
+1	-1	-1	20045	1.0
+1	-1	+1	20121	0.996223
+1	+1	-1	20403	0.982454
+1	+1	+1	20418	0.981732

mirroring the negative $\mathcal{S}_{xy}$ distribution across $\mathcal{S}_{xy} = 0$ and subtracting it from the positive $\mathcal{S}_{xy}$ distribution we can calculate the fraction of non-prompt particles, which form a tail out to large positive $\mathcal{S}_{xy}$ (shown in Fig. 4.1). For a maximum $\mathcal{S}_{xy}$ of 1.5 we find $\approx 2\%$ non-prompt particles. Calculation of $A_{\rm NS}(J/\psi)$ has been tested at several maximum $\mathcal{S}_{xy}$ values and there is no significant dependence on this cut.

After all selection cuts the J/ψ sample has very little background. Sideband subtraction is used to remove background events under the peak from $2.9 - 3.3$ GeV/c^2. Sideband ranges are set for each bin of $|\eta|$ and are shown in Fig. 4.2. Histograms in bins of J/ψ p_T and $|\eta|$

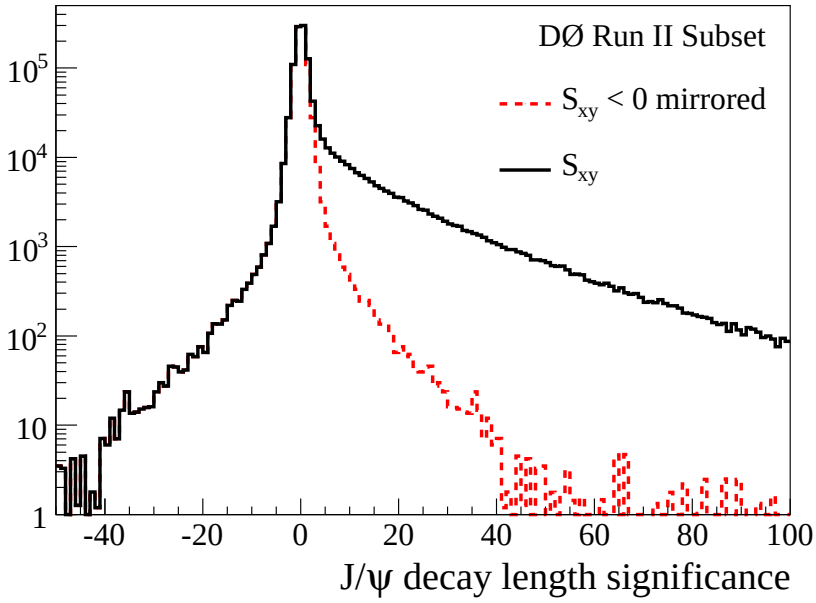

Figure 4.1 : Distribution of $\mathcal{S}_{xy}(J/\psi)$, showing a tail in positive values due to non-prompt J/ψ production. The number of mesons with negative decay length (solid black) can be mirrored onto positive values (dashes) and subtracted from the number of mesons with positive decay length (solid red), allowing calculation of the non-prompt event fraction.

are used to compute the North-South asymmetries as follows:

$$A_{\rm NS} = \frac{N_N(\text{peak}) - N_N(\text{sidebands}) - N_S(\text{peak}) + N_S(\text{sidebands})}{N_N(\text{peak}) - N_N(\text{sidebands}) + N_S(\text{peak}) - N_S(\text{sidebands})}. \tag{4.2}$$

Values of $A_{\rm NS}(J/\psi)$ are shown in Fig. 4.3 and listed in Table 4.2. The large asymmetries seen in the lowest bins of $p_T(J/\psi)$ appear to be caused by differences in detector material. Figure 4.4(a) shows muon placement in bins of $\eta(\mu)$ and $\phi(\mu)$ when $p_T(J/\psi) < 5.5$ GeV and $|\eta(J/\psi)| < 1.2$. There is a distinct difference between the north and south sides, with a deficiency of muons on the north side. Figure 4.4(b) shows the momentum distribution of these muons. Muons on the north side have $\langle p(\mu)\rangle = (4.039 \pm 0.002)$ GeV while muons on the south side have $\langle p(\mu)\rangle = (4.018 \pm 0.002)$ GeV, suggesting that something on the north side of the detector is causing a larger momentum threshold for muon reconstruction. Since muons in this low momentum range are just able to traverse the calorimeter and reach the muon tracking systems, we expect that they are quite sensitive to interactions with inactive detector material (such as cable bundles) which is not placed symmetrically on both sides of the detector. However, the bins of large $A_{\rm NS}(J/\psi)$ are a small fraction of the data sample. Integrated over p_T and $|\eta|$ we measure $A_{\rm NS}(J/\psi) = (-0.41 \pm 0.04)\%$.

4.3 $K^{\pm}$ north-south asymmetry

The $\phi \to K^+K^-$ decay is used to measure $A_{\rm NS}(K^{\pm})$. Events are selected in which two oppositely charged tracks form a vertex with a mass between 0.99 and 1.06 GeV/c^2. The tracks are selected using criteria which mirror the properties of the kaon candidates in the $B^{\pm} \to J/\psi K^{\pm}$ sample. Each track must have 3 hits in the SMT detector, 4 hits in the CFT

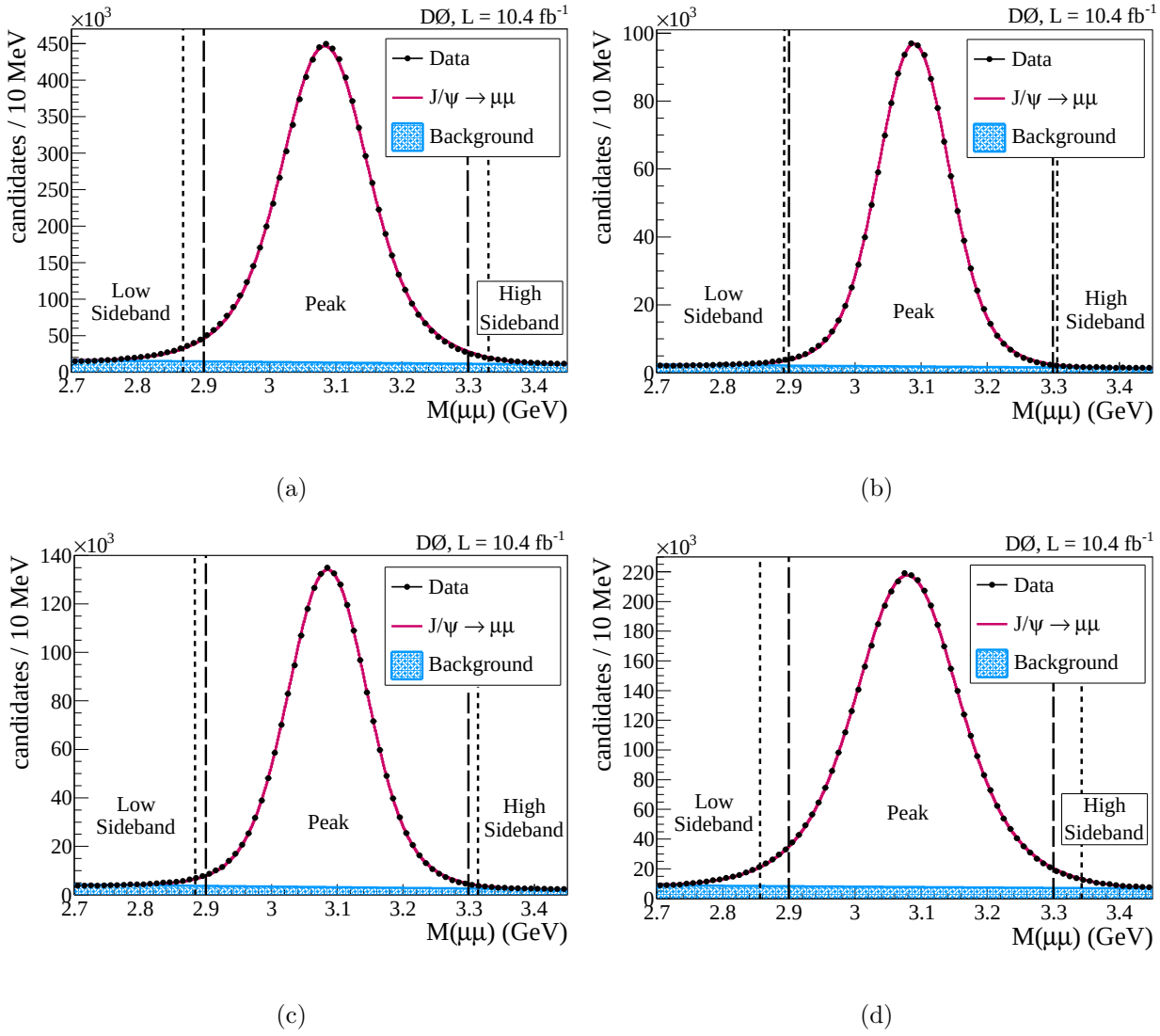

Figure 4.2 : Sideband and peak definitions for $J/\psi \to \mu^+\mu^-$ decays in (a) the whole detector, (b) $|\eta(J/\psi)| \leq 0.7$, (c) $0.7 < |\eta(J/\psi)| \leq 1.2$, and (d) $1.2 < |\eta(J/\psi)| \leq 2.2$.

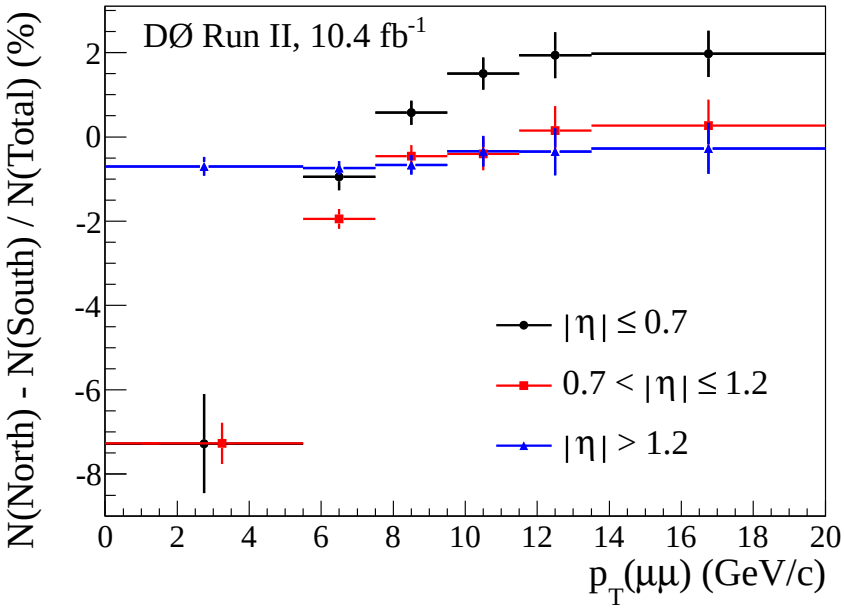

Figure 4.3 : North-south reconstruction asymmetries of prompt J/ψ mesons in bins of $|\eta|$ and p_T.

Table 4.2 : North-south asymmetries $A_{\rm NS}(J/\psi)$ (%).

p_T range (GeV/c)	$\lvert\eta\rvert \leq 0.7$	$0.7 < \lvert\eta\rvert \leq 1.2$	$\lvert\eta\rvert > 1.2$
< 5.5	-6.56 ± 0.58	-8.19 ± 0.23	0.12 ± 0.11
5.5 – 7.5	-1.58 ± 0.16	-2.46 ± 0.12	0.15 ± 0.08
7.5 – 9.5	0.30 ± 0.15	-1.00 ± 0.13	0.25 ± 0.11
9.5 – 11.5	1.37 ± 0.21	0.09 ± 0.20	0.41 ± 0.18
11.5 – 13.5	2.21 ± 0.31	0.60 ± 0.31	0.44 ± 0.28
> 13.5	2.48 ± 0.33	0.34 ± 0.34	0.80 ± 0.31

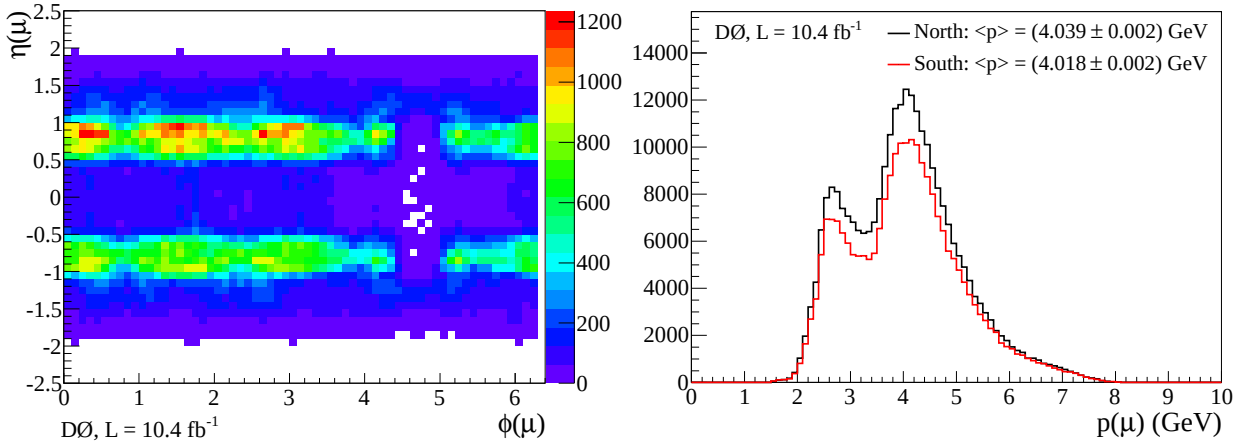

(a) (b)

Figure 4.4 : Distributions of (a) muon placement in η-ϕ bins and (b) muon momentum on the north and south sides when $|\eta(J/\psi)| < 1.2$ and $p_T(J/\psi) < 5.5$ GeV.

detector, and $|\eta| \leq 2.2$. Additional requirements are transverse impact parameter less than 1.0 cm, p_T 0.7 – 13.5 GeV/c, and track fit χ^2 less than 400. The ϕ meson must have vertex fit χ^2 less than 16 for two degrees of freedom and the cosine of the two-dimensional pointing angle must be greater than 0.8. Finally, the kaon tracks must have a minimum separation of $\Delta\mathcal{R} = \sqrt{(\Delta\phi)^2 + (\Delta\eta)^2} > 0.15$ to ensure non-collinear tracks.

The $M(K^+K^-)$ distribution is fitted using a binned χ^2 minimization fit. The signal is modeled by a relativistic Breit-Wigner resonance convoluted with a double Gaussian resolution to represent the detector resolution. The convolution is performed in each bin of $M(K^+K^-)$, with the bin center labeled m_i, by integrating a variable x:

$$P_{\text{signal}} = \int_{m_i-10\sigma_0}^{m_i+10\sigma_0} G_{\text{res}}(m_i - x, \sigma_0, \sigma_1) P_{\text{BW}}(x)\, \mathrm{d}x, \tag{4.3}$$

where $G_{\rm res}$ is a double Gaussian function with six floating parameters and the same structure as the probability distribution $S(M_{J/\psi K}, E_K)$ in Eq. 3.3. The width σ_0 is the larger of the two widths. This double Gaussian resolution form was chosen to improve the fit performance compared to a single Gaussian resolution. The Breit-Wigner probability depends on the floating mass of the resonance M and a mass-dependent width γ:

$$P_{\rm BW}(x) = \frac{2xM\gamma}{\pi[(x^2 - M^2)^2 + M^2\gamma^2]}, \tag{4.4}$$

$$\gamma = \frac{M\Gamma}{x}\left(\frac{|(x^2/4) - M_K^2|}{|(M^2/4) - M_K^2|}\right)^{3/2} B_L'^2. \tag{4.5}$$

Here Γ is the fixed total width of the resonance, M_K is the kaon mass, and $B_L'^2$ is the Blatt-Weisskopf barrier function which accounts for the relationship between angular momentum L ($L = 1$ for the ϕ meson) and linear momentum.

$$B_1'^2 = \frac{1 + |(M^2/4) - M_K^2|/d^2}{1 + |(x^2/4) - M_K^2|/d^2}, \tag{4.6}$$

where $d = 5$ GeV is a fixed meson radius [41].

Two background models were determined from simulation, using a sample of $B_s \to J/\psi\phi$ MC generated using PYTHIA. Random combinations of two tracks and partially reconstructed particles are modeled with an exponential function labeled B_1. Two-body decays which are not identified as $\phi \to K^+K^-$ using the MC particle ID information are modeled with a quadratic function labeled B_2, with the coefficients fixed to the MC values since they are consistent across bins of leading kaon $|\eta|$. Both functions depend on the bin center values

m_i in the $M(K^+K^-)$ distribution:

$$B_1 = N_1(1 - b_0 e^{-b_1 m_i}) \tag{4.7}$$

$$B_2 = N_2(1 - 2.025 m_i + 1.025 m_i^2) \tag{4.8}$$

Data on the north and south sides are fitted simultaneously by minimizing the sum χ^2(north) + χ^2(south). All fit parameters are allowed to have different values on the north and south sides. The signal asymmetry is constructed as a fit parameter so that its uncertainty is calculated with all correlations included. Parameters N (number of $\phi \to K^+K^-$ events) and $A_{\rm NS}$ are related to the counts N(north) and N(south) as follows:

$$N(\text{north}) = N(1 + A_{\rm NS})/2, \tag{4.9}$$

$$N(\text{south}) = N(1 - A_{\rm NS})/2. \tag{4.10}$$

We measure $A_{\rm NS}(K^\pm)$ in bins of leading kaon charge and pseudorapidity. Unlike the north-south asymmetries for the J/ψ, no significant dependence on p_T is seen in the kaon asymmetries, which are listed in Table 4.3. Figure 4.5 shows $A_{\rm NS}(K^\pm)$ in three bins of $|\eta|$, and Figs. 4.6 – 4.8 show the fits for each bin. The large size of this sample makes achieving good fit quality difficult, but the fit performance is the same for data on the north and south sides. Integrated over all $|\eta|$, $A_{\rm NS}(K^+) = (0.39 \pm 0.22)\%$ and $A_{\rm NS}(K^-) = (0.64 \pm 0.23)\%$.

Table 4.3 : North-south asymmetries $A_{\rm NS}(K^{\pm})$.

$\lvert\eta\rvert$ range	$K^{+}A_{\rm NS}(\%)$	$K^{-}A_{\rm NS}(\%)$
$\lvert\eta\rvert \leq 0.7$	0.48 ± 0.26	0.71 ± 0.26
$0.7 < \lvert\eta\rvert \leq 1.2$	0.64 ± 0.25	-0.14 ± 0.24
$1.2 < \lvert\eta\rvert \leq 2.2$	0.13 ± 0.52	1.15 ± 0.54

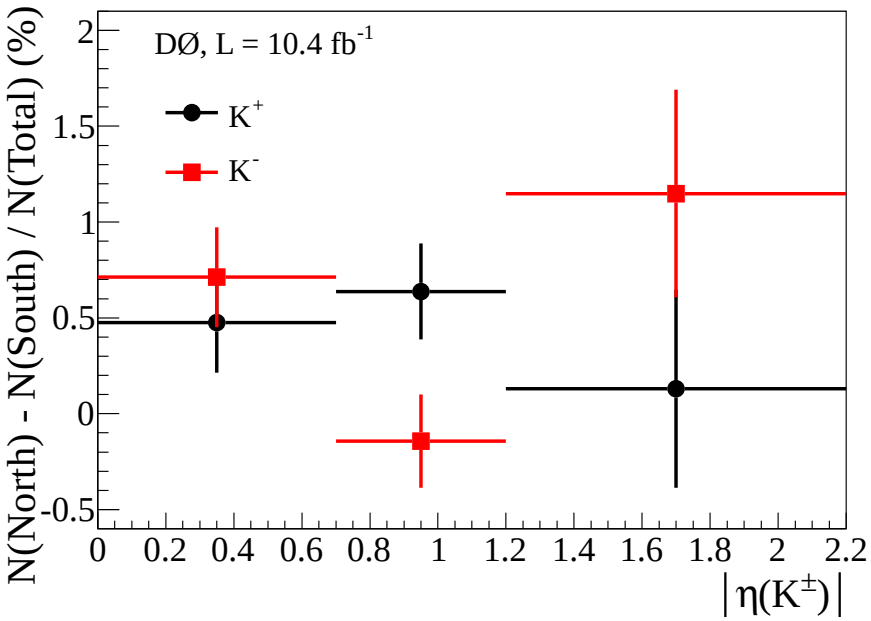

Figure 4.5 : Kaon north-south asymmetries in bins of leading kaon charge and $|\eta|$

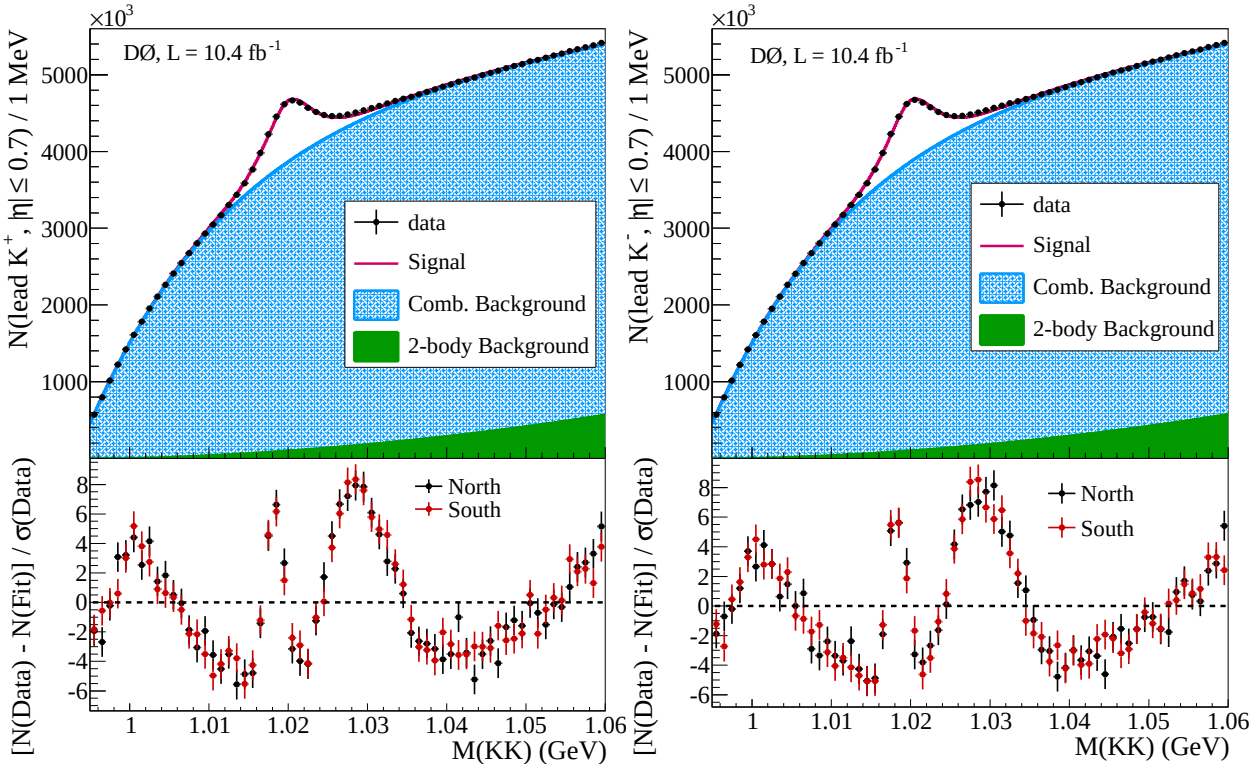

(a) (b)

Figure 4.6 : Fits of $M(K^+K^-)$ in the central $|\eta|$ region, $|\eta| \leq 0.7$, for leading (a) K^+ or (b) K^-. The lower panes show the residuals.

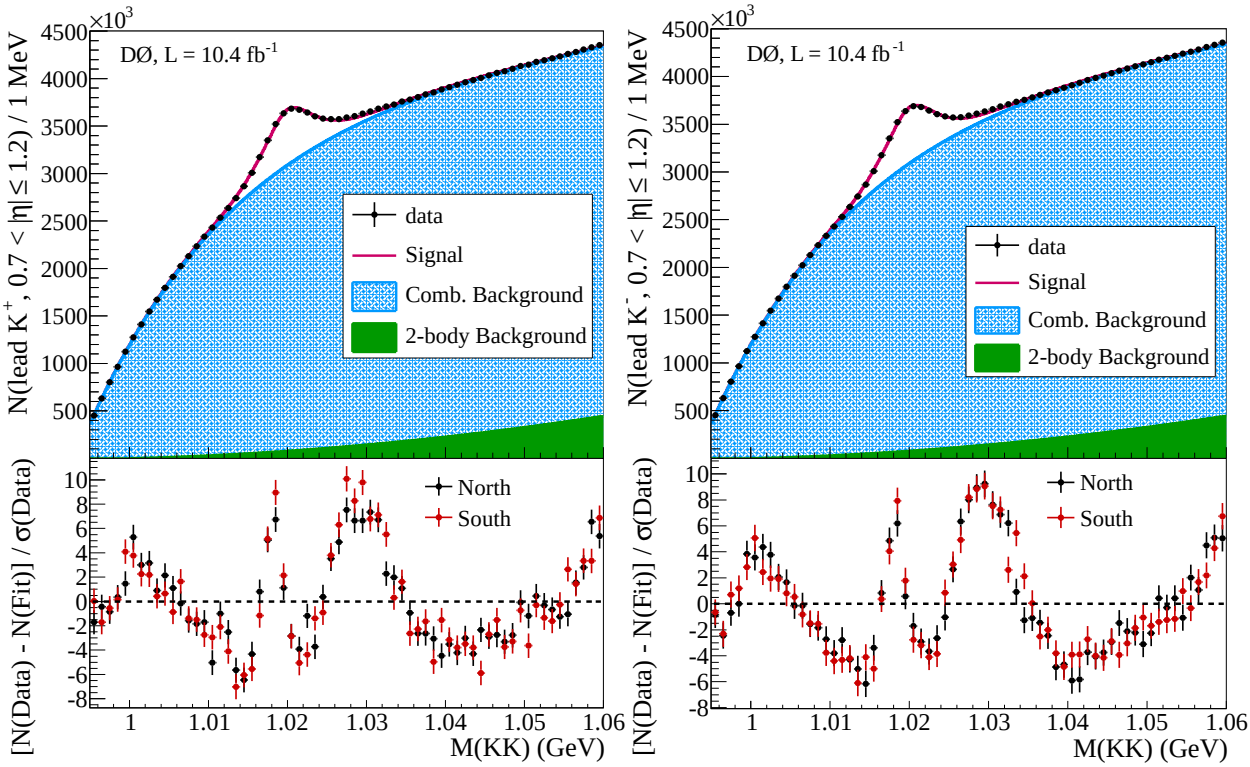

(a) (b)

Figure 4.7 : Fits of $M(K^+K^-)$ in the middle $|\eta|$ region, $0.7 < |\eta| \leq 1.2$, for leading (a) K^+ or (b) K^-. The lower panes show the residuals.

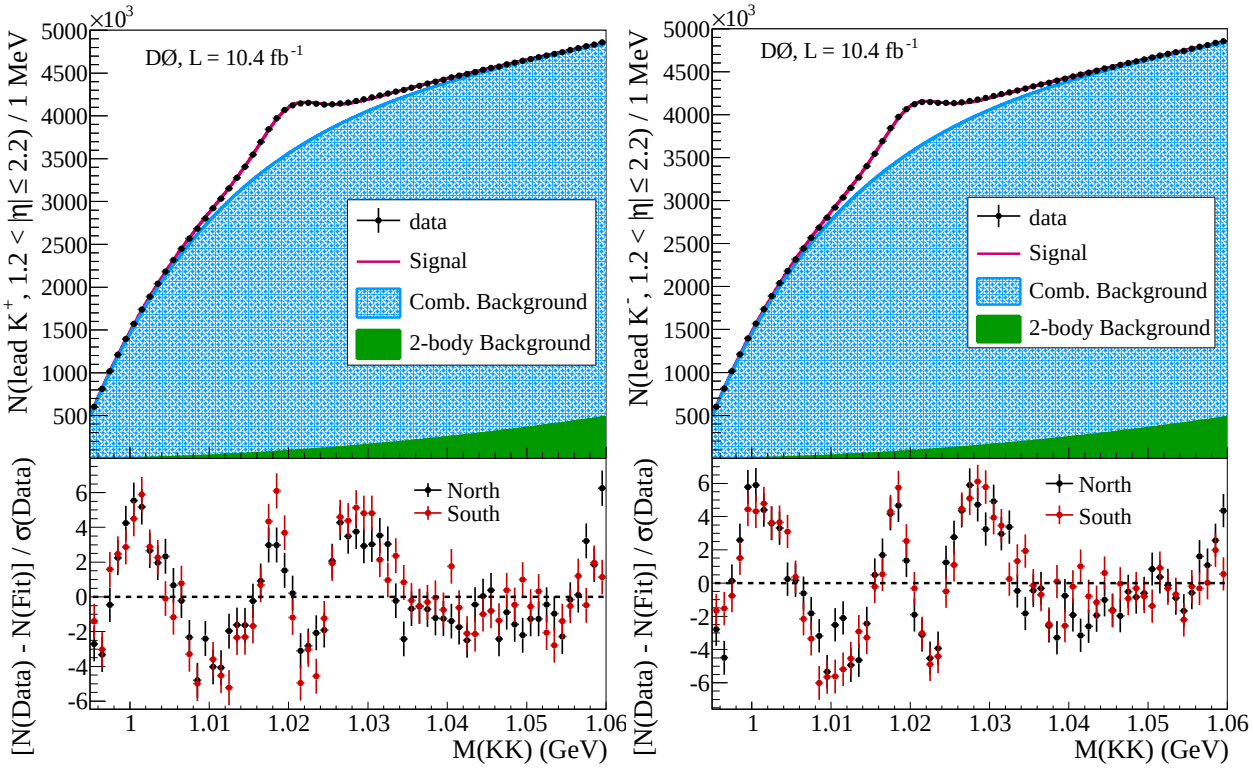

(a) (b)

Figure 4.8 : Fits of $M(K^+K^-)$ in the forward $|\eta|$ region, $1.2 < |\eta| \leq 2.2$, for leading (a) K^+ or (b) K^-. The lower panes show the residuals.

4.4 Weighting procedure

The values of $A_{\rm NS}$ can be used to equalize the relative reconstruction efficiencies for J/ψ and $K^{\pm}$ on both sides of the detector:

$$A_{\rm NS} = \frac{\varepsilon_N - \varepsilon_S}{\varepsilon_N + \varepsilon_S}, \tag{4.11}$$

$$\varepsilon_S = \varepsilon_N \frac{1 - A_{\rm NS}}{1 + A_{\rm NS}}. \tag{4.12}$$

If particles on the south side are assigned $\varepsilon_S = 1$, then particles on the north side are weighted so that $\varepsilon_N = \varepsilon_S$:

$$w_{\rm north} = \frac{1}{\varepsilon_N} = \frac{1 - A_{\rm NS}}{1 + A_{\rm NS}}. \tag{4.13}$$

The background distributions P, T, and E could contain events without real J/ψ or $K^{\pm}$ particles (i.e., distribution P, where a pion has been mis-labeled as a kaon), so the values of $A_{\rm NS}$ are scaled by the expected signal fraction of the $B^{\pm}$ candidate. The expected signal fraction F is a ratio of the signal probability density function to the total likelihood function. Using the notation of eq. 3.17:

$$F(M_{J/\psi K, E_K}) = \frac{\alpha f_S S}{\alpha(f_S S + f_P P + f_T T) + [1 - \alpha(f_S + f_P + f_T)]E}. \tag{4.14}$$

Fits without asymmetry parameters are performed on the $B^{\pm} \to J/\psi K^{\pm}$ data sample to set the parameters of S, P, T, and E for calculating the signal fraction. We use parameter sets fitted specifically for each bin of $|\eta(B^{\pm})|$, $p_T(B^{\pm})$ and $B^{\pm}$ charge, as applicable. Distributions of F are shown in Fig. 4.9.

By multiplying $A_{\rm NS}$ by the signal fraction F we are applying reconstruction asymmetry corrections to the signal asymmetry A_S, but not applying corrections to the background

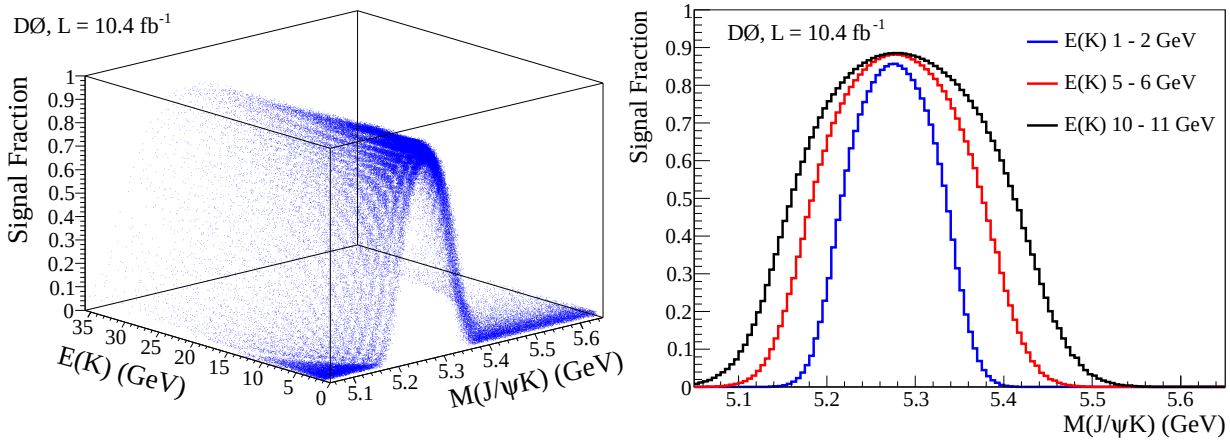

(a) 3D view

(b) 2D views in 3 E_K ranges

Figure 4.9 : Distributions of the signal fraction F as a function of mass $M(J/\psi K)$ and (a) kaon energy E_K, or (b) at select values of E_K.

asymmetry parameters. To test this method we use an analog of the weight in Eq. 4.13:

$$w_{\text{forward}} = \frac{1 - F A_{\text{FB}}}{1 + F A_{\text{FB}}}, \tag{4.15}$$

where A_{FB} is a test asymmetry injected into $B^{\pm} \to J/\psi K^{\pm}$ data with the sign of q_{FB} randomized. We then compare the results of the fit to the known injected asymmetry value. Figure 4.10 shows the results of this test when $F = 1$ for all events. Both the signal asymmetry and the background asymmetries return the injected value. Figure 4.11 shows the results when $F = F(M_{J/\psi K}, E_K)$, which exhibit the desired effect: the background asymmetry is consistent with zero for all input asymmetry values.

With this scaling, the overall weight for each event is:

$$w_n = w_{\text{magnet}} w_{J/\psi} w_{K^{\pm}}, \tag{4.16}$$

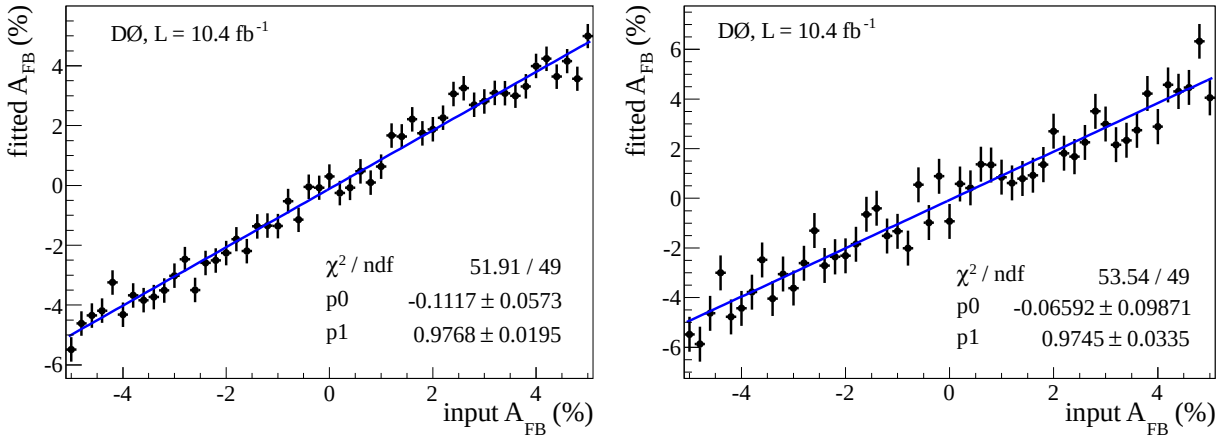

(a) (b)

Figure 4.10 : Injected asymmetry test with forward events weighted: $w_{\text{forward}} = [1 - A_{\text{FB}}(\text{input})]/[1 + A_{\text{FB}}(\text{input})]$. Both the (a) signal asymmetry A_S and (b) the background asymmetry A_E reproduce the input asymmetries.

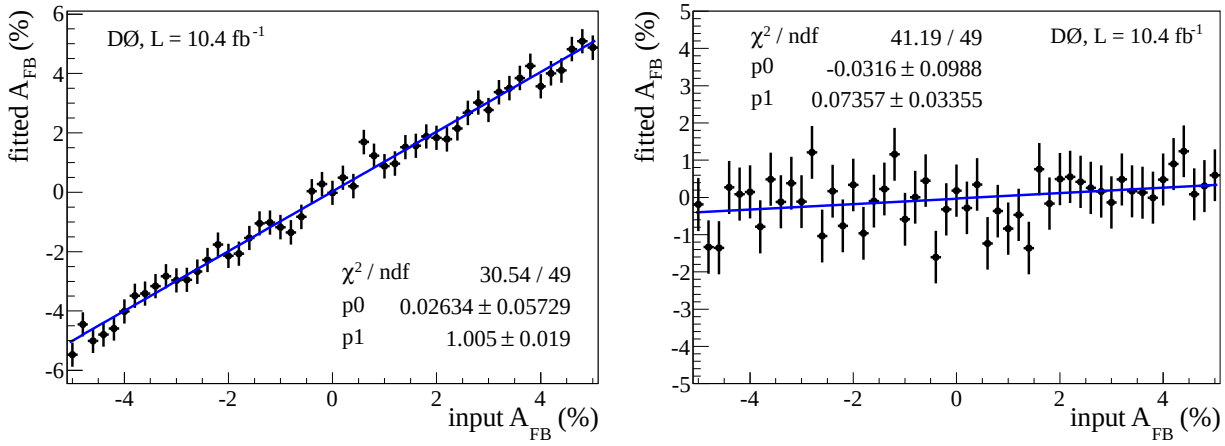

(a) (b)

Figure 4.11 : Injected asymmetry test with forward events weighted: $w = [1 - FA_{\text{FB}}(\text{input})]/[1 + FA_{\text{FB}}(\text{input})]$. Scaling the input asymmetry by the signal fraction F isolates the effect onto (a) the signal asymmetry, leaving (b) the background asymmetry consistent with zero.

where $w_{J/\psi}$ and $w_{K^\pm}$ are:

$$w_X = \begin{cases} 1 & \text{for south-side } X = J/\psi,\ K^\pm \\ [1 - FA_{\rm NS}(X)]/[1 + FA_{\rm NS}(X)] & \text{for north-side } X = J/\psi,\ K^\pm. \end{cases} \tag{4.17}$$

4.5 Cross-check of reconstruction asymmetry weights

The effect on $A_{\rm FB}(B^\pm)$ of applying the reconstruction asymmetry weights $w_{J/\psi}$ and $w_{K^\pm}$ is calculated by comparing weighted fits with unweighted, or "raw", fits:

$$A_{\rm FB}(\text{reconstructed}) = A_{\rm FB}(\text{raw}) - A_{\rm FB}(\text{weighted}). \tag{4.18}$$

By applying the reconstruction asymmetry weights we are essentially multiplying the J/ψ and $K^\pm$ reconstruction efficiencies. It has been shown previously that multiplying efficiencies is equivalent, to first order in the asymmetries, to adding reconstruction asymmetries to a raw asymmetry [42]. As a cross-check for our weighting method we calculate the expected $A_{\rm FB}$(reconstruction) by fitting the $B^\pm \to J/\psi K^\pm$ data in each bin of $[p_T(J/\psi),\ |\eta(J/\psi)|]$ and $|\eta(K^\pm)|$, and taking a weighted average of the $A_{\rm NS}$ values over these bins.

First we must consider how $A_{\rm NS}$ affecting the J/ψ or $K^\pm$ particles will correspond to $A_{\rm FB}$ for the $B^\pm$ candidate. The forward-backward charge is defined as $q_{\rm FB} = -q_B \,\mathrm{sgn}(\eta_B)$, and we can define a north-south charge for particle X as $q_{\rm NS}(X) = -\,\mathrm{sgn}(\eta_X)$. For B^+ mesons, $q_{\rm FB} = q_{\rm NS}(X)$ if particle X (J/ψ or K^+) is on the same side of the detector as the B^+. For B^- mesons with X on the side side of the detector as B^-, $q_{\rm FB} = -q_{\rm NS}(X)$. If X and $B^\pm$ are on opposite side, these relationships between $q_{\rm FB}$ and $q_{\rm NS}(X)$ are flipped. In practice, this defines two cases:

- Case 1: $A_{\rm FB} = A_{\rm NS}$. B^+ candidate in the same hemisphere as J/ψ or K^+; B^- candidate in the opposite hemisphere as J/ψ or K^-.

- Case 2: $A_{\rm FB} = -A_{\rm NS}$. B^- candidate in the same hemisphere as J/ψ or K^-; B^+ candidate in the opposite hemisphere as J/ψ or K^+.

Since the majority of $B^\pm$ candidates have decay products on the same side of the detector, Case 1 will dominate for B^+ events and Case 2 will dominate for B^- events.

To perform the weighted average cross-check, the data is split into the kinematic bins used to calculate $A_{\rm NS}(J/\psi)$ and $A_{\rm NS}(K^\pm)$ and then into Case 1 and Case 2. The $B^\pm \to J/\psi K^\pm$ distribution is fitted to extract the number of signal events per bin. The total number of signal events, labeled N_i, in a kinematic bin is the sum of signal events in Case 1 plus Case 2. To calculate $A_{\rm FB}$(reconstruction) we need the *effective* number of events, labeled n_i, which is the sum of signal events in Case 1 minus the sum of signal events in Case 2.

The asymmetry $A_{\rm FB}$(reconstruction) for particle X, labeled $A_{\rm FB}(X$ reco), is calculated according to:

$$A_{\rm FB}(X \text{ reco}) = \frac{1}{N} \sum_{\rm bins} n_i A_{{\rm NS},i}(X), \tag{4.19}$$

where N is the total number of fitted events over all bins. This weighted average depends on n_i, which reflects the difference in the number of B^+ and B^- candidates per kinematic bin. Therefore, when B^+ and B^- are combined, the values of n_i will be small and the effects of applying the reconstruction asymmetry weights will generally cancel. When B^+ and B^- samples are considered separately these corrections for detector reconstruction asymmetries will play a more significant role in the measurement of $A_{\rm FB}$.

The uncertainty on $A_{\rm FB}(X \text{ reco})$ is:

$$\sigma^2_{A_{\rm FB}}(X \text{ reco}) = \frac{1}{N^2} \sum_{\text{bins}} N_i^2 \sigma^2_{A_{{\rm NS},i}(X)} + A^2_{{\rm NS},i}(X) \sigma^2_{N_i}, \tag{4.20}$$

and the asymmetry $A_{\rm FB}$(reconstruction) is the sum: $A_{\rm FB}(J/\psi \text{ reco}) + A_{\rm FB}(K^\pm \text{ reco})$.

Comparisons of $A_{\rm FB}$(reconstruction) from this cross-check (Eq. 4.19) and the weighting method (Eq. 4.18) are listed in Table 4.4. The good consistency between these methods validates our choice to apply the reconstruction asymmetries via weights.

Table 4.4 : Comparison of methods to correct for reconstruction asymmetries

Sample	Reconstructed particle	Weighting method (Eq. 4.18)	Cross-check (Eq. 4.19)
B^+	J/ψ	-0.359%	$(-0.310 \pm 0.091)\%$
B^+	$K^\pm$	0.363%	$(0.401 \pm 0.136)\%$
B^+	both	0.004%	$(0.091 \pm 0.164)\%$
B^-	J/ψ	0.380%	$(0.330 \pm 0.090)\%$
B^-	$K^\pm$	-0.517%	$(-0.469 \pm 0.133)\%$
B^-	both	-0.137%	$(-0.139 \pm 0.161)\%$
$B^\pm$	J/ψ	0.0089%	$(0.0084 \pm 0.0905)\%$
$B^\pm$	$K^\pm$	-0.0638%	$(-0.0233 \pm 0.0955)\%$
$B^\pm$	both	-0.0558%	$(-0.0149 \pm 0.1316)\%$

A central benefit of the weighting method is the small uncertainty on $A_{\rm FB}(B^\pm)$ due to the statistical uncertainties on the $A_{\rm NS}$ measurements. Had we used the A(physics) =

$A(\text{raw}) - A(\text{reconstruction})$ method we would have an uncertainty of $\approx 0.13\%$, as seen in bottom right cell of Table 4.4, but this simple sum discards all asymmetry terms past the first order. The weighting method preserves these higher order terms, which bring along correlations between the asymmetries which must be accounted for in calculation of the overall uncertainty.

This uncertainty is determined using an ensemble test of 500 Gaussian variations of the $A_{\text{NS}}(J/\psi)$ and $A_{\text{NS}}(K^{\pm})$ values, shown in Fig. 4.12. In each trial the binned values of A_{NS} are randomized according to Gaussian distributions with widths determined by the statistical uncertainties of the measured A_{NS} values. The values of q_{FB} are also randomized, but using the same random seed for each trial. This gives the distribution in Fig. 4.12 an arbitrary mean value, but the width of the distribution shows the small uncertainty, 0.003%, due to the uncertainties on $A_{\text{NS}}(J/\psi)$ and $A_{\text{NS}}(K^{\pm})$.

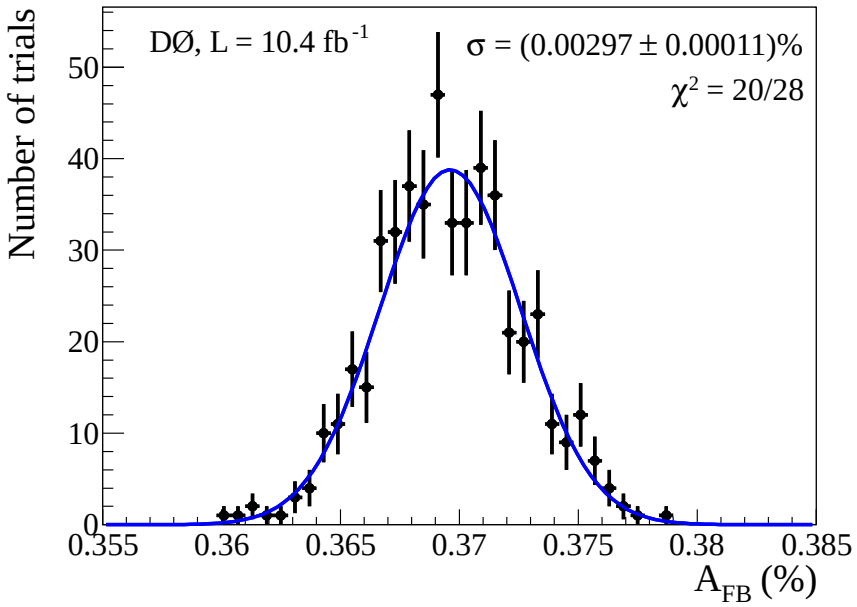

Figure 4.12 : Distribution of $A_{\rm FB}(B^{\pm})$ from 500 Gaussian randomizations of $A_{\rm NS}(J/\psi)$ and $A_{\rm NS}(K^{\pm})$. Each trial uses the same random seed to blind $q_{\rm FB}$, giving an arbitrary mean value of 0.37%. The width gives the statistical uncertainty of 0.003% from the reconstruction asymmetry weights.

Chapter 5

Measuring $A_{\rm FB}(B^{\pm})$

The final data sample, after $B^{\pm} \to J/\psi K^{\pm}$ selection cuts and the BDT discriminant cut, contains 160360 weighted events. The maximum likelihood fit, corrected for reconstruction asymmetries, gives 89466 $\pm$ 347 signal events. The fit parameters are listed in Table 5.1. Although the fit is unbinned, the data and fit quality are visualized with binned distributions of invariant mass $M(J/\psi K)$ for the sum and the difference in the numbers of forward and backward $B^{\pm}$ candidates. These are shown with their projected fits in Figs. 5.1 and 5.2, respectively. The lower panel of both figures shows the distributions of residuals, which compare the average value of the fit function in each bin with the data value and its statistical uncertainty. The quadrature sum of these residuals is taken as the χ^2 value:

$$\chi^2 = \sum_{\rm bins} \left([N({\rm Data}) - N({\rm Fit})]/\sigma({\rm Data}) \right)^2 . \tag{5.1}$$

The χ^2 value is 132.6 in the (forward + backward) distribution and 116.4 in the (forward $-$ backward) distribution. The fit has 26 free parameters and there are 240 bins across both distributions, which gives $\chi^2/{\rm ndf} = 249/214 = 1.16$.

We measure a signal asymmetry consistent with zero:

$$A_{\rm FB}(B^{\pm}) = [-0.24 \pm 0.41\,({\rm stat.})]\%. \tag{5.2}$$

The background asymmetries are also consistent with zero: $A_P = (8.16 \pm 15.95)\%$,

$A_T = (2.51 \pm 3.86)\%$, and $A_E = (-0.17 \pm 0.71)\%$.

5.1 Systematic Uncertainties

To determine systematic uncertainties on $A_{\rm FB}(B^{\pm})$ a number of variations are made to the analysis method. We test changes to the data sample, and the fit functions, biases in the fit algorithm, and alternate reconstruction asymmetry calculations. For sets of less than eight variations, half the largest change in the central value of $A_{\rm FB}(B^{\pm})$ is assigned as the systematic uncertainty. For larger sets the systematic uncertainty is one standard deviation:

$$\sigma = \sqrt{\sum [A_{\rm FB}(x) - \bar{A}_{\rm FB}]^2 / N}, \tag{5.3}$$

where $A_{\rm FB}(x)$ is the measured value of $A_{\rm FB}(B^{\pm})$ in a given variation, and $\bar{A}_{\rm FB}$ is the mean value of $A_{\rm FB}(B^{\pm})$ over all variations including the default measurement.

5.1.1 Data sample variations

Four alternative BDTs were considered:

- Minimum $M(J/\psi K)$ of the lower background sideband is increased from 4.0 GeV to 4.5 GeV to improve agreement of the background input variable distributions with the distributions of background events in the analysis range.

- Maximum $M(J/\psi K)$ of the upper background sideband is decreased from 7.0 GeV to 6.5 GeV.

Table 5.1 : Maximum likelihood fit parameters

Parameter	Value	Parameter	Value
f_S	0.5592 ± 0.0016	p_0	0.2647 ± 0.0115
f_P	0.0076 ± 0.0011	p_1	-0.3804 ± 0.0212
f_T	0.0306 ± 0.0011	p_2	0.1839 ± 0.0073
m_B^N	5.2747 ± 0.0003	m_B^S	5.2761 ± 0.0003
f^N	0.0840 ± 0.0068	f^S	0.1934 ± 0.0100
c_0^N	0.0875 ± 0.0004	c_0^S	0.0886 ± 0.0004
c_1^N	-0.7268 ± 0.0036	c_1^S	-0.7336 ± 0.0041
c_2^N	0.1027 ± 0.0015	c_2^S	0.1173 ± 0.0017
c_3^N	0.4727 ± 0.0235	c_3^S	0.6119 ± 0.0146
s_0	-2.4486 ± 0.0315	A_S	-0.0024 ± 0.0041
s_1	-1.0770 ± 0.0274	A_P	0.0816 ± 0.1595
s_2	0.4489 ± 0.0136	A_T	0.0252 ± 0.0386
t	5.1282 ± 0.0030	A_E	-0.0017 ± 0.0071

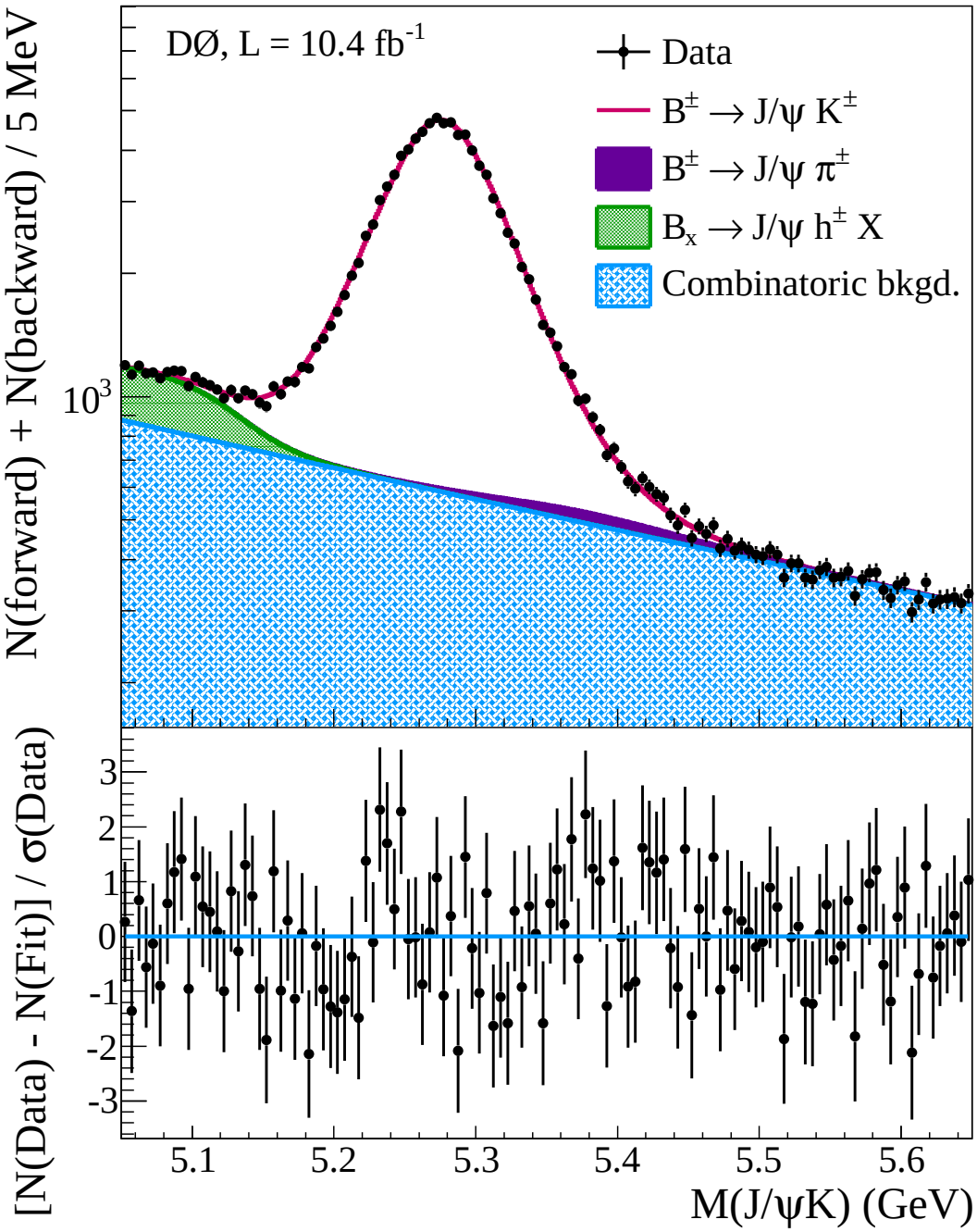

Figure 5.1 : Invariant mass $M(J/\psi K)$ of (forward + backward) events with fitted distributions. The lower pane shows the residuals, $[N(\text{Data}) - N(\text{Fit})]/\sigma(\text{Data})$.

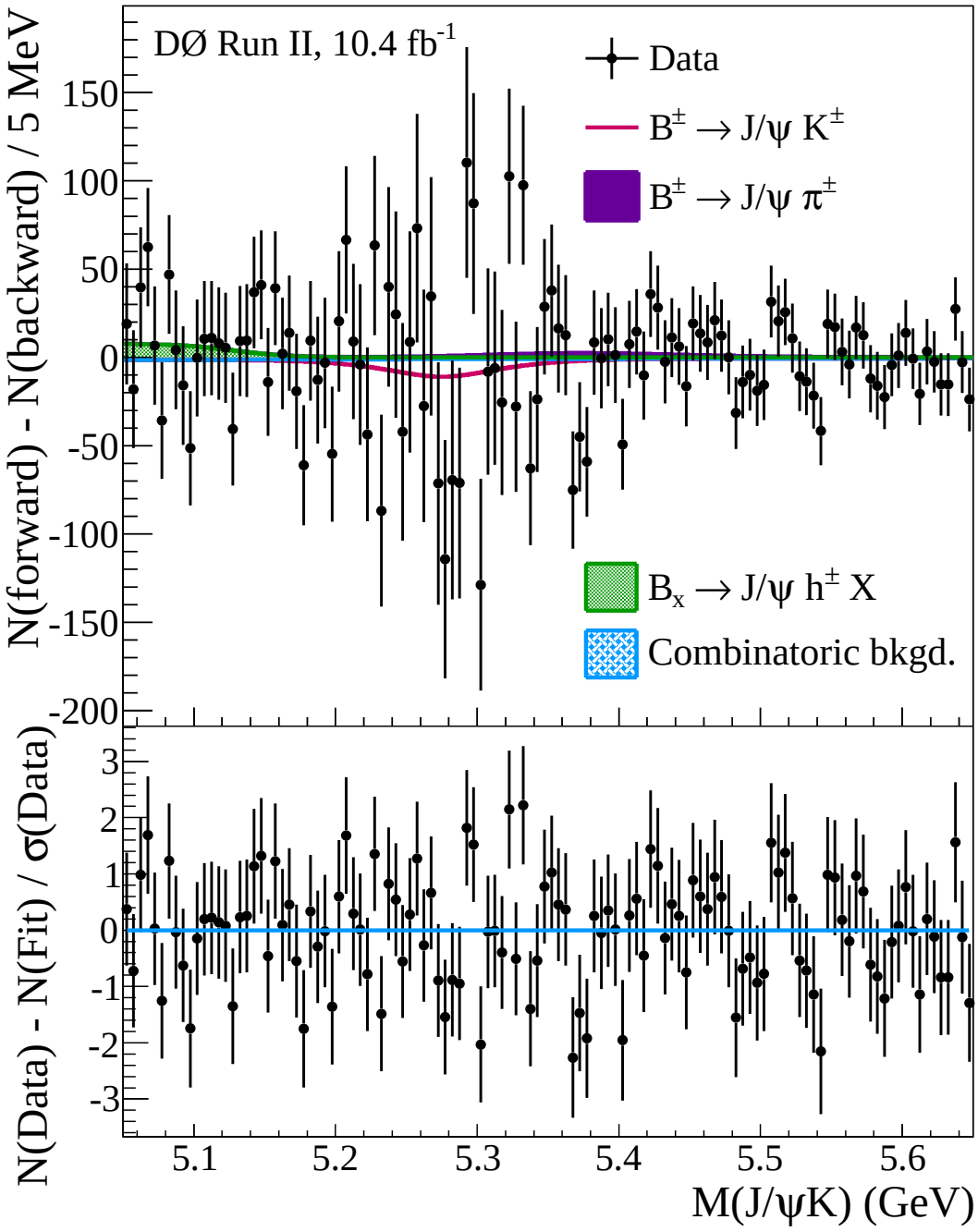

Figure 5.2 : Invariant mass $M(J/\psi K)$ of (forward − backward) events with fitted distributions which include the asymmetry parameters A_i. The lower pane shows the residuals, $[N(\text{Data}) - N(\text{Fit})]/\sigma(\text{Data})$.

- The BDT is trained without isolation variables to test any bias against high momentum B mesons embedded in a jet. No bias is observed when comparing event fractions with $p_T(B^{\pm}) > 15$ GeV.

- Maximum $p_T(B^{\pm}) = 20$ GeV in the background and MC signal samples, a cap used in initial versions of this analysis.

For each of these variations the BDT discriminant cut was set at -0.02, optimized to give the smallest statistical uncertainty when $p_T(B^{\pm})$ was capped at 20 GeV. These variations give an uncertainty of 0.115% on $A_{\rm FB}(B^{\pm})$.

Different cuts on the BDT discriminant are also considered. From Fig. 3.13(a) we choose a symmetric variation of four bins above and below the default cut at -0.01. These variations give a systematic uncertainty of 0.124%. The total uncertainty from variations to the data sample is 0.169%.

5.1.2 Fit method variations

The lower limit of the analysis mass range was varied from 5.0 GeV/c^2 to 5.05 GeV/c^2 in 10 MeV steps. At each lower limit step the upper limit of the mass range was varied from 5.65 GeV/c^2 to 5.7 GeV/c^2, also in 10 MeV steps. This results in an uncertainty of 0.024% on $A_{\rm FB}(B^{\pm})$.

The threshold function T for partially reconstructed B mesons has a fixed slope parameter, $t_1 = 25$, and a floating inflection point t. The following variations were tested:

- Float both t and t_1

- Fix $t = 5.128$ and $t_1 = 25$
- Fix $t = 5.128$ and float t_1

These changes have a very small effect on $A_{\rm FB}(B^{\pm})$, adding an uncertainty of only 0.005%.

One of the most significant possible modifications to the fit function is removing the dependence on kaon energy. There are three functions that depend on E_K: the widths of the double Gaussian signal distribution, the slope of the exponential background distribution, and the factor of α which modifies the event fractions f_i. The forms of these dependences were determined specifically for this analysis, so rather than modify the functional forms we test removing E_K completely by setting parameters (c_1, c_2), (s_1, s_2), and/or (p_0, p_1, p_2) equal to zero. Seven combinations were tested:

- Choose 1 E_K dependence to float: σ_1, S, or α. (3 variations)
- Choose 2 E_K dependences to float. (3 variations)
- Remove all E_K dependences.

The systematic uncertainty from these changes is 0.038%.

Another possible function variation is to the background asymmetries. Asymmetries A_P, A_T, and A_E were varied as follows:

- 1 asymmetry out of (A_P, A_T, A_E) is set to zero (3 variations)
- Constrain $A_T = A_E$ and allow A_P to float
- Fix $A_T = A_E = 0$ and allow A_P to float

- Set all three asymmetries to zero

These variations give an uncertainty on $A_{\rm FB}(B^{\pm})$ of 0.039%.

The final fit function variation takes into account statistical uncertainty on the magnet polarity settings. These weights are determined by counting events with a certain charge and magnet polarity setting, and the counts have associated statistical uncertainties. We vary each of the eight counts up and down by the uncertainty $\sqrt{N}$. The changes to $A_{\rm FB}(B^{\pm})$ from these variations are negligible, resulting in an uncertainty of 0.001%. The total uncertainty from variations to the fit function is 0.060%.

5.1.3 Reconstruction asymmetry calculations

Different methods of calculating the reconstruction asymmetries $A_{\rm NS}(J/\psi)$ and $A_{\rm NS}(K^{\pm})$ are tested:

- Replace $A_{\rm NS}(J/\psi)$ with a measurement of $A_{\rm NS}(\mu)$, for each of the individual muons
- Replace $A_{\rm NS}(K^{\pm})$ with a measurement from a sample of random tracks.

All three combinations were tested: $A_{\rm NS}(J/\psi)$ and $A_{\rm NS}$(tracks); $A_{\rm NS}(\mu)$ and $A_{\rm NS}$(tracks); and finally $A_{\rm NS}(\mu)$ and $A_{\rm NS}(K^{\pm})$. The difference in $A_{\rm FB}(B^{\pm})$ values with these alternate reconstruction asymmetry samples gives a systematic uncertainty of 0.048%.

The measurements of $A_{\rm NS}(J/\psi)$ and $A_{\rm NS}(K^{\pm})$ have gone through several revisions, with changes in binning, selection cuts, or construction of the fit parameters. All possible combinations of older versions and the measurements described in sections 4.2 and 4.3 have been

tested, giving a systematic uncertainty of 0.016%. The total systematic uncertainty from reconstruction asymmetry sources is 0.051%.

5.1.4 Fit bias

The test of possible bias in the fit, shown in Fig. 3.15, reveals small non-linearities in the fit method. The offset is consistent with zero: $(-0.016 \pm 0.018)\%$; the slope is consistent with one: 0.999 ± 0.006. For the observed $A_{\rm FB}(B^{\pm})$ of -0.236%, this calibration line indicates a true asymmetry of -0.220%. The shift of $(0.016 \pm 0.018)\%$ is consistent with a shift of zero, so it is added as a systematic uncertainty.

All sources of uncertainty are summarized in Table 5.2, assuming they are uncorrelated for the combination.

Table 5.2 : Summary and combination of uncertainties

Source	Uncertainty
Statistical	0.41%
Alternative BDTs and Cuts	0.17%
Fit Function Variations	0.06%
Reconstruction Asymmetry Calculations	0.05%
Fit Bias	0.02%
Systematic Uncertainty	0.19%
Total Uncertainty	0.45%

5.2 Stability Tests

The stability of the asymmetry measurement is tested by dividing the data into subsets which are expected to have the same asymmetry. Figure 5.3 shows $A_{\rm FB}(B^{\pm})$ over time, with the earliest data at the bottom and the most recent data at the top. Figure 5.4(a) shows the data divided into the four magnet polarity settings, with the number of B^+ and B^- candidates within each setting equalized. Figure 5.4(b) shows the data separated into B^+ and B^- samples, with the number of candidates in the four polarity settings equalized. The use of separate signal parameters for the north and south sides of the detector was essential for bringing these values into agreement, although this method disrupts the instinctive expectation that $[A_{\rm FB}(B^+) + A_{\rm FB}(B^-)]/2 = A_{\rm FB}(B^{\pm})$. Table 5.3 gives the raw values of $A_{\rm FB}$ for each charged sample and shows how each of the reconstruction asymmetry weights contributes to the physical values of $A_{\rm FB}$. The final stability test, shown in Fig. 5.5, measures $A_{\rm FB}(B^{\pm})$ over a range of BDT cut values.

Table 5.3 : Reconstruction Asymmetry Corrections: $A_{\rm FB}$(raw) − $A_{\rm FB}$(reco) = $A_{\rm FB}$(phys).

Sample	$A_{\rm FB}$(raw)	$A_{FB}(J/\psi$ reco)	$A_{FB}(K^{\pm}$ reco)	$A_{\rm FB}$(phys)
B^-	−0.64%	0.05%	−0.52%	(−0.18 ± 0.65)%
$B^{\pm}$	−0.29%	0.01%	−0.06%	(−0.24 ± 0.41)%
B^+	0.60%	−0.03%	0.37%	(0.25 ± 0.65)%

As a cross-check, we remove the $B^{\pm}$ charge equalization from $w_{\rm magnet}$ and correct for the

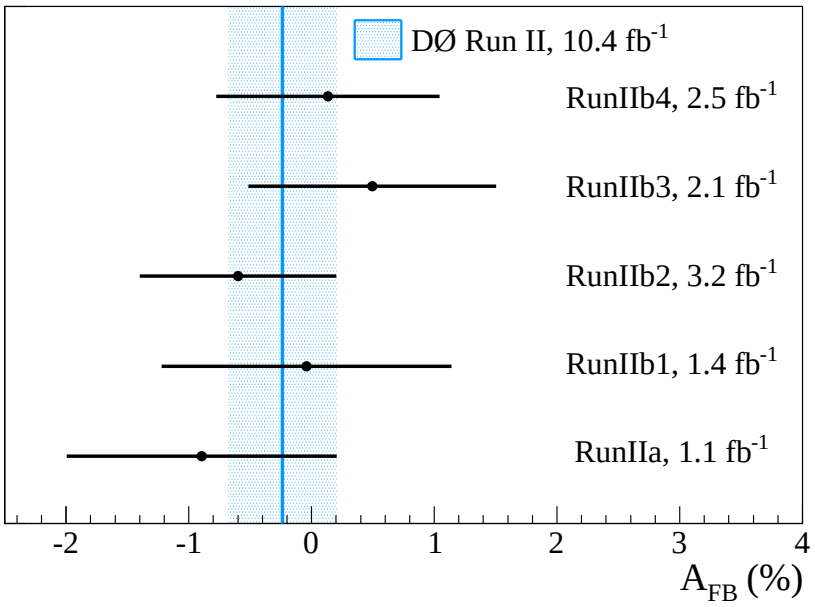

Figure 5.3 : The measurement of $A_{\mathrm{FB}}(B^{\pm})$ is consistent over time. The data points are shown with statistical uncertainties which reflect the integrated luminosity of the sample. The nominal result (blue band) is shown with the total uncertainty.

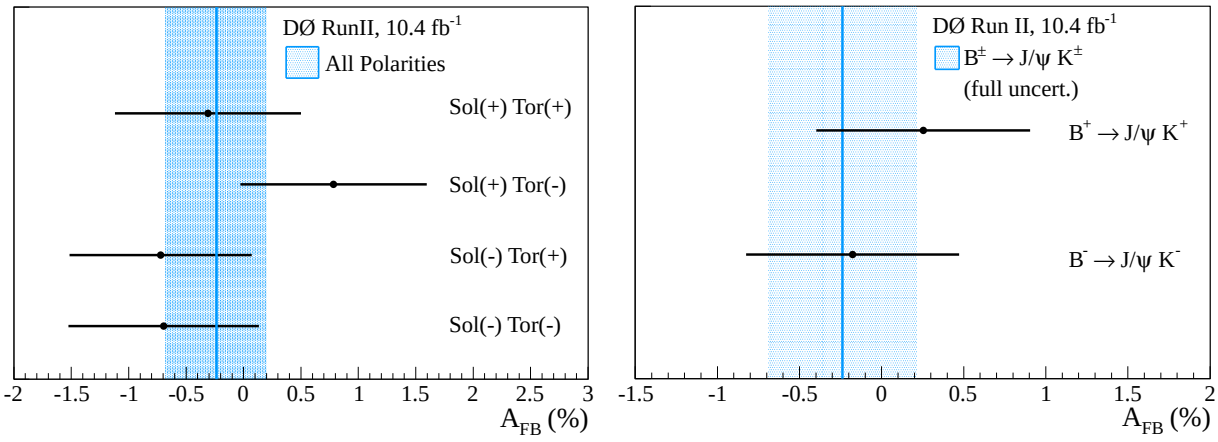

(a) (b)

Figure 5.4 : Measurements of $A_{\rm FB}(B^{\pm})$ in (a) different magnet polarity settings, with $N(B^{+}) = N(B^{-})$ within a polarity setting, and (b) for separate $B^{\pm}$ charges (b). Data points are shown with statistical uncertainties. The nominal result is shown in blue with the total uncertainty.

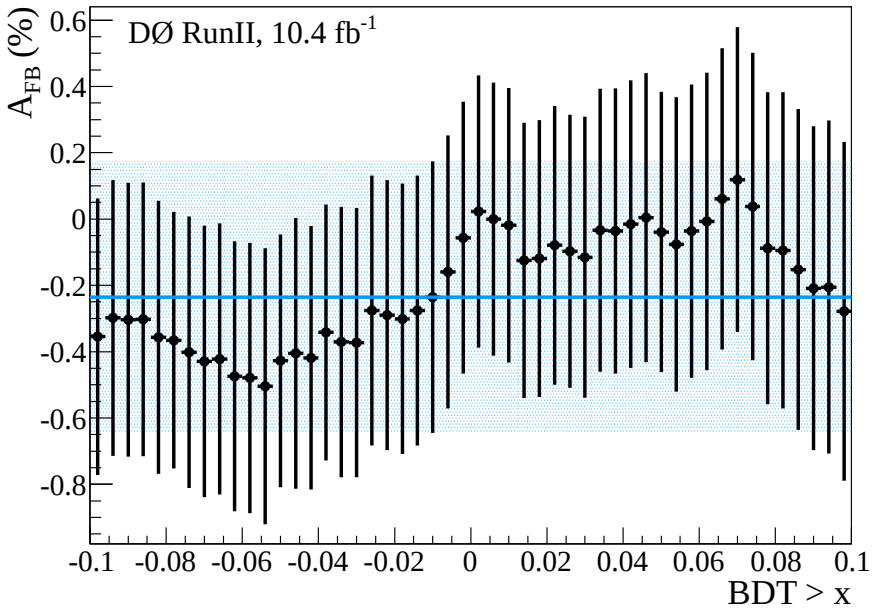

Figure 5.5 : Measurement of $A_{\rm FB}(B^{\pm})$ over a range of BDT cuts. The result at the selected value of BDT > -0.01 is shown in blue.

kaon charge asymmetry using a weight analogous to the reconstruction asymmetry weights $w_{J/\psi}$ and $w_{K^\pm}$. With these alterations we measure $A_{\rm FB}(B^\pm) = (-0.24 \pm 0.41)\%$, which is completely consistent with our nominal result. If the value of $q_{\rm FB}$ in the likelihood function is replaced with the $B^\pm$ charge q_B we can also measure the charge asymmetry in $B^\pm \to J/\psi K^\pm$. We measure $A(B^\pm) = 0.759\% \pm 0.447\%$, which is consistent with previous results [37].

Chapter 6

Comparing $A_{\rm FB}(B^{\pm})$ to the Standard Model

To compare the measurement of $A_{\rm FB}(B^{\pm})$ in data to the standard model (SM), the MC@NLO simulation described previously (sec. 1.6) is analyzed with the same reconstruction code as used for data, applying $B^{\pm} \to J/\psi K^{\pm}$ selections and weights to model the muon trigger effects. Additionally, reconstructed muon and kaon tracks must match tracks from generated $B^{\pm} \to J/\psi K^{\pm}$ decays. Since matching reconstructed $B^{\pm}$ candidates to generated $B^{\pm}$ mesons leaves no background events, $A_{\rm FB}^{\rm SM}(B^{\pm})$ is calculated directly:

$$A_{\rm FB} = \frac{N(q_{\rm FB} > 0) - N(q_{\rm FB} < 0)}{N(q_{\rm FB} > 0) + N(q_{\rm FB} < 0)} \tag{6.1}$$

Eight million events are generated in each solenoid/toroid magnet polarity setting. After all selection cuts the sample has 77157 events in the setting which is the default for DØ MC generation, and approximately 20000 events in each of the other settings. As in the data sample, the number of $B^{\pm}$ candidates in the four magnet polarity settings and the number of B^{+} and B^{-} candidates are equalized with the weight $w_{\rm magnet}$.

6.1 MC@NLO Trigger Weighting

Since the effects of the trigger system are not modeled in MC, the muon trigger weights w_{μ_1}, w_{μ_2}, and $w_{\mathcal{S}_{xy}}$ are applied to the MC events. Using the procedure outlined in sec. 3.3.1,

additional weights are derived to ensure optimal matching between estimated signal data and the MC@NLO simulation in distributions of $p_T(\mu_1)$, $|\eta(\mu_1)|$, and $|\eta(B^{\pm})|$. Figures 6.1 – 6.4 compare the data and MC@NLO distributions before and after weighting.

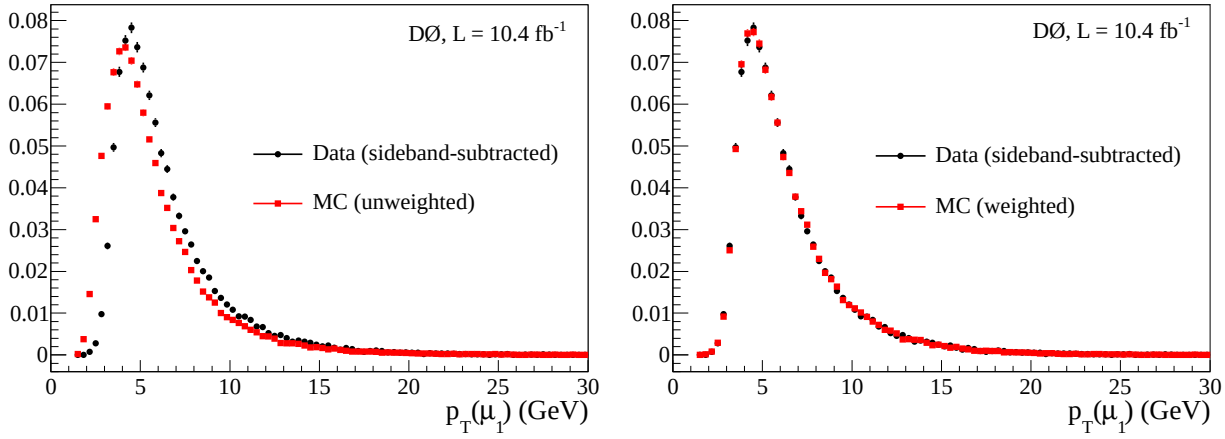

(a) (b)

Figure 6.1 : Distributions of $p_T(\mu_1)$ in MC@NLO (red squares) and estimated signal data (black circles), (a) before and (b) after reweighting.

6.2 Reconstruction Asymmetries in DØ MC

Regardless of the event generation program, all DØ MC uses the GEANT3 program for detector simulation. We measure $A_{\rm NS}(J/\psi)$ and $A_{\rm NS}(K^{\pm})$ in MC generated with PYTHIA since this leading order MC uses the same detector simulation but does not model the forward-backward production asymmetry. Using a variety of PYTHIA MC samples, we isolate $\phi \to K^+K^-$ and $J/\psi \to \mu^+\mu^-$ decays using the Particle Data Group identification

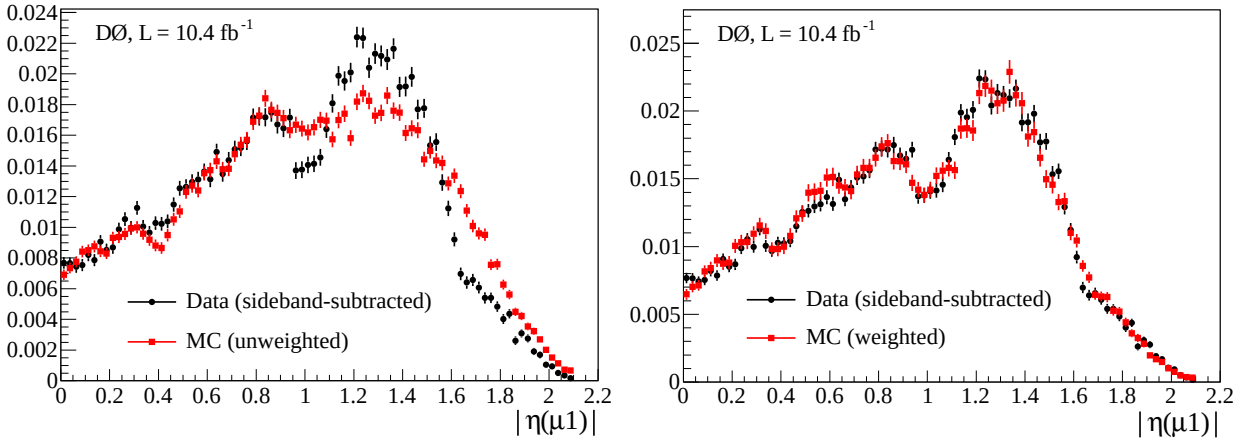

(a) (b)

Figure 6.2 : Distributions of $|\eta(\mu_1)|$ in MC@NLO (red squares) and estimated signal data (black circles), (a) before and (b) after reweighting.

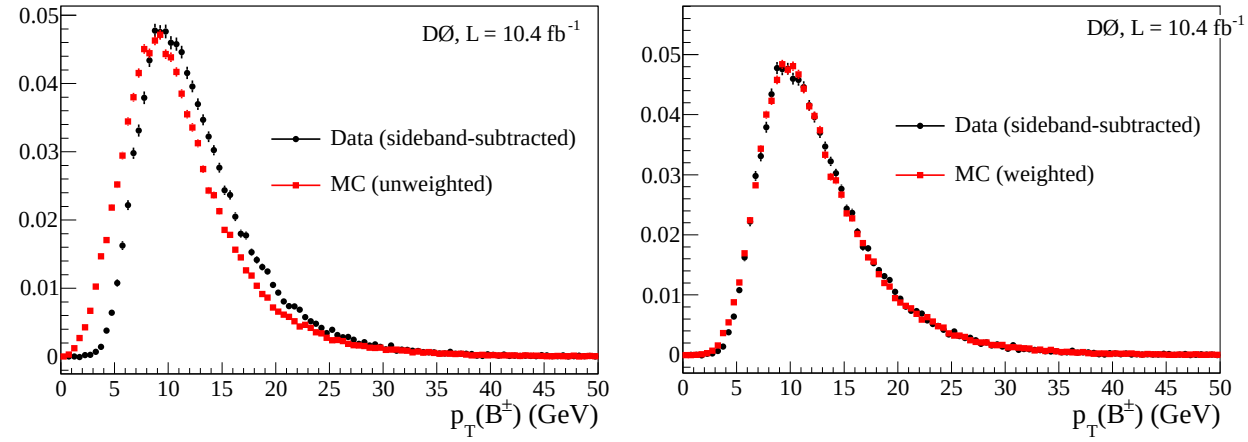

(a) (b)

Figure 6.3 : Distributions of $p_T(B^{\pm})$ in MC@NLO (red squares) and estimated signal data (black circles), (a) before and (b) after reweighting. The weight derived for $p_T(\mu_1)$ also brings these distributions into agreement.

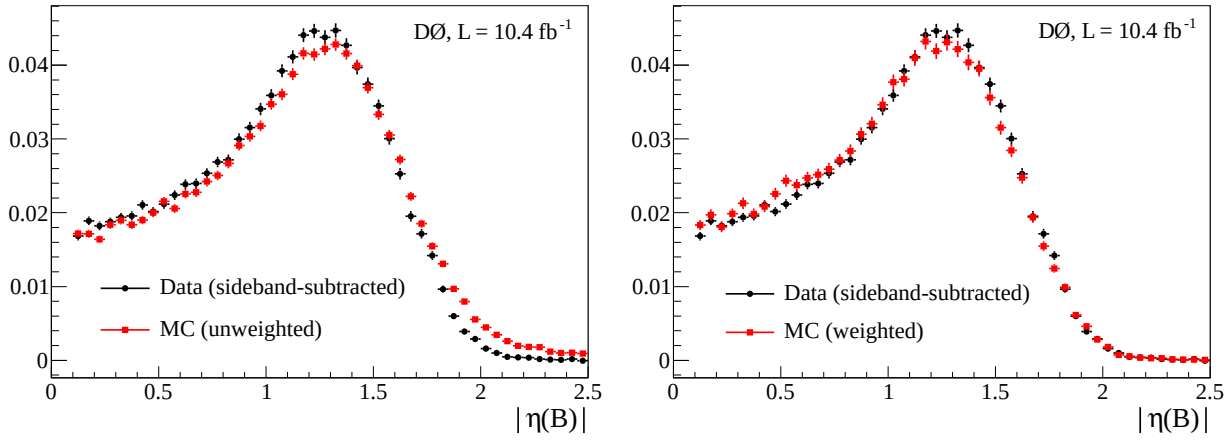

(a) (b)

Figure 6.4 : Distributions of $|\eta(B^{\pm})|$ in MC@NLO (red squares) and estimated signal data (black circles), (a) before and (b) after reweighting.

numbers [3]. A simulation of $B_s \to J/\psi(\mu\mu)\phi(K^+K^-)$ yields 241094 $\phi \to K^+K^-$ decays. A total of 658113 $J/\psi \to \mu^+\mu^-$ decays are taken from a combination of generic QCD simulation, $p\bar{p} \to J/\psi(\mu\mu)X$ simulation, $p\bar{p} \to b\bar{b}$ (or $c\bar{c}$) simulation with two muons in the final state, and unpolarized $gg \to \chi_c$ or J/ψ simulation.

We measure $A_{\rm NS}(J/\psi)$ and $A_{\rm NS}(K^{\pm})$ using the same bin structure as for data. Background is removed from both samples using the particle identification numbers, so the north-south asymmetries are calculated directly by counting north-side and south-side events. Figure 6.5 shows $A_{\rm NS}^{\rm MC}(J/\psi)$ and the muon placement distribution in $\eta - \phi$ space. Figure 6.6 shows the same distributions for $A_{\rm NS}^{\rm MC}(K^{\pm})$. The asymmetry values are listed in Table 6.1.

Comparison of Figs. 4.4 and 6.5(b) shows that the Monte Carlo simulation is much less affected by asymmetries in the detector material. In particular, the dependence of $A_{\rm NS}(J/\psi)$

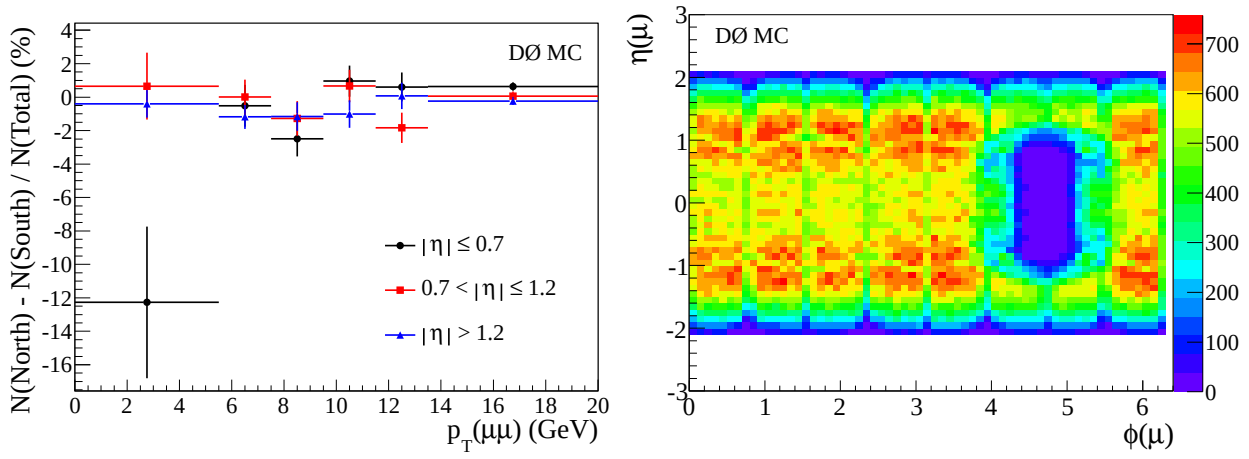

(a) (b)

Figure 6.5 : Distributions of PYTHIA MC J/ψ (a) north-south asymmetries in $|\eta|$ and p_T bins, and (b) muon placement in $\eta - \phi$ bins.

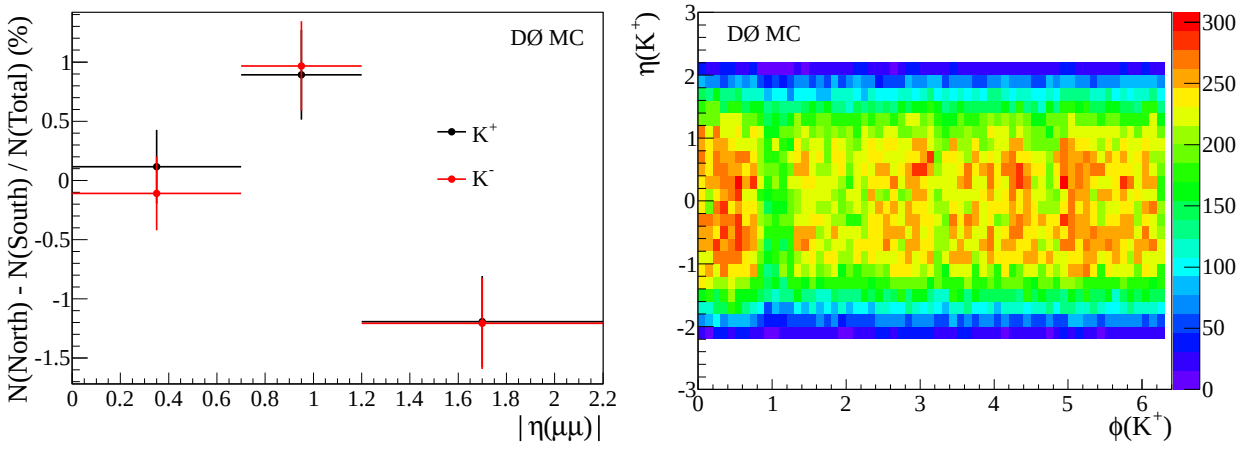

(a) (b)

Figure 6.6 : Distributions of PYTHIA MC $\phi \to K^+K^-$ (a) north-south asymmetries in $|\eta|$ bins, and (b) placement of K^+ particles in η-ϕ bins (the distribution for K^- is identical, qualitatively).

Table 6.1 : North-south asymmetries $A_{\rm NS}(J/\psi)$ and $A_{\rm NS}(K^{\pm})$ in PYTHIA MC.

$p_T(J/\psi)$ (GeV/c)	$\lvert\eta(J/\psi)\rvert \leq 0.7$	$0.7 < \lvert\eta(J/\psi)\rvert \leq 1.2$	$\lvert\eta(J/\psi)\rvert > 1.2$
< 5.5	-12.27 ± 4.54	0.66 ± 2.00	-0.41 ± 0.82
5.5 - 7.5	-0.52 ± 1.25	0.01 ± 1.04	-1.18 ± 0.72
7.5 - 9.5	-2.49 ± 1.05	-1.28 ± 1.04	-1.16 ± 0.85
9.5 - 11.5	0.96 ± 0.93	0.67 ± 0.96	-1.01 ± 0.82
11.5 - 13.5	0.61 ± 0.86	-1.84 ± 0.91	-0.07 ± 0.79
> 13.5	0.64 ± 0.24	0.06 ± 0.28	-0.23 ± 0.24
K charge	$\lvert\eta(K^{\pm})\rvert \leq 0.7$	$0.7 < \lvert\eta(K^{\pm})\rvert \leq 1.2$	$1.2 < \lvert\eta(K^{\pm})\rvert \leq 2.2$
K^+	0.12 ± 0.31	0.89 ± 0.38	-1.19 ± 0.38
K^-	-0.11 ± 0.31	0.97 ± 0.38	-1.21 ± 0.38

on p_T in data is not reproduced in the MC, which suggests that the primary source of the large negative asymmetries in data is not from active detector material which is modeled in GEANT. The values of $A_{\rm NS}(K^{\pm})$ are generally an amalgamation of small effects throughout each bin (Fig. 6.6(b)). The similarity between $A_{\rm NS}(K^{+})$ and $A_{\rm NS}(K^{-})$ is greatly improved in MC, since we can isolate $\phi \to K^{+}K^{-}$ signal using the MC particle identification rather than fits.

6.3 $A_{\rm FB}(B^{\pm})$ in MC@NLO

We calculate $A_{\rm FB}(B^{\pm})$ in MC@NLO using binned histograms since there is no background component requiring a fit. Each candidate is given the weight $w_n = w_{\rm trigger} w_{\rm magnet} w_{J/\psi} w_{K^{\pm}}$, which includes the trigger weights and reconstruction asymmetry weights described above. "Difference" histograms binned in $|\eta(B^{\pm})|$ or $p_T(B^{\pm})$ are filled using positive or negative weights based on the value of $q_{\rm FB}$. "Sum" histograms are filled with positive weights to find the total number of events per bin. $A_{\rm FB}$ in each bin, with statistical uncertainty, is calculated by dividing a difference histogram by the corresponding sum histogram. We measure:

$$A_{\rm FB}^{\rm SM}(B^{\pm}) = [2.31 \pm 0.34\,({\rm stat.})]\% \tag{6.2}$$

Systematic uncertainties from four sources are considered: renormalization and factorization energy scale choice, parton distribution function (PDF) set uncertainties, b quark fragmentation models, and possible biases in the measurement technique. MC@NLO defines energy scales for renormalization (μ_R) and for factorization of the initial partons (μ_F) [20].

For the process $p\bar{p} \to b\bar{b}X$:

$$\mu_{R,F} = m(b) + \sqrt{[p_T^2(b) + p_T^2(\bar{b})]/2}, \tag{6.3}$$

where the b quark mass $m(b)$ is set to 4.75 GeV [43]. Since $A_{\rm FB}^{b\bar{b}}$ is zero at leading-order, there is a large scale dependence in predictions at next-to-leading-order [44]. Both scales are varied independently from $\frac{1}{2}\mu_{R,F}$ to $2\mu_{R,F}$ to estimate an uncertainty due to uncalculated higher orders. Six million MC events were generated in each of the eight new scale combinations. All scale variation samples are generated in the default magnet polarity setting, so the values of $A_{\rm FB}(B^{\pm})$ are compared to the nominal value from the same setting of $[1.39 \pm 0.40\,({\rm stat})]\%$. Figure 6.7 shows the scale variations with respect to the nominal scale. Half the largest spread of variations gives a systematic uncertainty of 0.44%.

The PDF uncertainty is calculated using a system of weights. The CTEQ6M1 PDF set is created from fits which have twenty eigenvectors, each with an associated uncertainty. Using the momentum transfer Q^2 of the primary interaction, the initial parton flavors, and the fractions of the p or $\bar{p}$ momentum carried by the initial partons we calculate an array of forty weights which mirror the effect of shifting each eigenvector up or down by its uncertainty. We calculate $A_{\rm FB}(B^{\pm})$ forty times, applying one weight at a time from the array. The standard deviation of the variations is 0.03%, which is applied as a systematic uncertainty.

We estimate an uncertainty due to b quark fragmentation by weighting the MC so that the fragmentation of b quarks into $B^{\pm}$ mesons follows a Bowler fragmentation function tuned to reproduce LEP or SLD data. The Bowler function [46] is:

$$f(z) \propto z^{-(1+br_q m_b^2)}(1-z)^a \exp(-bm_T^2/z), \tag{6.4}$$

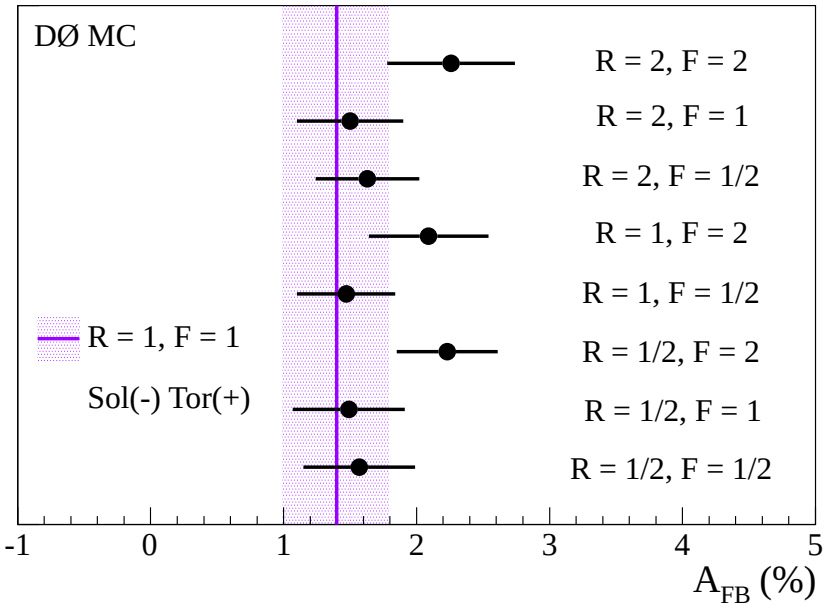

Figure 6.7 : Measurements of $A_{\rm FB}^{SM}(B^{\pm})$ in different scale samples. Half the largest spread is 0.44%. Points show statistical uncertainties.

where m_b is the b quark mass set to 5.0 GeV, and $m_T = \sqrt{m^2 + p_T^2}$ is the transverse mass of the B hadron with $m = 5.0$ GeV and $p_T = 0.39$ GeV. Parameters a, b, and r_q can be tuned for a given dataset. We calculate the fragmentation variable as:

$$z = p(B^{\pm})_{||}/p(b), \tag{6.5}$$

where $p(B^{\pm})$ is the component of $p(B^{\pm})$ in the direction of the b jet. To estimate b jet momentum we identify the earliest produced MC b quark that is within $\Delta\mathcal{R} < 0.5$ of the $B^{\pm}$ meson. The parameters for the LEP and SLD tunes are:

- LEP: $a = 1.03$, $b = 1.31$, $r_q = 0.897$.
- SLD: $a = 1.30$, $b = 1.58$, $r_q = 0.98$.

The Bowler functions with LEP and SLD tunes are shown in Fig. 6.8, along with the z variable in our default MC@NLO+HERWIG MC. Because we do not have an exact calculation of the jet momentum, the distribution in HERWIG extends past $z = 1$. We weight these events as if z were equal to 1, which maintains the continuity of z in the weighted MC. In LEP tuned MC $A_{\rm FB}^{\rm SM}(B^{\pm}) = (2.01 \pm 0.39)\%$, and in SLD tuned MC $A_{\rm FB}^{\rm SM}(B^{\pm}) = (1.82 \pm 0.42)\%$. Half the largest spread between our default MC@NLO+HERWIG and these variations gives an uncertainty of 0.25%.

The MC calculation is tested for bias with the same procedure as data: events are randomly categorized as forward or backward, and then a percentage of randomly selected events have $q_{\rm FB}$ flipped to inject an asymmetry (Fig. 6.9). Five ensemble tests are combined and the distribution of measured $A_{\rm FB}(B^{\pm})$ versus $A_{\rm FB}$(input) is fitted with a line. As in the

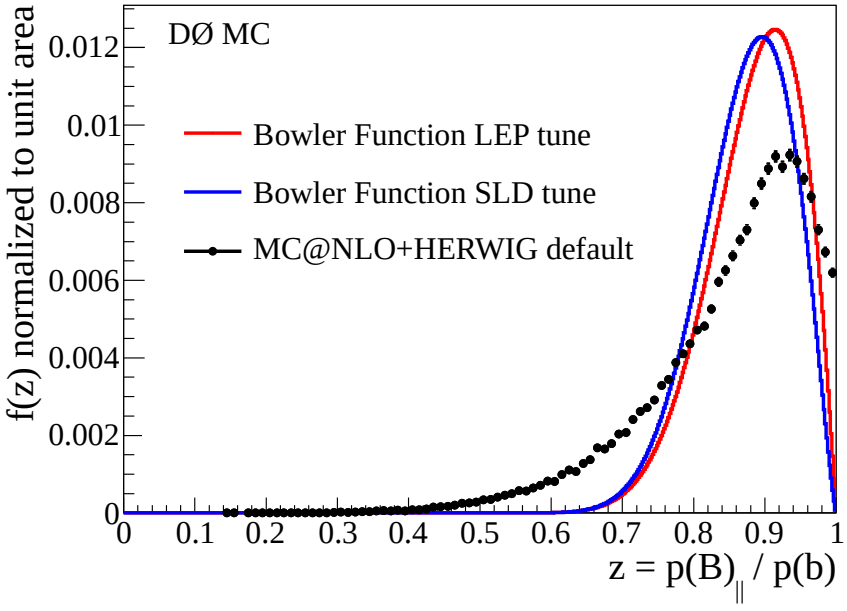

Figure 6.8 : Bowler functions tuned to LEP (red) and SLD (blue) data, along with fragmentation variable $z = p(B^{\pm})_{||}/p(b)$ in MC@NLO+HERWIG MC (points).

data calibration, the line parameters are consistent with an offset of zero and a slope of one, so all adjustments are consistent with zero. The indicated adjustment is 0.01% for all bins, and is negligible compared to all other uncertainties.

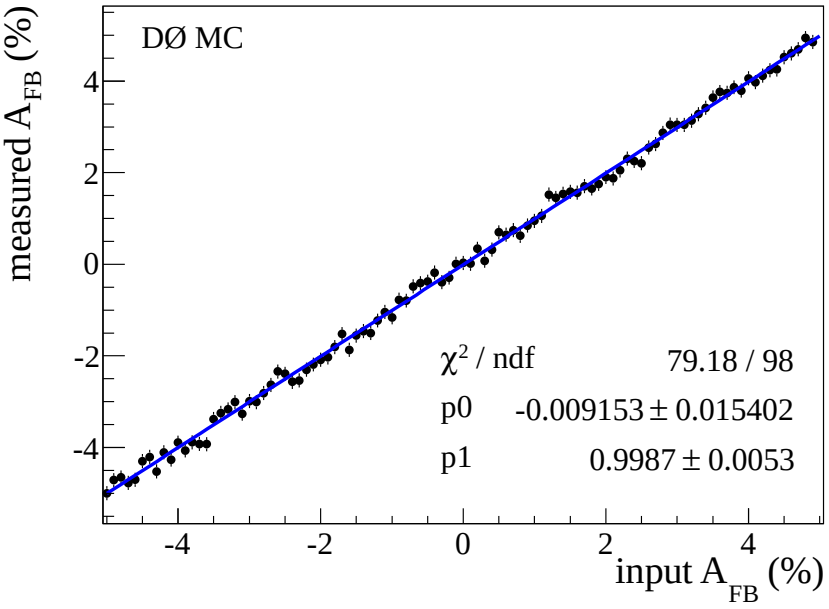

Figure 6.9 : Calibration of $A_{\rm FB}^{\rm SM}(B^{\pm})$ in MC@NLO. Each point is the average of five tests with different random seeds. Because the offset is consistent with zero and the slope is consistent with one, the shift from measured $A_{\rm FB}(B^{\pm})$ to $A_{\rm FB}$(input) is included as a systematic uncertainty.

With these uncertainties $A_{\rm FB}^{\rm SM}(B^{\pm}) = [2.31 \pm 0.34\,(\text{stat.}) \pm 0.51\,(\text{syst.})]\%$.

6.4 Binned Measurements of $A_{\rm FB}(B^{\pm})$

Table 6.2 lists the values of $A_{\rm FB}^{\rm SM}$ in bins of $p_T(B^{\pm})$ and $|\eta(B^{\pm})|$ with all associated uncertainties. Figure 6.10 shows measurements of $A_{\rm FB}(B^{\pm})$ and $A_{\rm FB}^{\rm SM}(B^{\pm})$ versus transverse

momentum and pseudorapidity. The fully reconstructed $J/\psi K^{\pm}$ final state produces good kinematic agreement between reconstructed and generated $B^{\pm}$ mesons, as shown in Fig. 6.11, so corrections to recover the true $B^{\pm}$ kinematics are unnecessary. The average p_T of the $B^{\pm}$ mesons is 12.9 GeV. We find that $A_{\rm FB}(B^{\pm})$ is systematically lower than $A_{\rm FB}^{\rm SM}(B^{\pm})$ for all pseudorapidities, and for $p_T(B) = 9$ – 30 GeV. Considering the MC systematic uncertainties to be correlated (uncorrelated), Fig. 6.10 (a) has $\chi^2 = 10.3\,(11.8)$ for three bins and Fig. 6.10 (b) has $\chi^2 = 6.6\,(7.0)$ for seven bins.

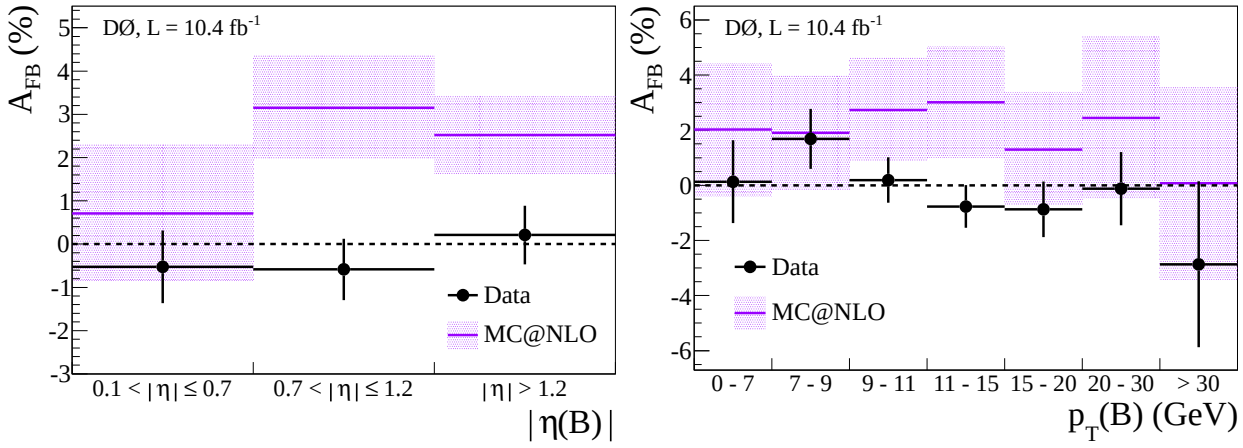

(a) (b)

Figure 6.10 : Comparison of $A_{\rm FB}(B^{\pm})$ and $A_{\rm FB}^{\rm SM}(B^{\pm})$ in bins of (a) $|\eta_B|$ and (b) $p_T(B)$. Data points and MC bands include statistical uncertainties convoluted with systematic uncertainties (Table 6.2).

Table 6.2 : $A_{\mathrm{FB}}(B^{\pm})$ and uncertainties in MC@NLO

Bin	A_{FB} (%)	Uncertainties (%)			
		Statistical	Scale choice	Fragmentation	PDF
$B^{\pm}$	2.31	0.34	0.44	0.25	0.03
B^{+}	3.39	0.48	0.68	0.14	0.05
B^{-}	1.24	0.48	0.78	0.37	0.03
$\lvert\eta(B^{\pm})\rvert$ 0.1 – 0.7	0.72	0.71	1.39	0.03	0.01
$\lvert\eta(B^{\pm})\rvert$ 0.7 – 1.2	3.08	0.60	0.99	0.24	0.02
$\lvert\eta(B^{\pm})\rvert > 1.2$	2.61	0.51	0.62	0.37	0.05
$p_T(B^{\pm}) < 7$	0.83	0.85	2.15	0.64	0.05
$p_T(B^{\pm})$ 7 – 9	1.30	0.80	1.89	0.17	0.06
$p_T(B^{\pm})$ 9 – 11	2.74	0.78	1.62	0.47	0.03
$p_T(B^{\pm})$ 11 – 15	2.30	0.67	1.83	0.50	0.02
$p_T(B^{\pm})$ 15 – 20	1.21	0.89	1.81	0.20	0.03
$p_T(B^{\pm})$ 20 – 30	3.01	1.23	2.65	0.34	0.04
$p_T(B^{\pm}) > 30$	-0.12	2.61	2.31	0.53	0.09

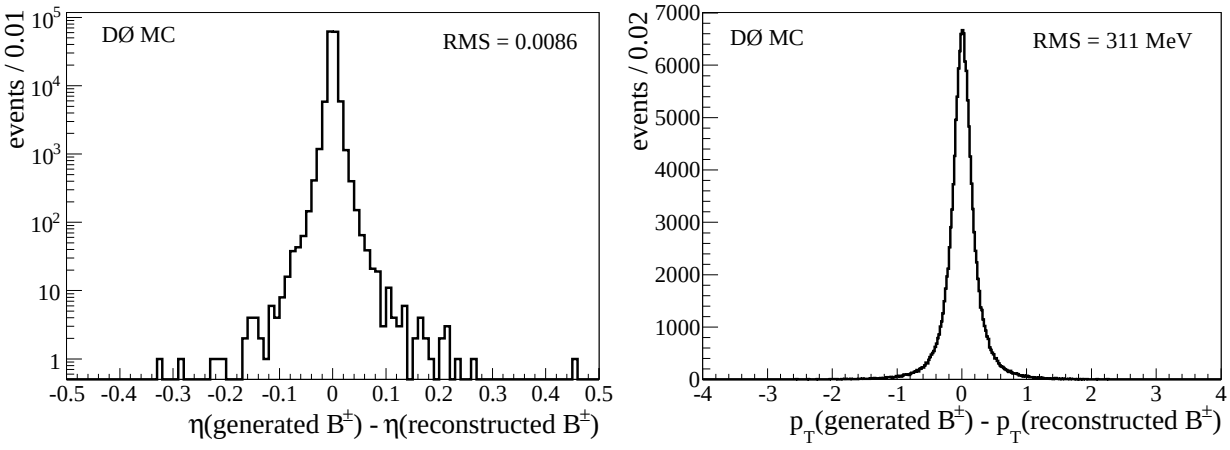

(a) (b)

Figure 6.11 : Distributions of (a) $\eta(\text{generated}B^{\pm})-\eta(\text{reconstructed}B^{\pm})$ and (b) $p_T(\text{generated}B^{\pm})-p_T(\text{reconstructed } B^{\pm})$ in MC@NLO.

Chapter 7

Conclusions

In this analysis we have measured the forward-backward asymmetry in the production of $B^{\pm}$ mesons with $B^{\pm} \to J/\psi K^{\pm}$ decays in $p\bar{p}$ collisions at $\sqrt{s} = 1.96$ TeV. For $B^{\pm}$ mesons with a mean p_T of 12.9 GeV, the result is $A_{\rm FB}(B^{\pm}) = [-0.24 \pm 0.41\,({\rm stat}) \pm 0.19\ ({\rm syst})]\%$, which is the first measurement of this quantity.

Combining the $A_{\rm FB}(B^{\pm})$ data and MC uncertainties in quadrature, our estimate from MC@NLO differs from data by $(2.55 \pm 0.76)\%$, or 3.3 standard deviations. The MC@NLO simulation suggests that $A_{\rm FB}(B^{\pm}) \approx A_{\rm FB}^{b\bar{b}}$, but the measurement of $A_{\rm FB}^{\rm SM}(B^{\pm}) = [2.31 \pm 0.34\,({\rm stat.}) \pm 0.51\,({\rm syst.})]\%$ disagrees with the SM prediction of $A_{\rm FB}^{b\bar{b}}$ in [11] at low $b\bar{b}$ masses. These discrepancies suggest that more rigorous determination of the standard model prediction is needed to interpret our results.

Our data measurement agrees with preliminary results from the CDF collaboration, who are measuring $A_{\rm FB}^{b\bar{b}}$ in the mass range $M(b\bar{b}) > 150$ GeV [47]. Their results are shown in Fig. 7.1 along with SM calculations which are an extension of the values in [11]. All experimental results from the Tevatron show forward-backward asymmetries consistent with zero, and the results from CDF are consistent with the SM predictions, although with large uncertainties. The LHCb collaboration also reports consistency with the SM for their measurement of the $b\bar{b}$ charge asymmetry, or forward-central asymmetry [17].

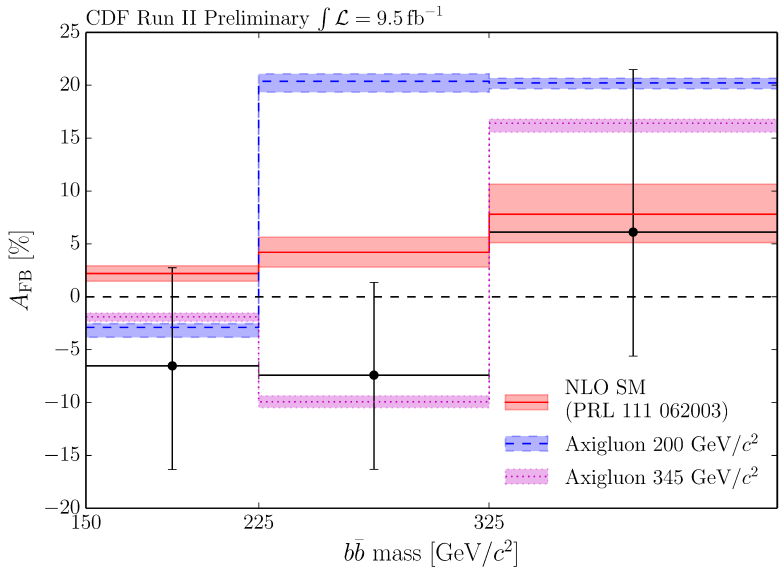

Figure 7.1 : Measurement of $A_{\mathrm{FB}}^{b\bar{b}}$ from the CDF collaboration, along with the SM predictions and two axigluon models. Figure from [47].

The case for new physics creating anomalous forward-backward production asymmetries has steadily weakened. Experimental values of $A_{\mathrm{FB}}^{t\bar{t}}$ decreased and the SM prediction, now known to next-to-next-to-leading-order, has been revised to a larger value. Both our results and the results from CDF suggest that the theory of quantum chromodynamics in the standard model accurately predicts the collision properties which produce $A_{\mathrm{FB}}^{b\bar{b}}$. Due to the limited energy range of the reconstructed $B^{\pm}$ mesons in this data sample we cannot distinguish between the possible new physics models shown in Fig. 1.6, but the precision of this measurement is unique among forward-backward asymmetry measurements and our results for $A_{\mathrm{FB}}(B^{\pm})$ will provide experimental input for constraining new physics models in the future.

References

[1] F. Halzen and A.D. Martin, *Quarks and Leptons: An Introductory Course in Modern Particle Physics*, John Wiley & Sons, Inc. (1984).

[2] E. Siegel, "How the Higgs gives Mass to the Universe", 2012, `http://scienceblogs.com/startswithabang/2012/07/04/how-the-higgs-gives-mass-to-the-universe/`

[3] K.A. Olive *et al.* (Particle Data Group), Chin. Phys. C **38**, 090001 (2014).

[4] V.M. Abazov *et al.* (D0 Collaboration), arXiv:1408.5016 (2014) (submitted to Phys. Rev. Lett.).

[5] G. Aad *et al.* (Atlas Collaboration), Phys. Lett. B **716**, 1 (2012); S. Chatrchyan *et al.* (CMS Collaboration), Phys. Lett. B **716**, 30 (2012);

[6] R.D. Field, Phys. Rev. D **65**, 094006 (2002).

[7] L.G. Almeida, G. Sterman, and W. Vogelsang, Phys. Rev. D **78**, 014008 (2008); J.H. Kühn and G. Rodrigo, J. High Energy Phys. 01 (2012) 063; J.A. Aguilar-Saavedra, D. Amidei, A. Juste, and M. Perez-Victoria, arXiv:1406.1798.

[8] V.M. Abazov *et al.* (D0 Collaboration), Phys. Rev. D **84**, 112005 (2011).

[9] T. Aaltonen *et al.* (CDF Collaboration), Phys. Rev. D **83**, 112003 (2011); Phys. Rev. D **87**, 092002 (2013); Phys. Rev. D **88**, 072003 (2013).

[10] M.I. Gresham, I.-W. Kim, and K.M. Zurek, Phys. Rev. D **83**, 114027 (2011); J.A. Aguilar-Saavedra and M. Perez-Victoria, J. High Energy Phys. 09 (2011) 097; J.F. Kamenik, J. Shu, and J. Zupan, Eur. Phys. J. C **72**, 2102 (2012).

[11] B. Grinstein and C.W. Murphy, Phys. Rev. Lett. **111**, 062003 (2013); Phys. Rev. Lett. **112**, 239901 (2014).

[12] S. Ipek, Phys. Rev. D **87**, 116010 (2013).

[13] V. M Abazov *et al.* (D0 Collaboration), Phys. Rev. D **87**, 011103(R) (2013); Phys. Rev. D **88**, 112002 (2013); Phys. Rev. D **90**, 072001 (2014); arXiv:1405.0421 (2014) (to appear in Phys. Rev. D).

[14] W. Bernreuther and Z.-G. Si, Phys. Rev. D **86**, 034026 (2012).

[15] S. Chatrchyan *et al.* (CMS Collaboration), J. High Energy Phys. 04 (2014) 191.

[16] G. Aad *et al.* (ATLAS Collaboration), J. High Energy Phys. 02 (2014) 107.

[17] R. Aaij *et al.* (LHCb Collaboration), Phys. Rev. Lett. **113**, 082003 (2014).

[18] J.H. Kühn and G. Rodrigo, Phys. Rev. D **59**, 054017 (1999).

[19] A.V. Manohar and M. Trott, Phys. Lett. B **711**, 313 (2012).

[20] S. Frixione and B.R. Webber, J. High Energy Phys. 06 (2002) 029; S. Frixione, P. Nason, and B.R. Webber, J. High Energy Phys. 08 (2003) 007.

[21] J. Pumplin, D.R. Stump, J. Huston, H.-L. Lai, P. Nadolsky, and W.-K. Tung, J. High Energy Phys. 07 (2002) 012; D. Stump, J. Huston, J. Pumplin, W.-K. Tung, H.-L. Lai, S. Kuhlmann, and J. Francis Owens, J. High Energy Phys. 10 (2003) 046.

[22] G. Corcella *et al.*, J. High Energy Phys. 01 (2001) 010.

[23] R. Brun and F. Carminati, CERN Program Library Writeup W5013, 1993. We use GEANT version 3.15.

[24] Fermilab Web Page, "Science: Neutrinos", `http://www.fnal.gov/pub/science/particle-physics/experiments/neutrinos.html`.

[25] Fermilab Web Page, "Science: Muons", `http://www.fnal.gov/pub/science/particle-physics/experiments/muons.html`.

[26] Fermilab Accelerator Division, "Concepts Rookie Book" (2010). `http://www-bdnew.fnal.gov/operations/rookie\_books/rbooks.html`.

[27] B. Casey *et al*, Nucl. Instrum. Methods A **698**, 208 (2013).

[28] S. Abachi *et al.* (D0 Collaboration), Phys. Rev. Lett. **74**, 2632 (1995); F. Abe *et al.* (CDF Collaboration), Phys. Rev. Lett. **74**, 2626 (1995).

[29] B. Abbott *et al.* (D0 Collaboration), Phys. Rev. D **58**, 092003 (1998); V.M. Abazov *et al.* (D0 Collaboration), Phys. Rev. D **89**, 012005 (2014).

[30] V.M. Abazov *et al.* (D0 Collaboration), Nucl. Instrum. Methods A **565**, 463 (2006).

[31] S.N. Ahmed *et al.*, Nucl. Instrum. Methods A **634**, 8 (2011).

[32] R. Angstat *et al.* (D0 Collaboration), Nucl. Instrum. Methods A **622**, 298 (2010).

[33] V.M. Abazov *et al.*, Nucl. Instrum. Methods A **552**, 372 (2005); V.M. Abazov *et al.* (D0 Collaboration), Nucl. Instrum. Methods A **737**, 281 (2014).

[34] M. Williams, "Observations and Measurements of $L = 1$ Orbitally Excited B Mesons at the DØ Experiment", Doctoral Thesis, Lancaster University (2008).

[35] M. Aoki, "Search for the rare decay $B_s^0 \to \mu^+\mu^-$ using 6 fb^{-1} of DØ RunII data", Internal Note 6048, DØ Collaboration (2010).

[36] I. Antcheva *et al.*, Computer Physics Communications **180** 2499 (2009).

[37] V.M. Abazov *et al.* (D0 Collaboration), Phys. Rev. Lett. **110**, 241801 (2013).

[38] A. Hoecker *et al.*, "Toolkit for multivariate data analysis", *Proc. Sci.* ACAT (2007) 040. We use version 4.1.0.

[39] T. Sjöstrand, S. Mrenna, and P. Skands, J. High Energy Phys. 05 (2006) 026.

[40] V.M. Abazov *et al.* (D0 Collaboration), Phys. Rev. D **82**, 032001 (2010).

[41] J. Beringer *et al.* (Particle Data Group), "Dalitz Plot Analysis Formalism", Phys. Rev. D **86**, 010001 (2012).

[42] V.M. Abazov *et al.* (D0 Collaboration), Phys. Rev. D **86**, 072009 (2012);

[43] S. Frixione (private communication).

[44] J.M. Campbell and R.K. Ellis, FERMILAB-PUB-12-078-T, arXiv:1204.1513 (2012).

[45] S. Frixione, "MC@NLO: a tutorial". Talk presented at: Les Houches 2005(SM: EW, QCD, and Higgs), June 2005. `http://indico.cern.ch/event/a052819/session/s2/contribution/s2t1/material/0/0.pdf`, page 15.

[46] G. Corcella and V. Drollinger, Nucl. Phys. B **730**, 82 (2005).

[47] CDF Collaboration, CDF/ANAL/TOP/PUB/11092 (2014).

Appendix A

BDT Variables

The following figures compare sideband-subtracted data (blue triangles) and MC (red squares) from the "peak" mass range of Fig. 3.4. These distributions should agree well after the MC reweighting, and are also contrasted to the distributions of background range data (black dots). The variables are ordered by their importance to the BDT.

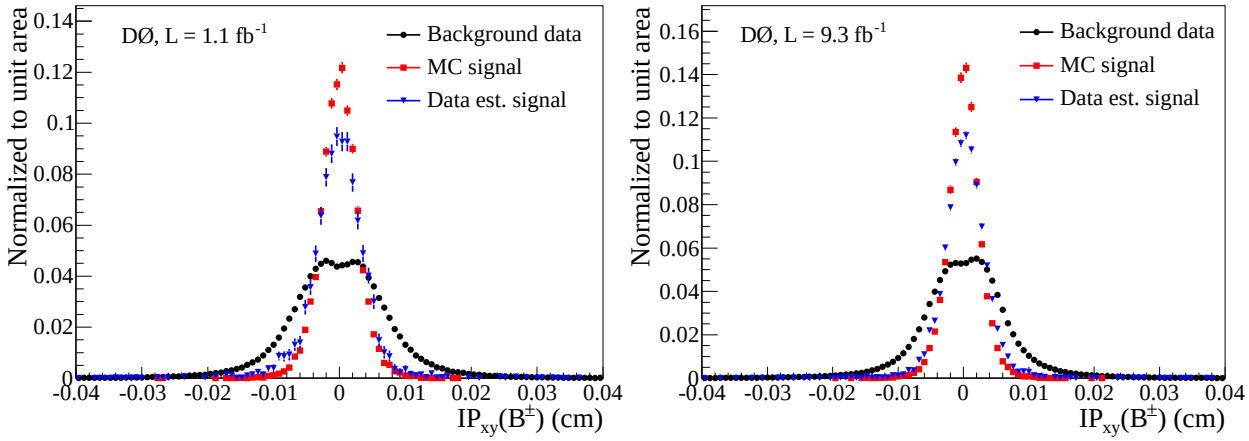

(a) (b)

Figure A.1 : Distributions of $B^{\pm}$ transverse IP in (a) Run IIa and (b) Run IIb.

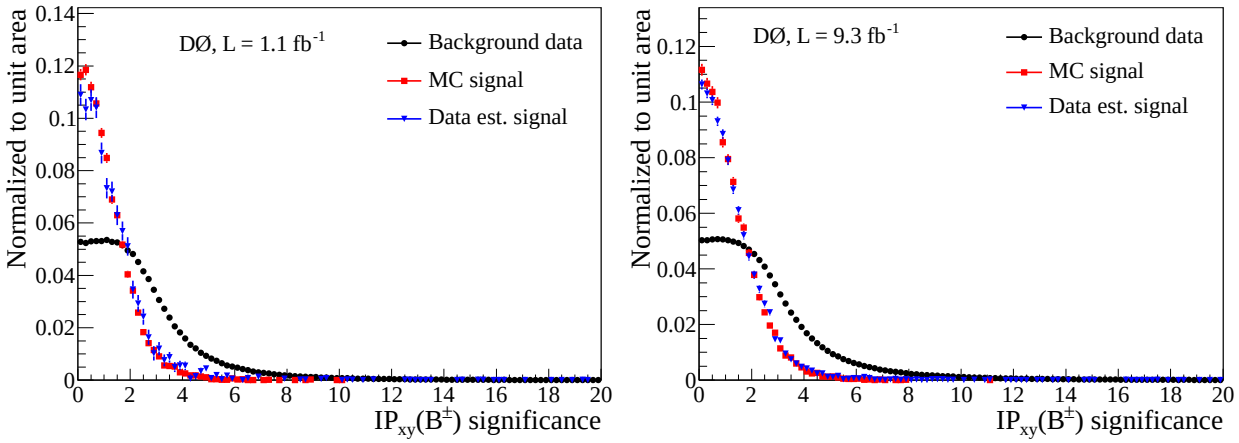

(a) (b)

Figure A.2 : Distributions of $B^{\pm}$ transverse IP significance in (a) Run IIa and (b) Run IIb.

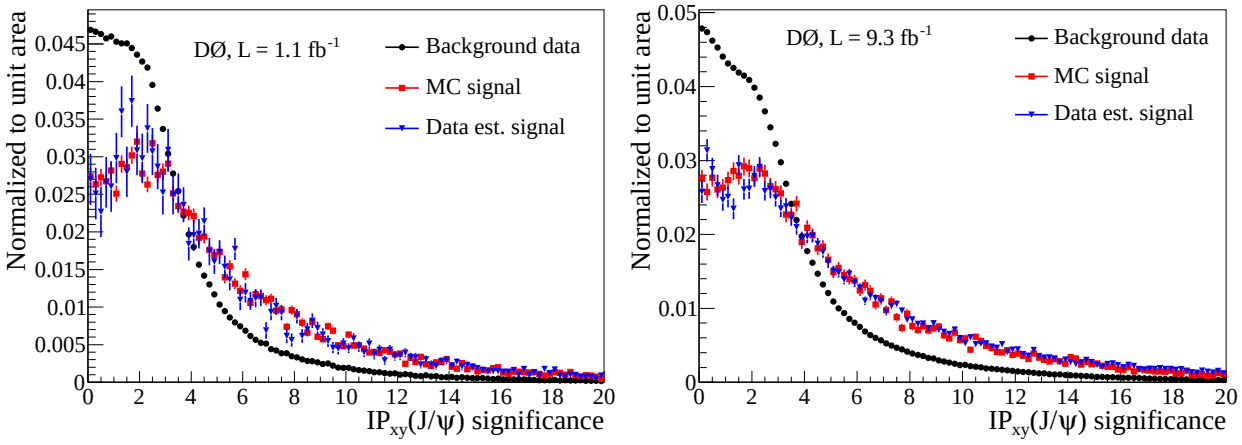

(a) (b)

Figure A.3 : Distributions of J/ψ transverse IP significance in (a) Run IIa and (b) Run IIb.

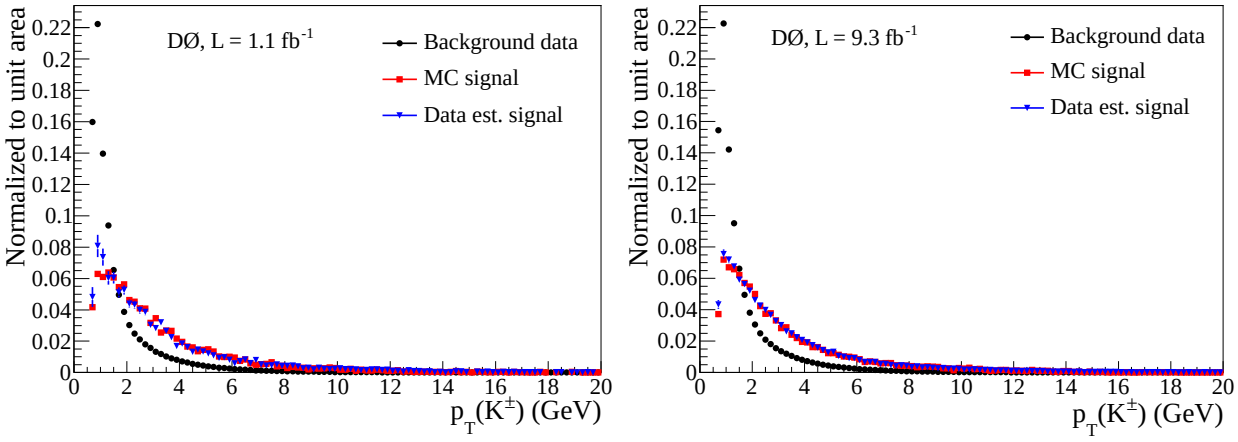

(a) (b)

Figure A.4 : Distributions of $p_T(K^{\pm})$ in (a) Run IIa and (b) Run IIb.

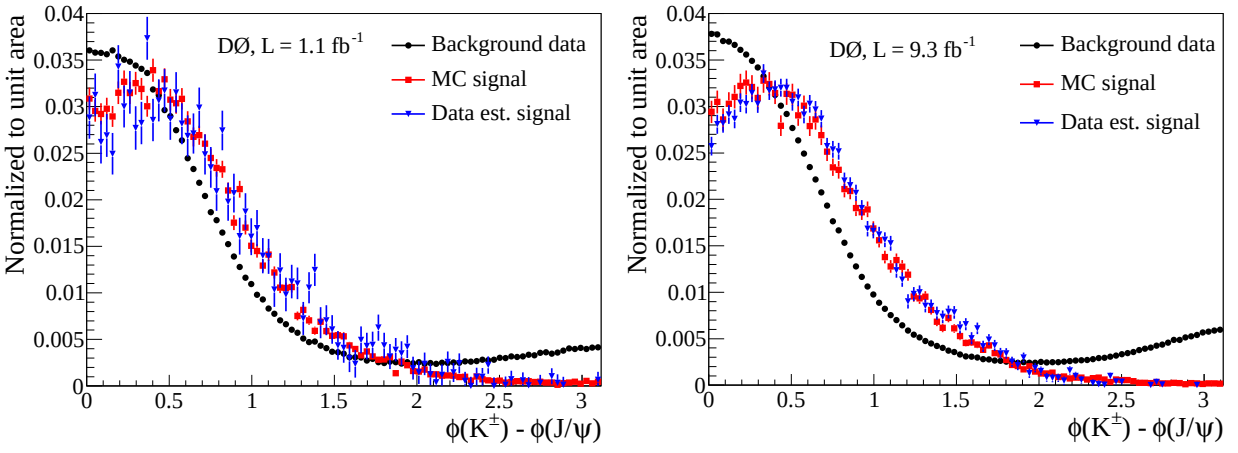

(a) (b)

Figure A.5 : Distributions of $\phi_{K^{\pm}} - \phi_{J/\psi}$ in (a) Run IIa and (b) Run IIb.

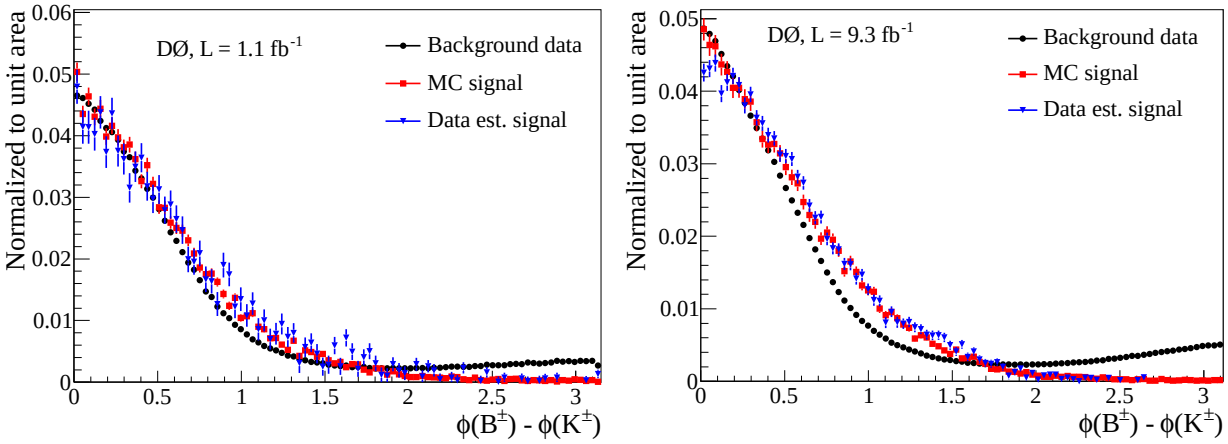

(a) (b)

Figure A.6 : Distributions of $\phi_{B^\pm} - \phi_{K^\pm}$ in (a) Run IIa and (b) Run IIb.

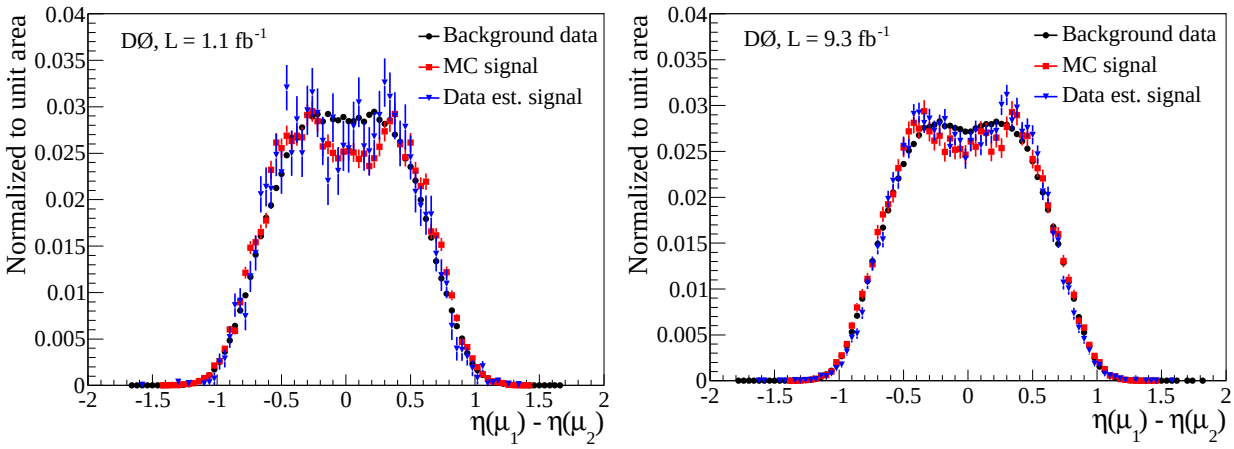

(a) (b)

Figure A.7 : Distributions of $\eta_{\mu_1} - \eta_{\mu_2}$ in (a) Run IIa and (b) Run IIb.

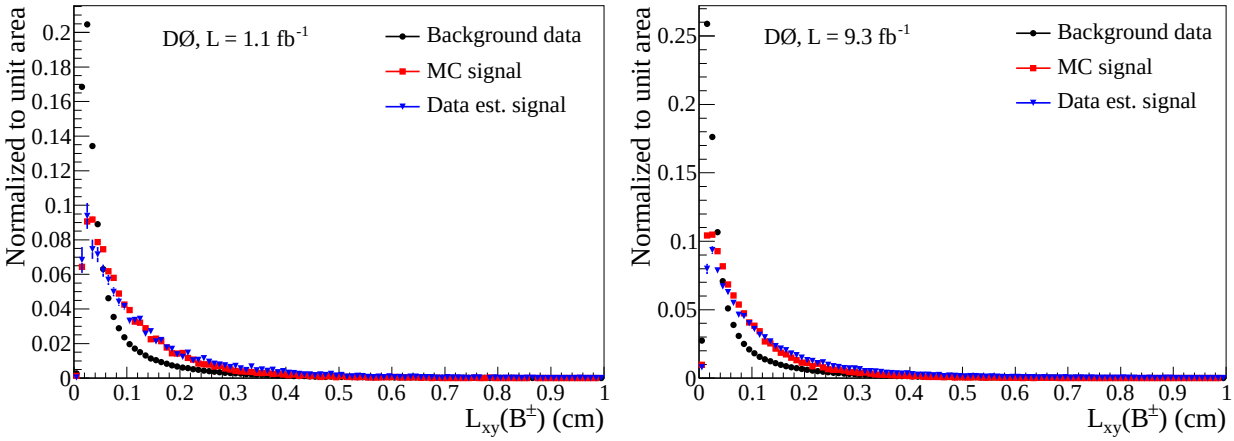

(a) (b)

Figure A.8 : Distributions of $L_{xy}(B^{\pm})$ in (a) Run IIa and (b) Run IIb.

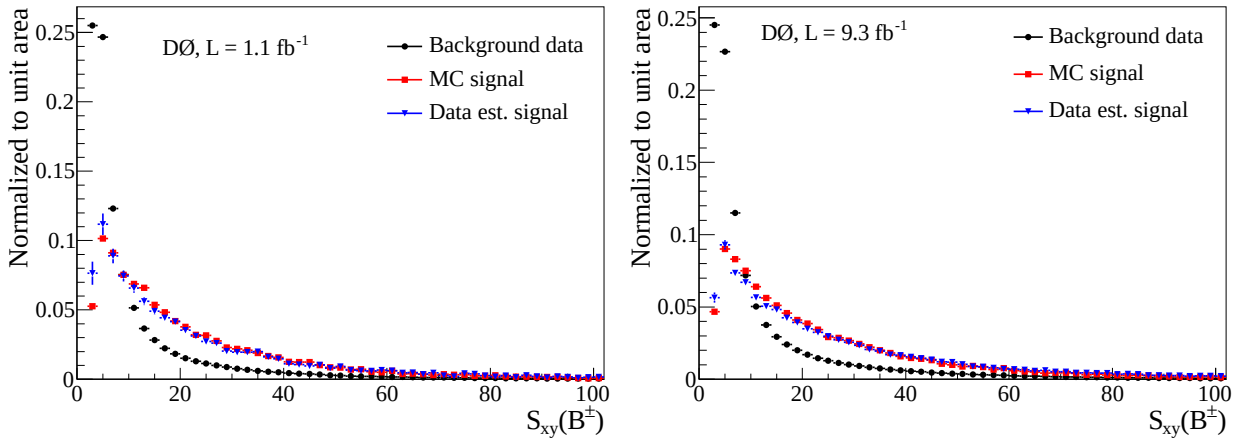

(a) (b)

Figure A.9 : Distributions of $\mathcal{S}_{xy}(B^{\pm})$ in (a) Run IIa and (b) Run IIb.

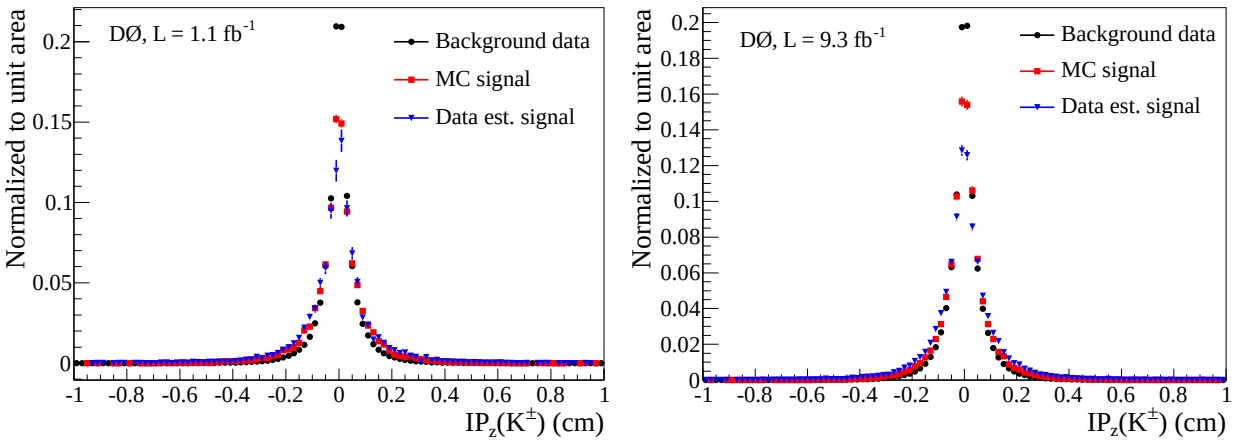

(a) (b)

Figure A.10 : Distributions of $K^{\pm}$ longitudinal IP in (a) Run IIa and (b) Run IIb.

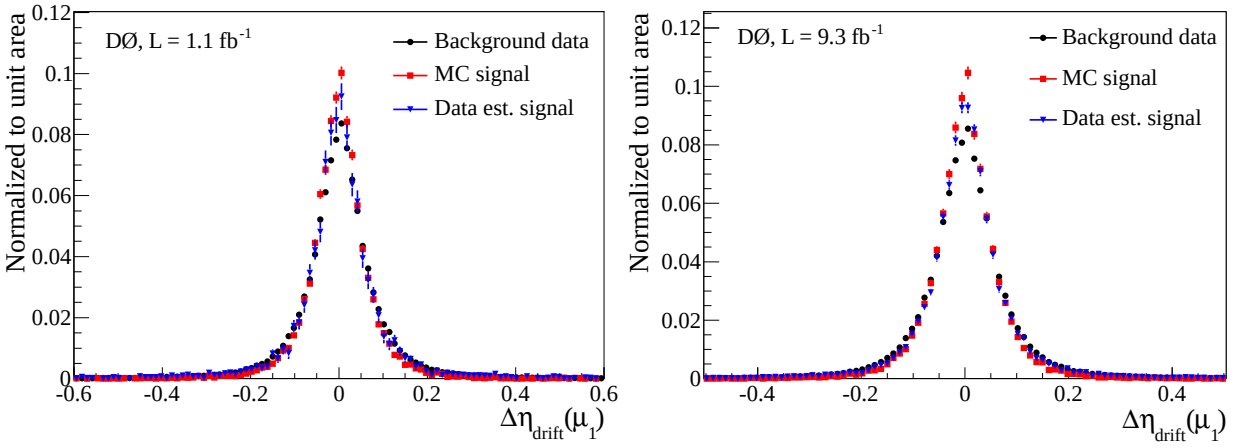

(a) (b)

Figure A.11 : Distributions of $\Delta\eta(\mu_1)$ (central tracker to muon system) in (a) Run IIa and (b) Run IIb.

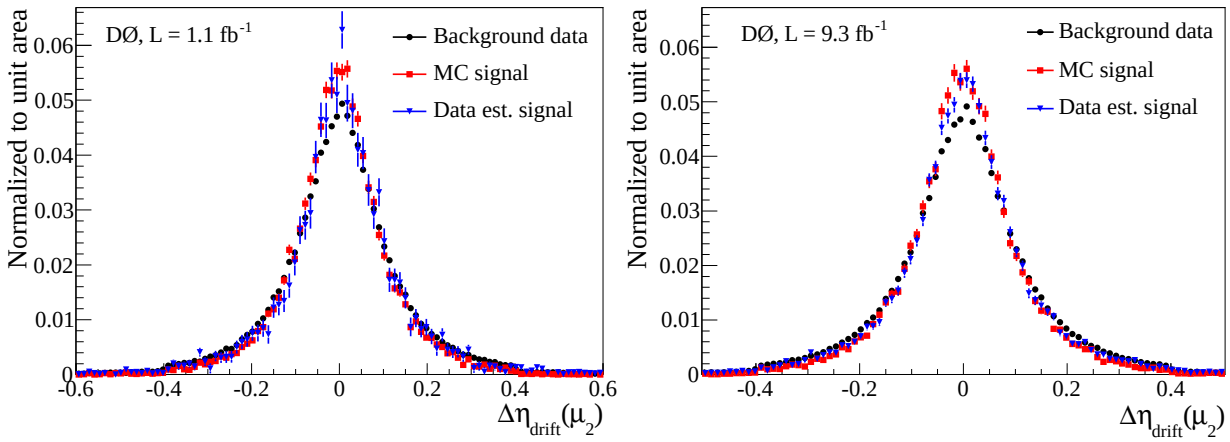

(a) (b)

Figure A.12 : Distributions of $\Delta\eta(\mu_2)$ (central tracker to muon system) in (a) Run IIa and (b) Run IIb.

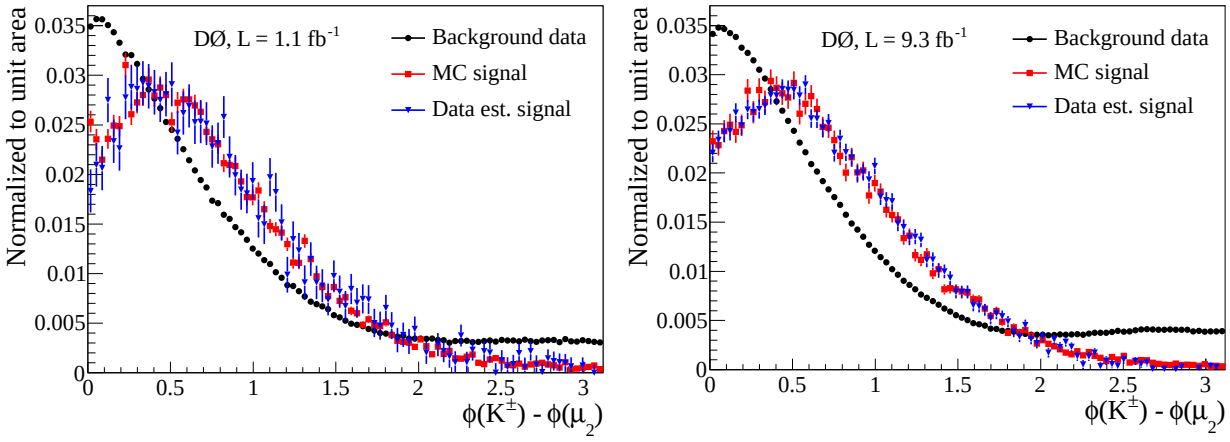

(a) (b)

Figure A.13 : Distributions of $\phi_{K^\pm} - \phi_{\mu_2}$ in (a) Run IIa and (b) Run IIb.

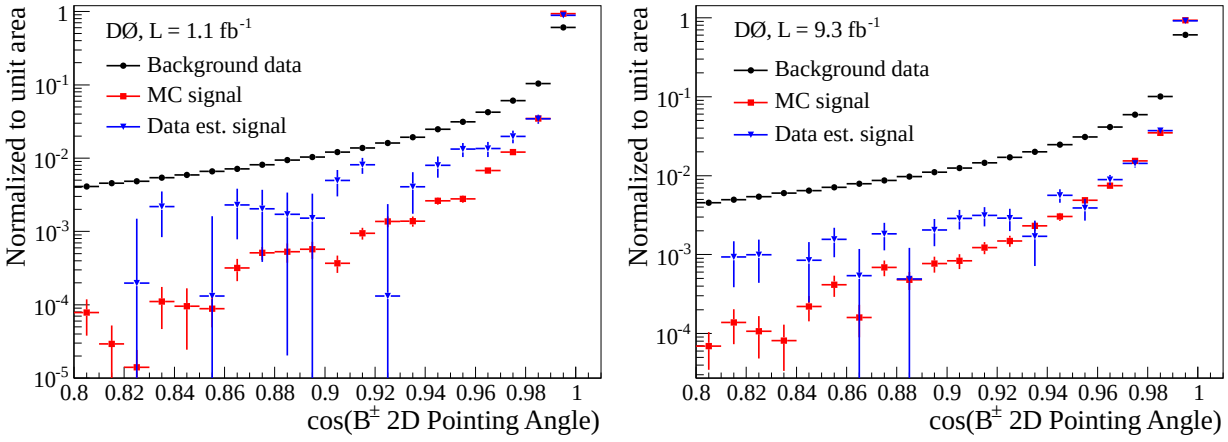

(a) (b)

Figure A.14 : Distributions of cos($B^{\pm}$ 2D Pointing Angle) in (a) Run IIa and (b) Run IIb.

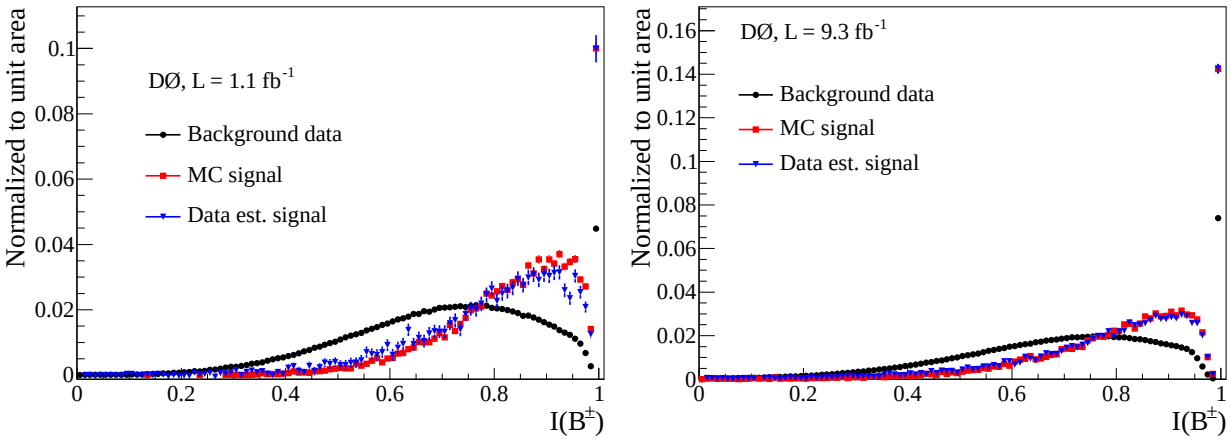

(a) (b)

Figure A.15 : Distributions of $\mathcal{I}(B^{\pm})$ in (a) Run IIa and (b) Run IIb.

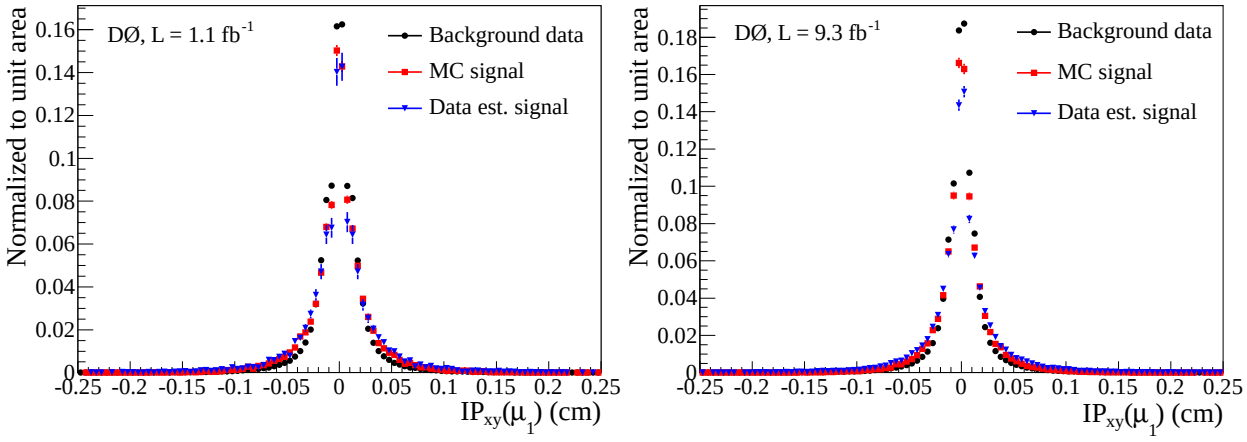

(a) (b)

Figure A.16 : Distributions of μ_1 transverse IP in (a) Run IIa and (b) Run IIb.

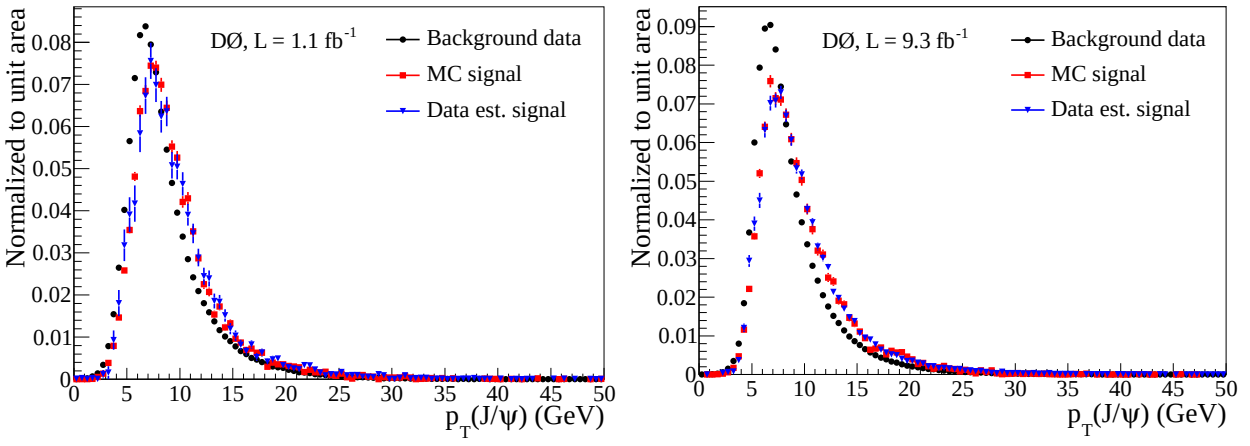

(a) (b)

Figure A.17 : Distributions of $p_T(J/\psi)$ in (a) Run IIa and (b) Run IIb.

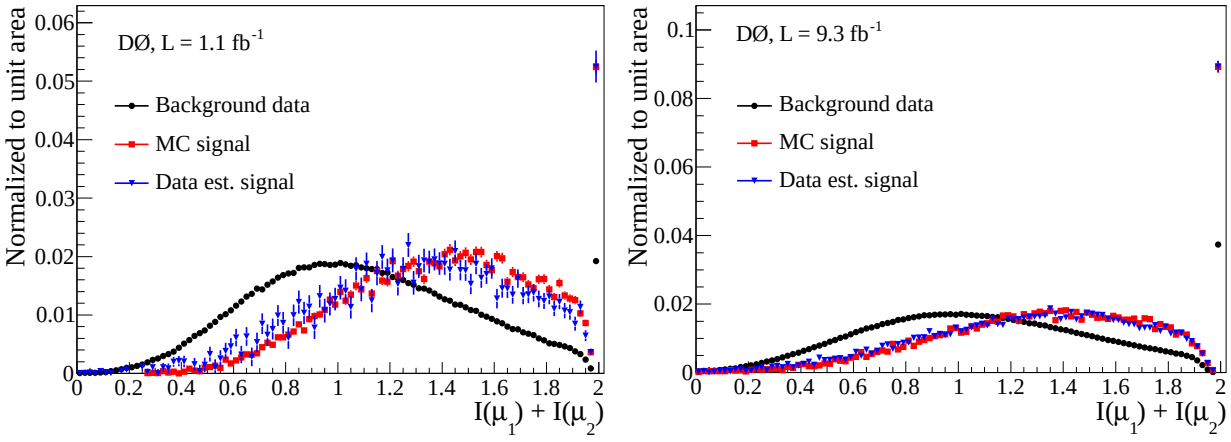

(a) (b)

Figure A.18 : Distributions of $\mathcal{I}(\mu_1) + \mathcal{I}(\mu_2)$ in (a) Run IIa and (b) Run IIb.

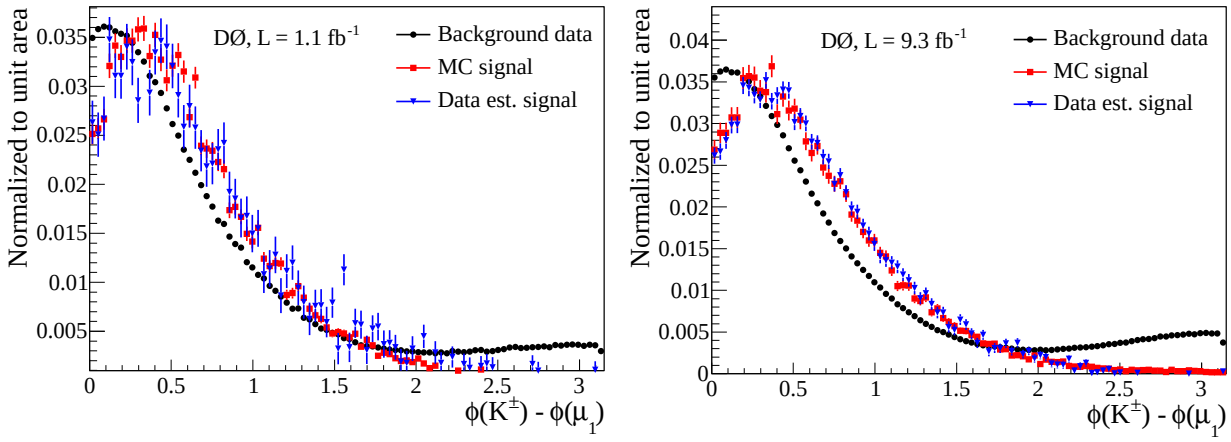

(a) (b)

Figure A.19 : Distributions of $\phi_{K^\pm} - \phi_{\mu_1}$ in (a) Run IIa and (b) Run IIb.

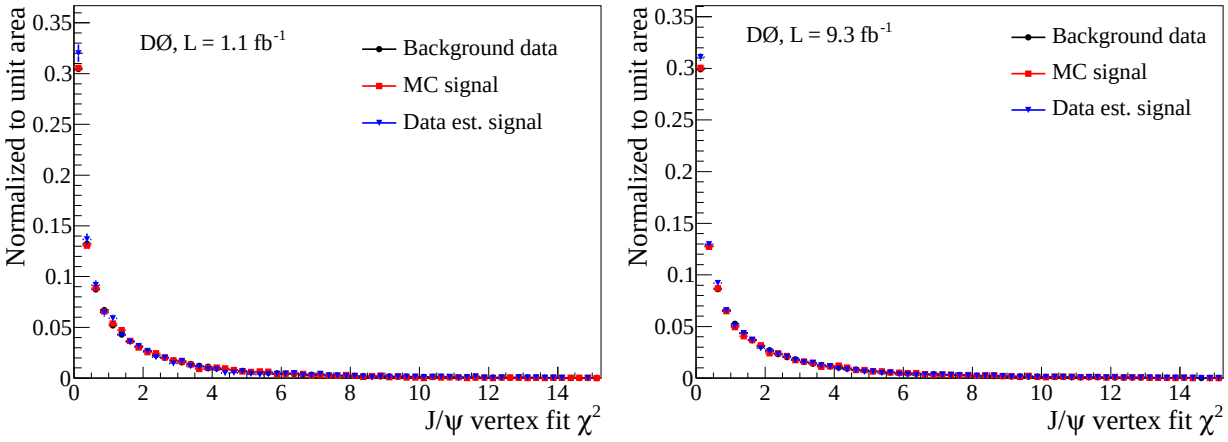

(a) (b)

Figure A.20 : Distributions of J/ψ vertex χ^2 in (a) Run IIa and (b) Run IIb.

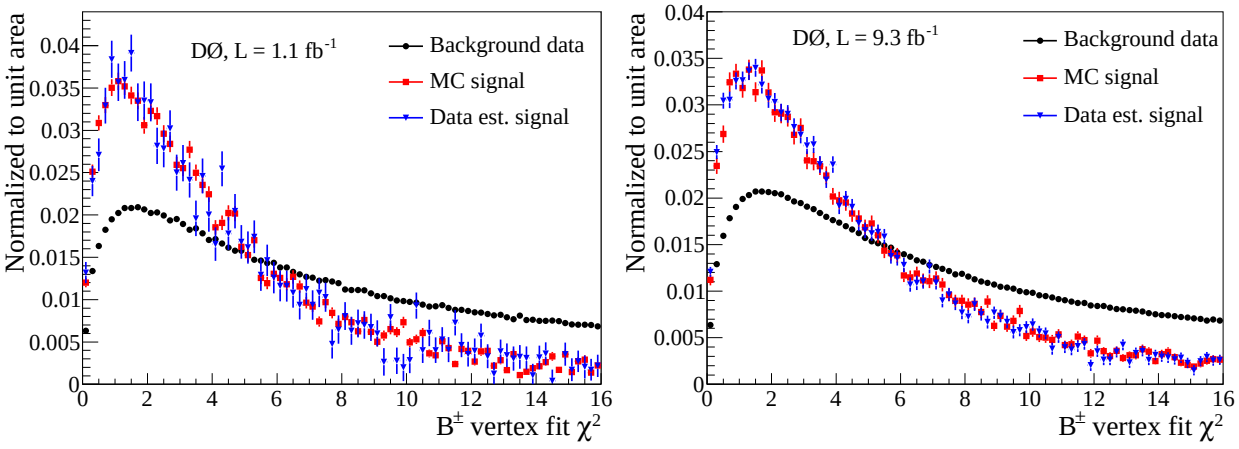

(a) (b)

Figure A.21 : Distributions of $B^{\pm}$ vertex χ^2 in (a) Run IIa and (b) Run IIb.

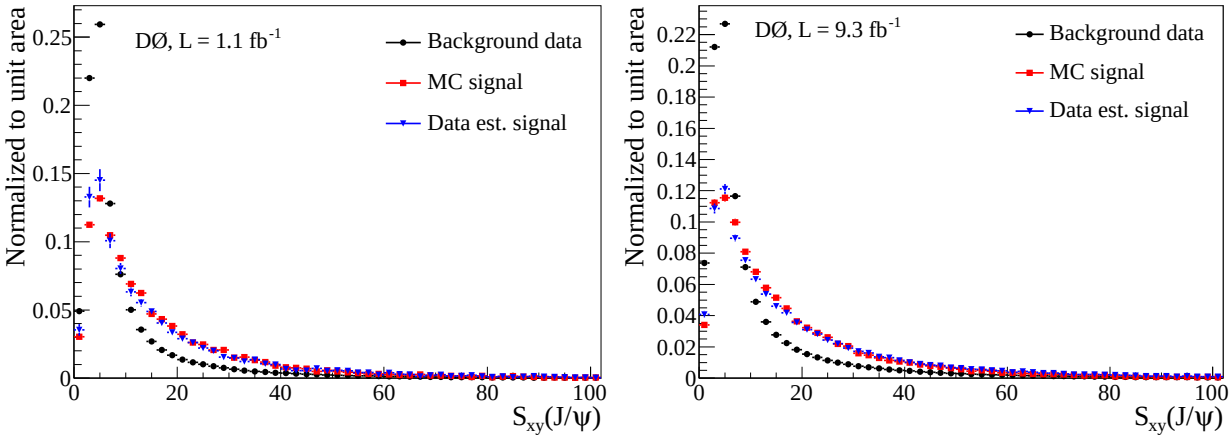

(a) (b)

Figure A.22 : Distributions of $\mathcal{S}_{xy}(J/\psi)$ in (a) Run IIa and (b) Run IIb.

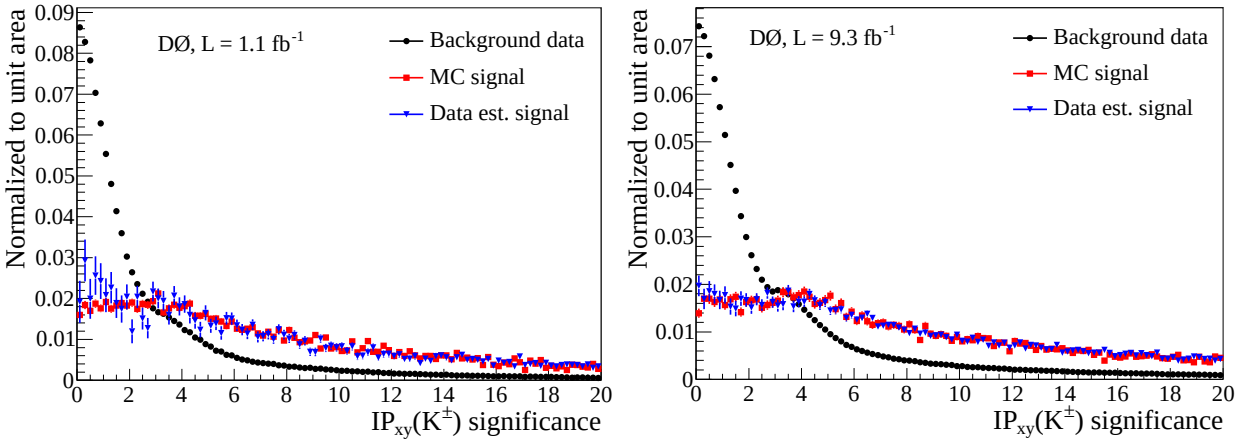

(a) (b)

Figure A.23 : Distributions of $K^{\pm}$ transverse IP significance in (a) Run IIa and (b) Run IIb.

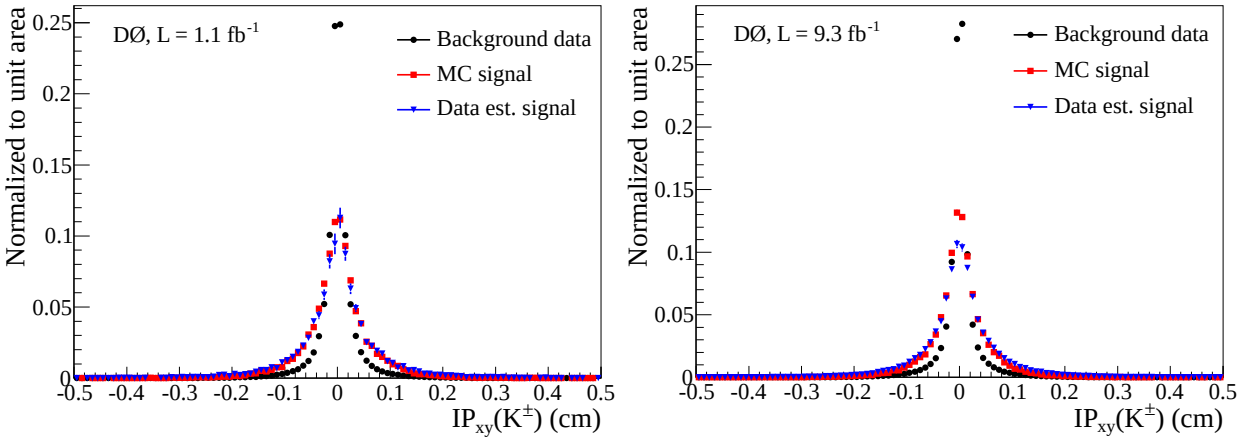

(a) (b)

Figure A.24 : Distributions of $K^{\pm}$ transverse IP in (a) Run IIa and (b) Run IIb.

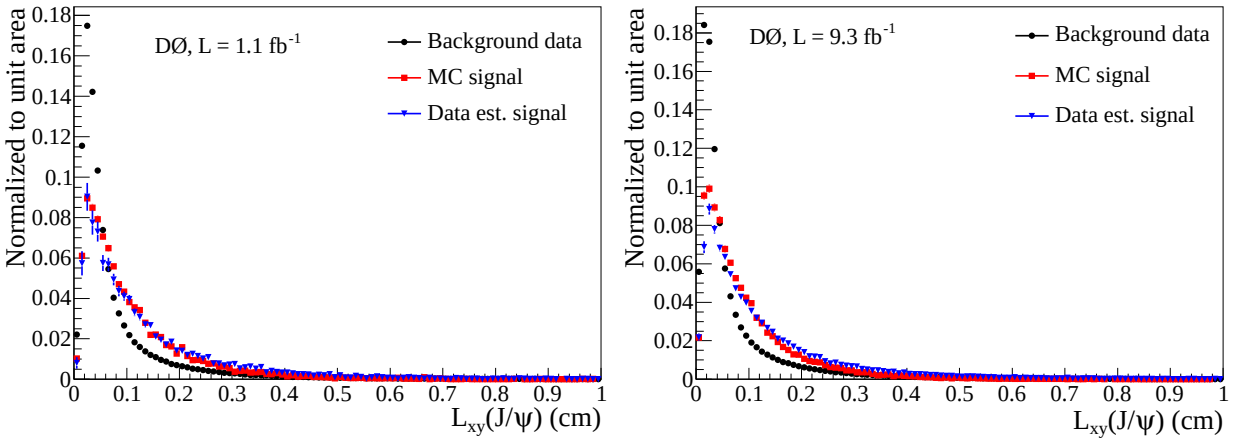

(a) (b)

Figure A.25 : Distributions of $L_{xy}(J/\psi)$ in (a) Run IIa and (b) Run IIb.

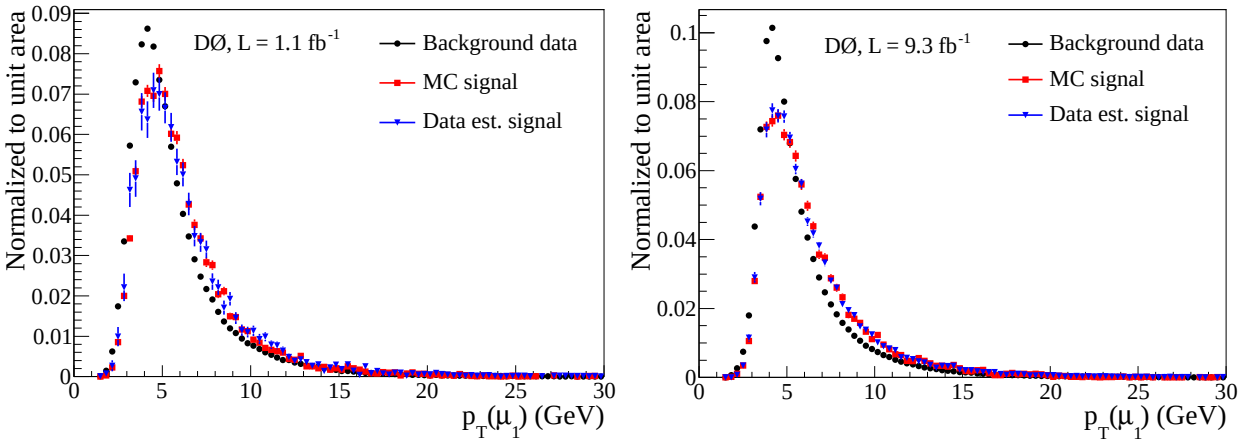

(a) (b)

Figure A.26 : Distributions of $p_T(\mu_1)$ in (a) Run IIa and (b) Run IIb.

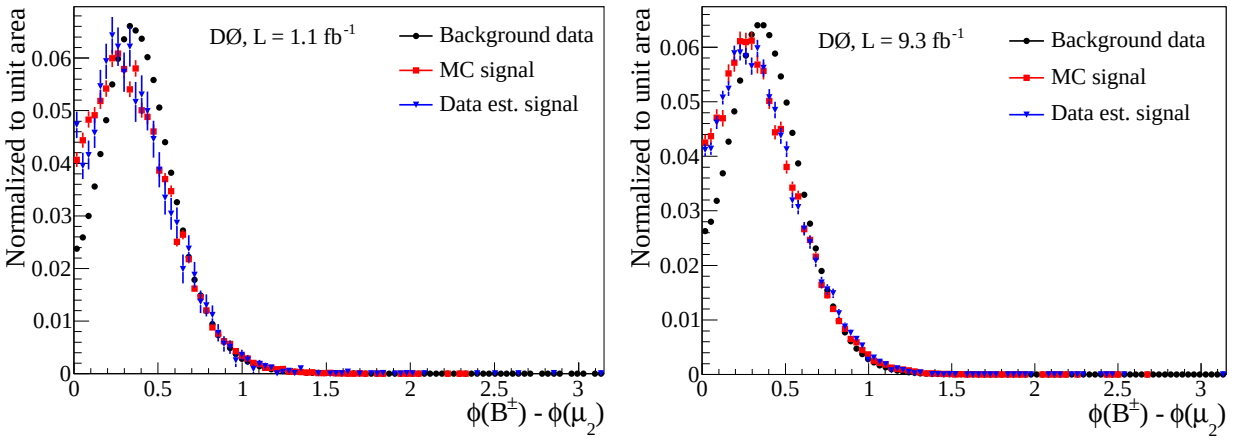

(a) (b)

Figure A.27 : Distributions of $\phi_{B^\pm} - \phi_{\mu_2}$ in (a) Run IIa and (b) Run IIb.

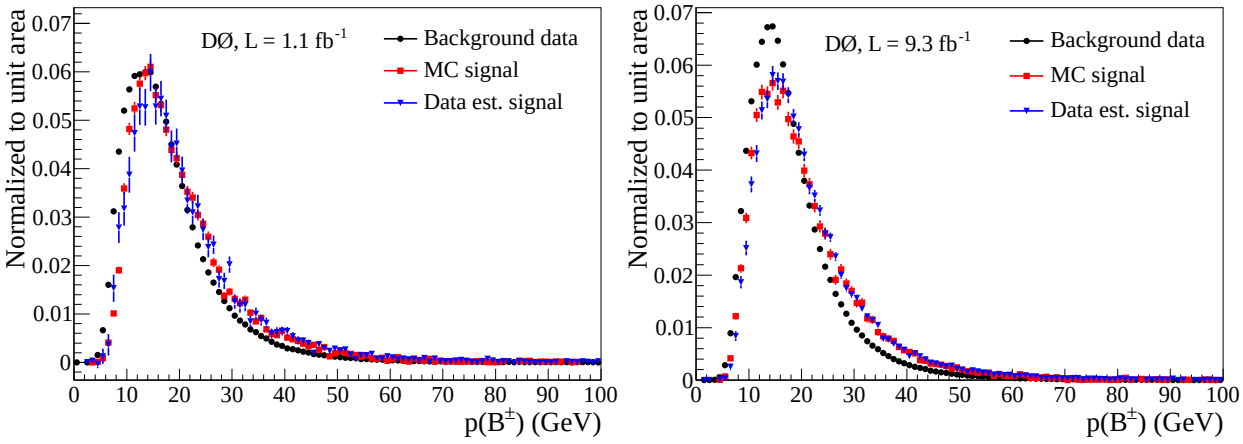

(a) (b)

Figure A.28 : Distributions of $p(B^{\pm})$ in (a) Run IIa and (b) Run IIb.

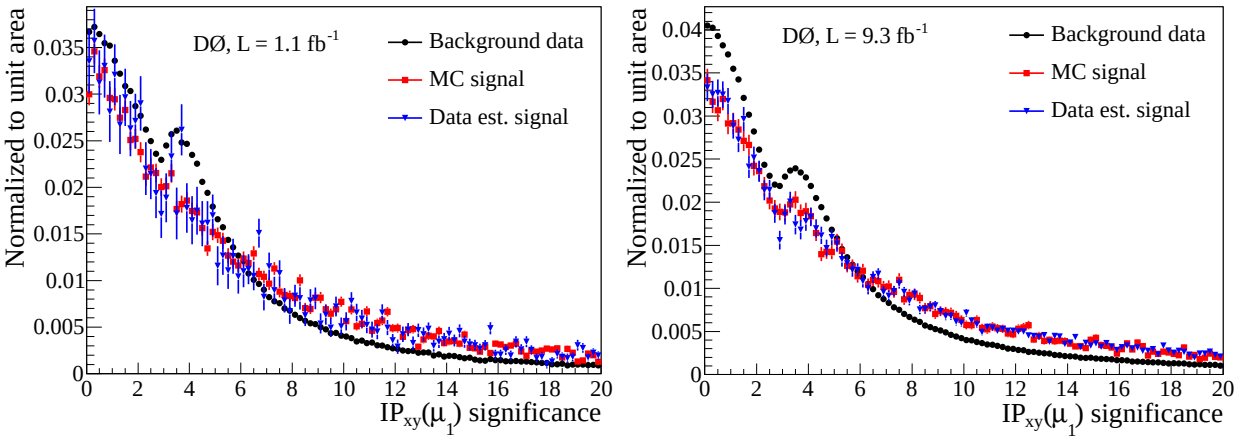

(a) (b)

Figure A.29 : Distributions of μ_1 transverse IP significance in (a) Run IIa and (b) Run IIb.

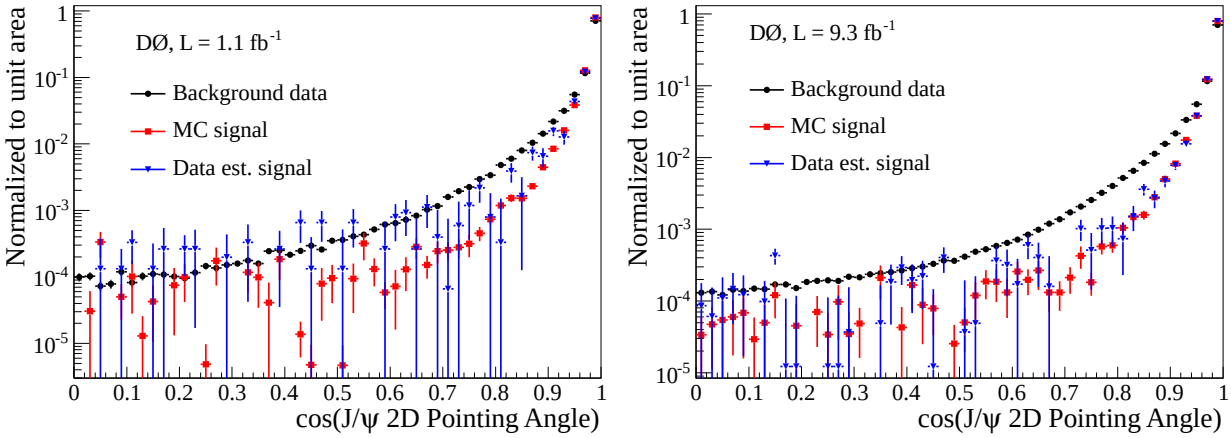

(a) (b)

Figure A.30 : Distributions of cos(J/ψ 2D Pointing Angle) in (a) Run IIa and (b) Run IIb.

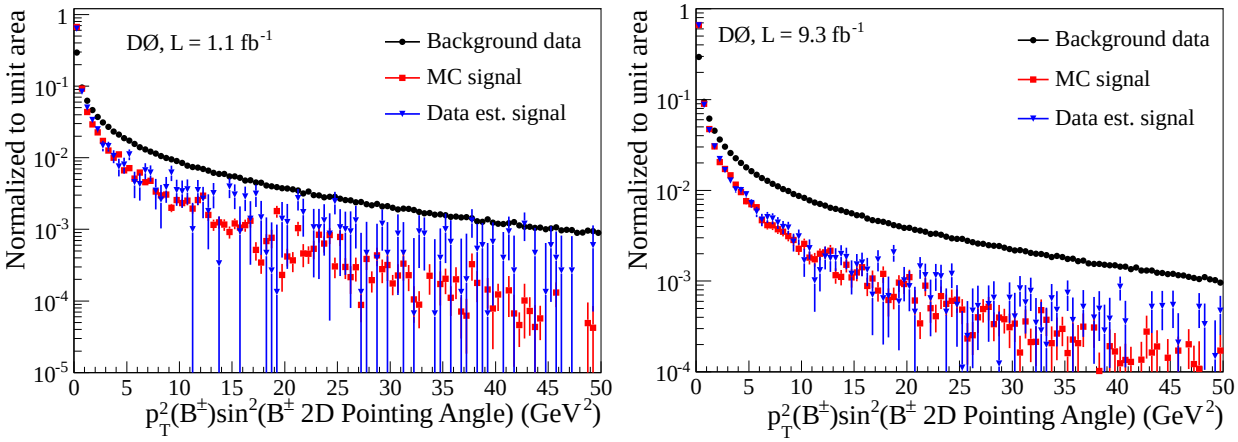

(a) (b)

Figure A.31 : Distributions of $p_T^2 \sin^2(B^{\pm}$ 2D Pointing Angle) in (a) Run IIa and (b) Run IIb.

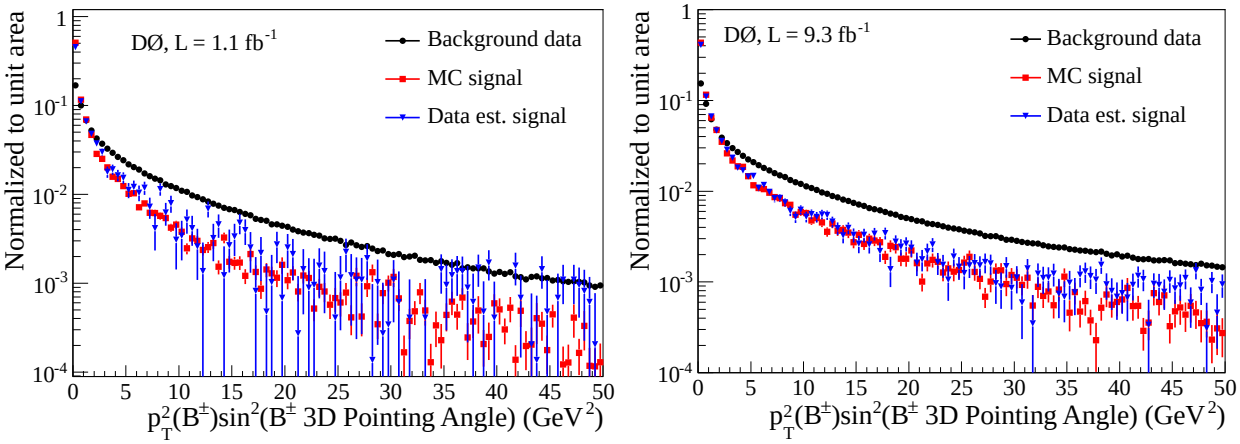

(a) (b)

Figure A.32 : Distributions of $p_T^2 \sin^2(B^{\pm}$ 3D Pointing Angle) in (a) Run IIa and (b) Run IIb.

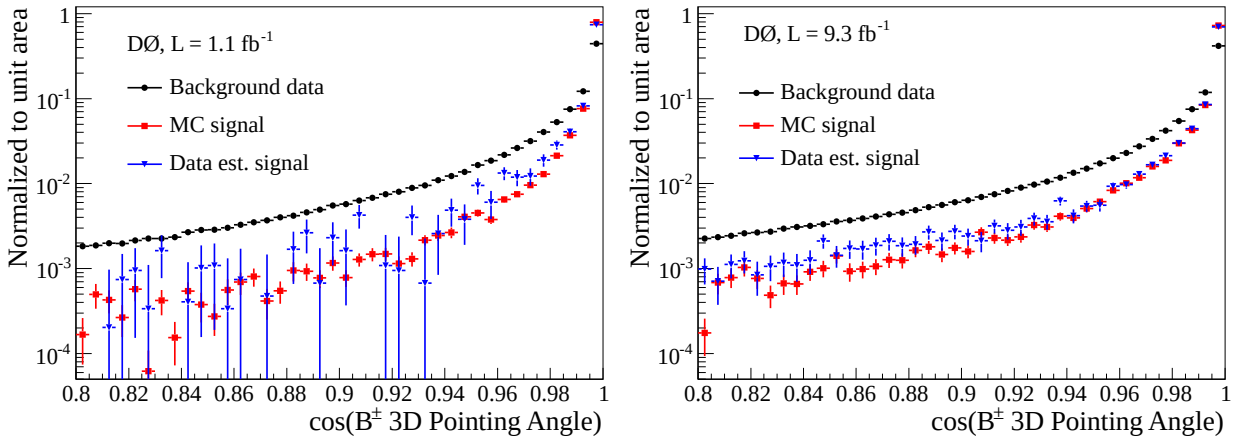

(a) (b)

Figure A.33 : Distributions of $\cos(B^{\pm}$ 3D Pointing Angle) in (a) Run IIa and (b) Run IIb.

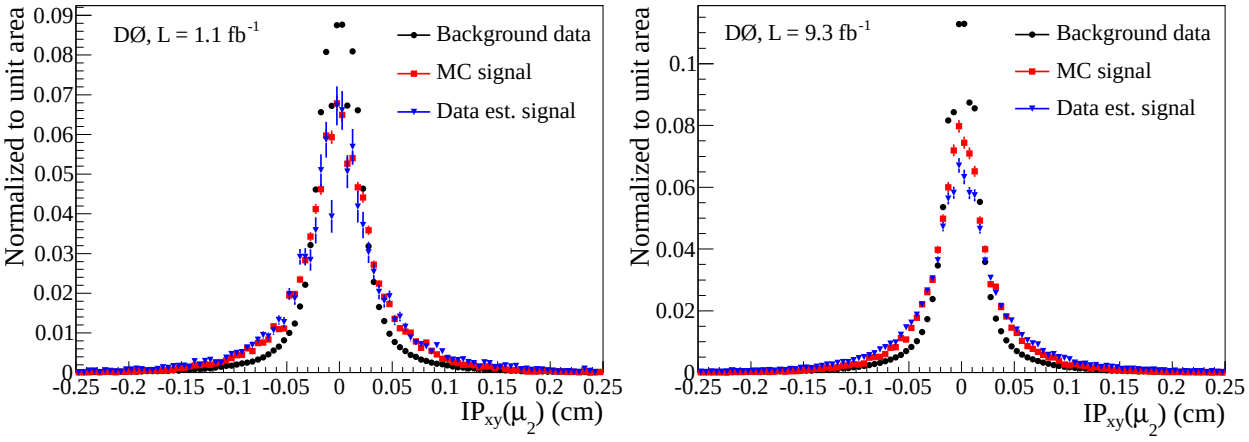

(a) (b)

Figure A.34 : Distributions of μ_2 transverse IP in (a) Run IIa and (b) Run IIb.

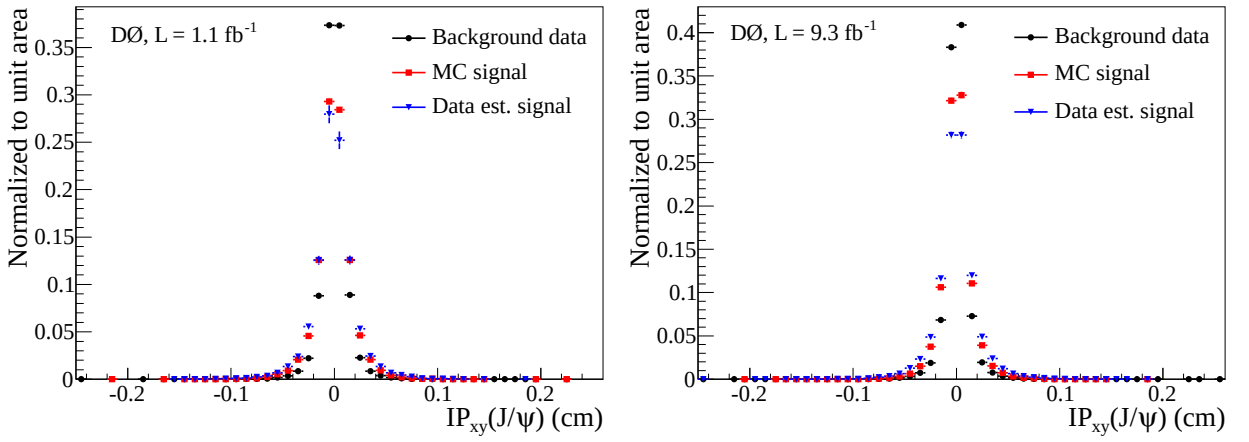

(a) (b)

Figure A.35 : Distributions of J/ψ transverse IP in (a) Run IIa and (b) Run IIb.

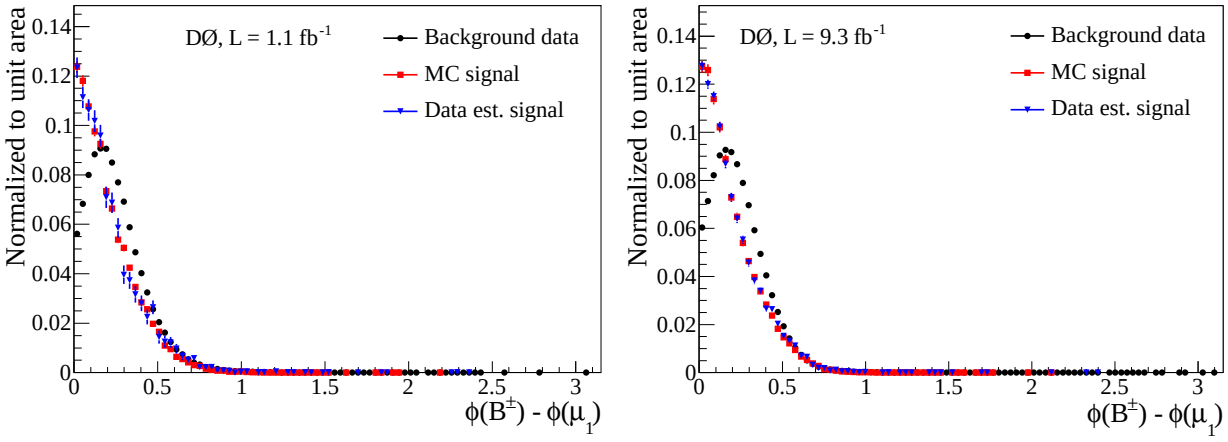

(a) (b)

Figure A.36 : Distributions of $\phi_{B^\pm} - \phi_{\mu_1}$ in (a) Run IIa and (b) Run IIb.

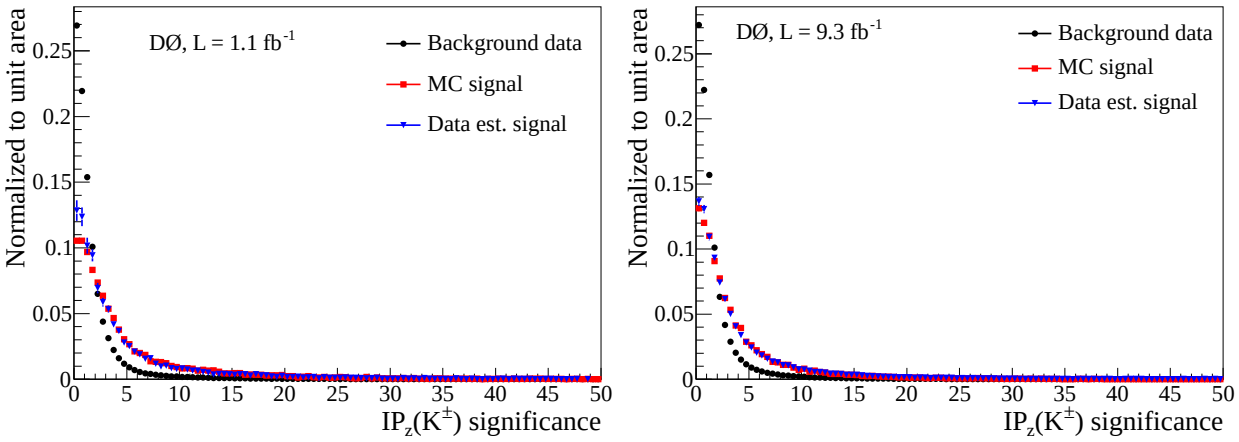

(a) (b)

Figure A.37 : Distributions of $K^\pm$ longitudinal IP significance in (a) Run IIa and (b) Run IIb.

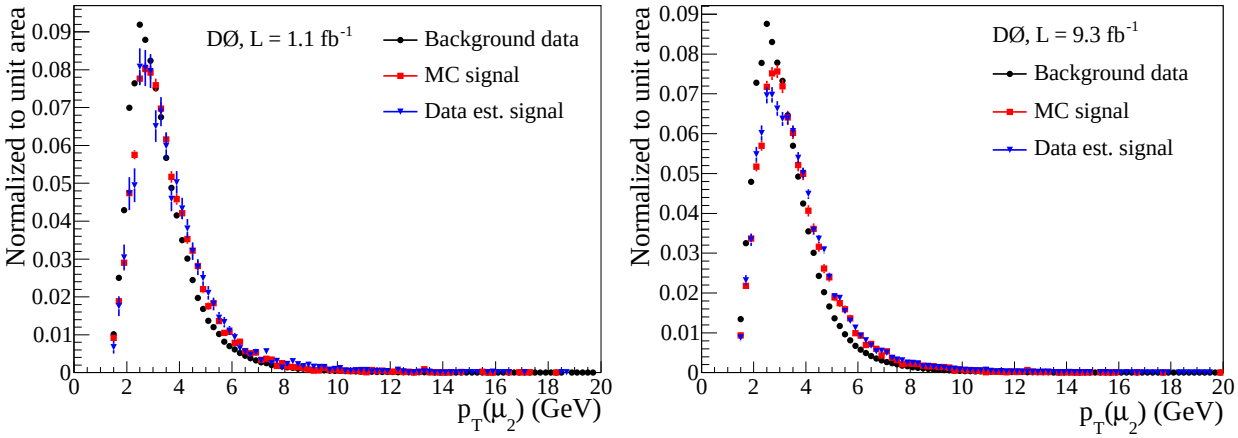

(a) (b)

Figure A.38 : Distributions of $p_T(\mu_2)$ in (a) Run IIa and (b) Run IIb.

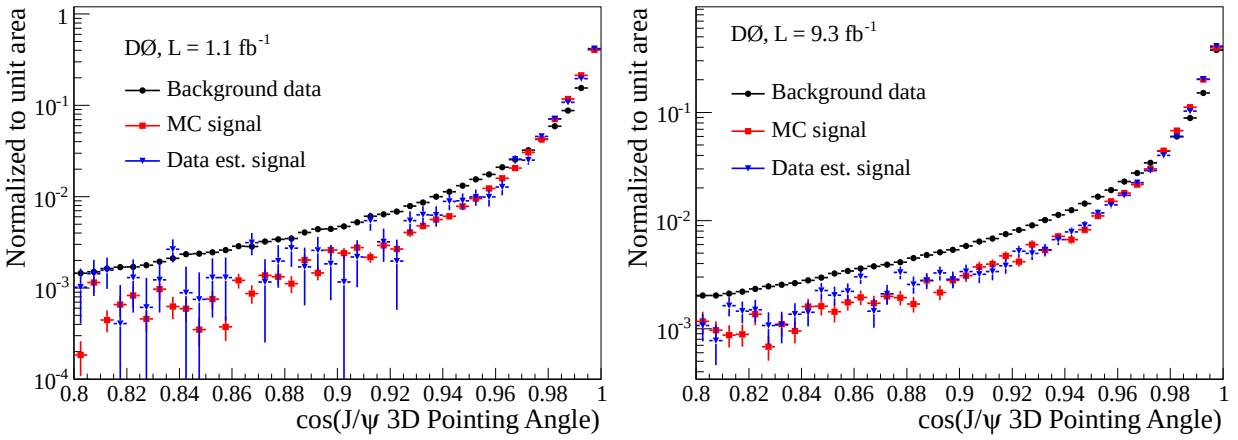

(a) (b)

Figure A.39 : Distributions of cos(J/ψ 3D Pointing Angle) in (a) Run IIa and (b) Run IIb.

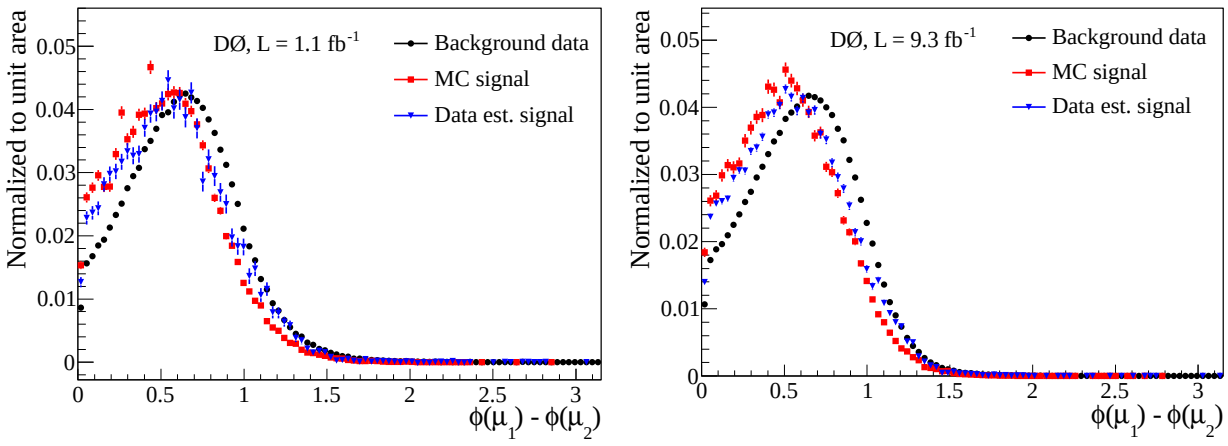

(a) (b)

Figure A.40 : Distributions of $\phi_{\mu_1} - \phi_{\mu_2}$ in (a) Run IIa and (b) Run IIb.